UNIVERSITY OF OKLAHOMA

GRADUATE COLLEGE

DESIGN AND IMPLEMENTATION OF A HIGH POWER, HIGH TEMPERATURE, AND SURFACE MOUNTABLE 2-4 GHZ CIRCULATOR FOR INTEGRATED RF TRANSCEIVERS

A THESIS

SUBMITTED TO THE GRADUATE FACULTY

in partial fulfillment of the requirements for the

Degree of

MASTER OF SCIENCE

By

PAUL HARTLINE

Norman, Oklahoma

2021

DESIGN AND IMPLEMENTATION OF A HIGH POWER, HIGH TEMPERATURE, AND SURFACE MOUNTABLE 2-4 GHZ CIRCULATOR FOR INTEGRATED RF TRANSCEIVERS

A THESIS APPROVED FOR THE

SCHOOL OF ELECTRICAL AND COMPUTER ENGINEERING

BY THE COMMITTEE CONSISTING OF

Dr. Jay McDaniel, Chair

Dr. Hjalti Sigmarsson

Dr. Caleb Fulton

Acknowledgments

A tremendous amount of thanks goes to those who helped me get to where I am today. Above all are my advisors, first Dr. Hjalti Sigmarsson for my senior year of undergrad, and then Dr. Jay McDaniel for my graduate years. They have both entertained my ramblings in topics related and not so related to research and have been an essential source of answers to my questions and excellent sounding boards to my ideas. Dr. Sigmarsson introduced me early in undergrad to the world of radio frequency and microwave engineering, specifically to the world of passive filters. The idea that the change of shape of a copper trace on a board could be utilized to achieve any desired performance captivated me early and is something in which I still find immense beauty. He then introduced me to the world of ferrimagnetic devices, specifically circulators, in which, over time, my primary advisor slowly switched to Dr. McDaniel, who was more familiar with the research area.

Immense thanks go to Dr. Hjalti Sigmarsson, Dr. Shahrokh Saeedi, and fellow student Alex Pham, who taught me everything I know about RF and microwave device fabrication and measurement.

When I was first introduced to ferrimagnetics, most of what I learned was self-taught, as most at the Advanced Radar Research Center (ARRC) were unfamiliar with ferrimagnetic devices at worst and had basic knowledge at best. I would like to thank Douglas Linkhart and Scott Gillette from MetaMagnetics, who taught me early on in my journey the fundamentals and unintuitive intricacies of circulators and other ferrimagnetic devices.

The advantages of working in an open environment such as the ARRC cannot be overstated, as technical and not-so-technical discussions can occur organically at any time, forming a degree of camaraderie between students and trust in the expertise of faculty. In this category, I would like to thank Dr. Caleb Fulton, Dr. Jessica Ruyle, Alex Pham, Alan Murphey, Chris Walker, Russell Kenney, Kurt Konyalioglu, Rachel Jarvis, Grant Karber, Jon Knowles, Marc Thibodeau, and Randall Summers, among many others, for helping me in development of my thesis, and for helping me either professionally or otherwise become the engineer I am today.

In addition to those who provided technical support, I would like to thank those who provided moral support, including my friends and family both inside and outside of Oklahoma. Without their support, I could never have made it as far as I have, and for that, I am genuinely thankful.

Table of Contents

List of Tables

List of Figures

Abstract

With the advent of today's wireless communications systems, the ability for non-local systems to listen to each other is critical. In the case of two monostatic systems communicating with each other, a signal of a given frequency is radiated, and the response listened for. Historically, the given signal had to be given in bursts, with the system set in transmission mode and switched over to a receiving mode in which to listen for a response. This switching mandated that the transmission and receiving modes be not connected, or else the transmitted signal could reach the receiving branch of the system, contaminating data. As the antenna had to switch between these branches, blind spots occurred for distances too close and too far away from the antenna to hear. If one required a maximal listening range in a monostatic system, data pulses had to be short, with a great deal of time in between sending. The solution for the problem turned out to be the circulator, a nonreciprocal device capable of allowing the transmission chain, the antenna, and the receiving chain to simultaneously be connected without signal interference. This nonreciprocity allowed RF power of a given frequency range to only travel in one direction of propagation and was achieved through the use of anisotropic ferrimagnetic materials. The only unfortunate reality of the circulator is the immense difficulty of the design and their unwieldy nature of integration. Compared to other devices operating at similar frequencies, circulators tend to be massive and weighty, with minimal options for integration. In this thesis, a design for a surface mountable octave bandwidth circulator operating at high temperatures and high power levels with a footprint of 1 square inch is presented. Potential fabrication difficulties are simulated and analyzed, with a time domain impedance analysis method used. Simulations and of this circulator display a 20 dB return loss and isolation bandwidth in excess of an octave in the S-band (2-4 GHz). Simulations and measurements show insertion loss is shown to be lower than 0.8 dB in the passband. This circulator demonstrates the feasibility of a high-performance 3D Tetris-like building block method that can be extended to ferrimagnetic circulators of any fractional bandwidth and operating frequency.

Chapter 1

Introduction

1.1 Overview

In any modern wireless communication system, the ability to simultaneously transmit and receive data is critical, even more so if one has a single antenna system. Traditional systems require a physical and/or electrical separation of the transmit and receive ends of the systems, with only one of the two branches connected to the antenna. The usage of nonferrimagnet solutions such as a single pole double throw (SPDT) switch will result in a system incapable of simultaneously transmitting and receiving (STAR) data, as depicted in Figure 1.1. Should the switch be in transmit mode, the receiver will be incapable of picking up incoming signals. Should the switch be in receive mode, the transmitter will be incapable of transmitting. Thus, nonreciprocity is required to achieve STAR. The invention of the ferrimagnetic circulator some decades ago provided the solution to this problem, as they are an RF and microwave device with nonreciprocity, allowing power to propagate in only one direction. Thus, a single antenna system can have the transmit and receive channels simultaneously physically connected to the antenna while they are effectively electrically disconnected from each other.

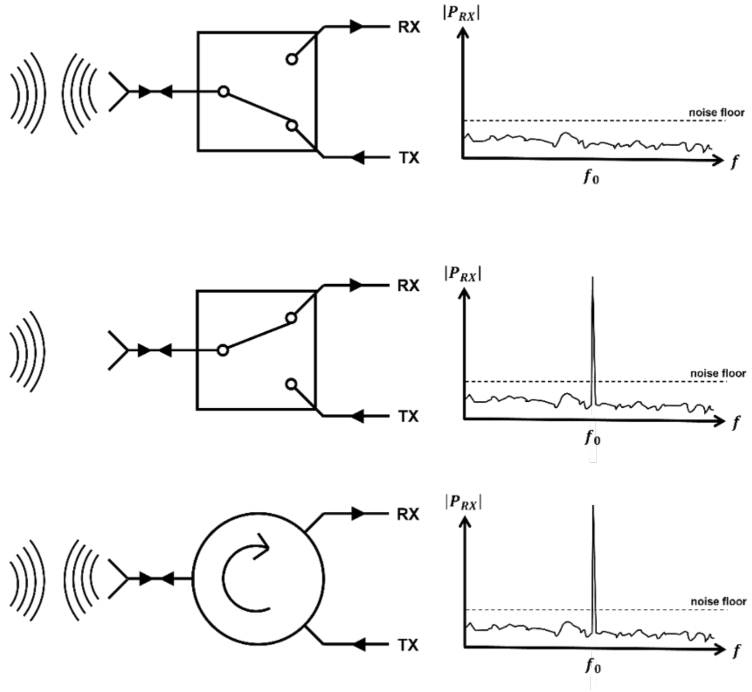

Figure 1.1: Monostatic transceiver architectures, using a SPDT switch in transmit mode (top), receive mode (middle), and using a circulator (bottom).

In a single antenna transceiver, the usage of nonferrimagnet solutions such as a single pole double throw (SPDT) switch will result in a system incapable of simultaneously transmitting and receiving data, as depicted in Figure 1.1. Should the switch be in transmit mode, the receiver will be incapable of picking up incoming signals. Should the switch be in receive mode, the transmitter will be incapable of transmitting. Thus, nonreciprocity is required to

While circulators have proven exceptionally useful, they are typically extremely bulky and heavy devices. The large physical size is largely due to the presence of the ferrite junction, which usually has input resistances far below the standard system impedance of 50Ω. To bring the ferrite junction to the standard system impedance, impedance transformers must be included. These transformers can have varying complexity and electrical size dependent on the desired performance and bandwidth. The high weight is largely owed to the presence of permanent magnets that bias the ferrites. These magnets are in most, but not all [1] ferrimagnetic circulators.

1.2 Ferrimagnetics

Magnetism has been known for thousands of years, ever since the Greeks discovered naturally magnetized minerals called lodestones that were capable of attracting any iron that came too close [2]. However, this was little more than a curiosity until very recently, as its properties remained mysterious and unquantifiable.

Engineering work truly began in ferrimagnetics when Polder [3] described what is now known as the Polder permeability tensor, which described the relationship between magnetic flux density and magnetic field intensity as a function of the DC biasing of the material, the field strength at which the material saturates magnetically, and the frequency of operation of the device. Devices utilizing ferrimagnetic materials started appearing that could boast electrical properties that beforehand were nearly or just outright impossible. Through the use of ferrimagnetics, one can passively introduce nonreciprocity into a circuit, passively force an upper limit on power in a device, and many other remarkable achievements, which are discussed in Chapter 2 of this thesis.

1.3 Device Integration using Surface Mount Technology

Circulators are, in general, extremely bulky devices that are famously difficult to integrate owing to the permanent magnets they house. This limits what commercial off-the-shelf (COTS) circulators can offer, with the vast majority only offering coaxial methods of integration. Drop-in circulators are somewhat common but must be designed in advance with the physical and electrical properties of the integrated printed circuit board (PCB) known, significantly increasing the cost and lead time of the project. This makes the idea of a surface mountable circulator extremely attractive.

The vast majority of circulators utilize stripline transmission lines, as they permit higher bandwidths due to the lack of frequency dispersion in their relative permittivity and their increased power handling in comparison to equivalent microstrip lines, detailed further in Chapter 3. Thus, in a COTS surface mountable circulator, the signal trace must have some level of vertical transition. Previous authors have investigated the performance of wirebond connections between grounded coplanar waveguide transmission lines (GCPW) in non-homogenous substrates of unequal height [4], with the topology as depicted in Figure 1.2.

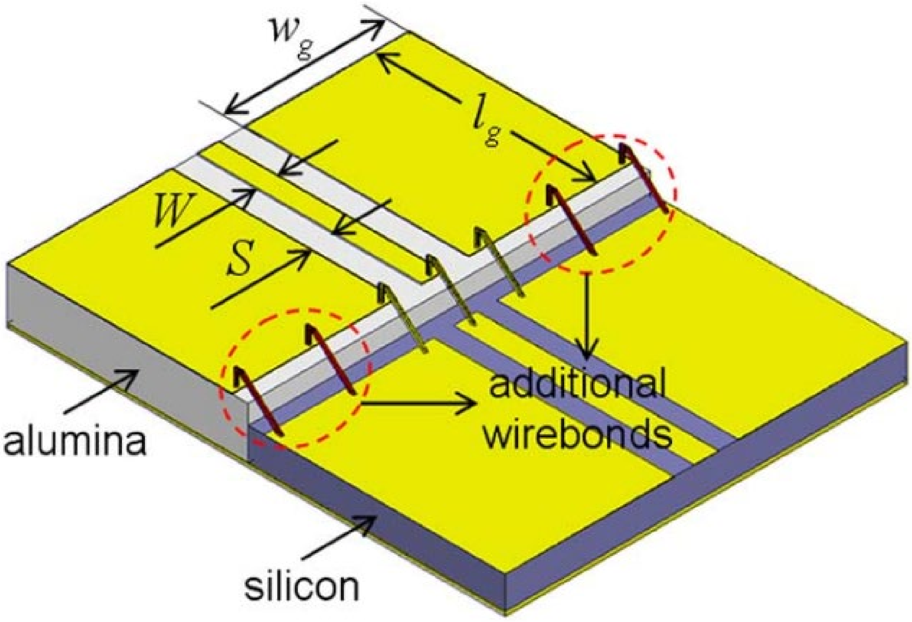

Figure 1.2: Wirebond GCPW to GCPW transition, adapted from [4].

It is often found that using wirebonds to connect GCPW transmission lines on substrates with unequal heights leads to resonances far below what one would expect [5]. These anomalous resonances, of course, lead to an investigation that led to the conclusion that as long as the length of the wirebond is minimal (minimizing wirebond inductance) and the electrical connection between the ground planes is maximized (i.e., maximize the number of wirebonds and minimize their separation), insertion loss is minimal in comparison to the nominal case of a perfect and direct electrical connection between the signal traces and ground planes. As a wirebond can largely be modeled as an inductor, and the increased number of wirebonds are in parallel, the total inductance introduced by the transition is minimized. This decreased inductance serves to push the anomalous resonances up in frequency, as can be seen in Figure 1.3.

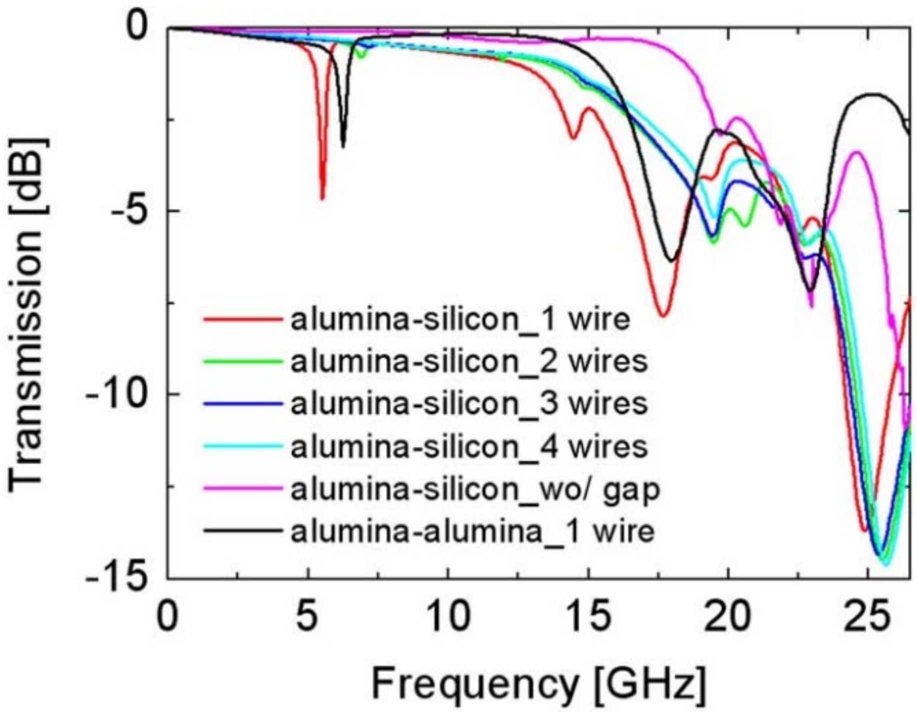

Figure 1.3: Performance of the wirebond GCPW to GCPW transition, adapted from [4]. As the number of wirebonds increase, resonances are moved up in frequency, and insertion loss is reduced.

1.4 Ferrimagnetic Circulators

Ferrimagnetic circulators have seen a long history, and due to their application as high power front-end devices in radar systems, they have seen a large deal of attention in the academic world. Over the years, a variety of methods have been used to induce nonreciprocity using ferrites in order to create a circulator, but to the best of this author's knowledge, the theory behind ferrimagnetic circulators was first characterized and defined by Hogan in 1952 [6]. Hogan created a waveguide implemented isolator that utilized Faraday rotation in which to provide a nonreciprocal response, generating a scattering matrix S such as:

$$S = \begin{bmatrix} 0 & 0 \\ 1 & 0 \end{bmatrix} \tag{1.1}$$

Hogan's prototype, through biasing and rotation of the output port, was capable of isolating a wide range of frequencies. This successful isolator proved the viability of nonreciprocal power transfer through the use of ferrimagnetic materials.

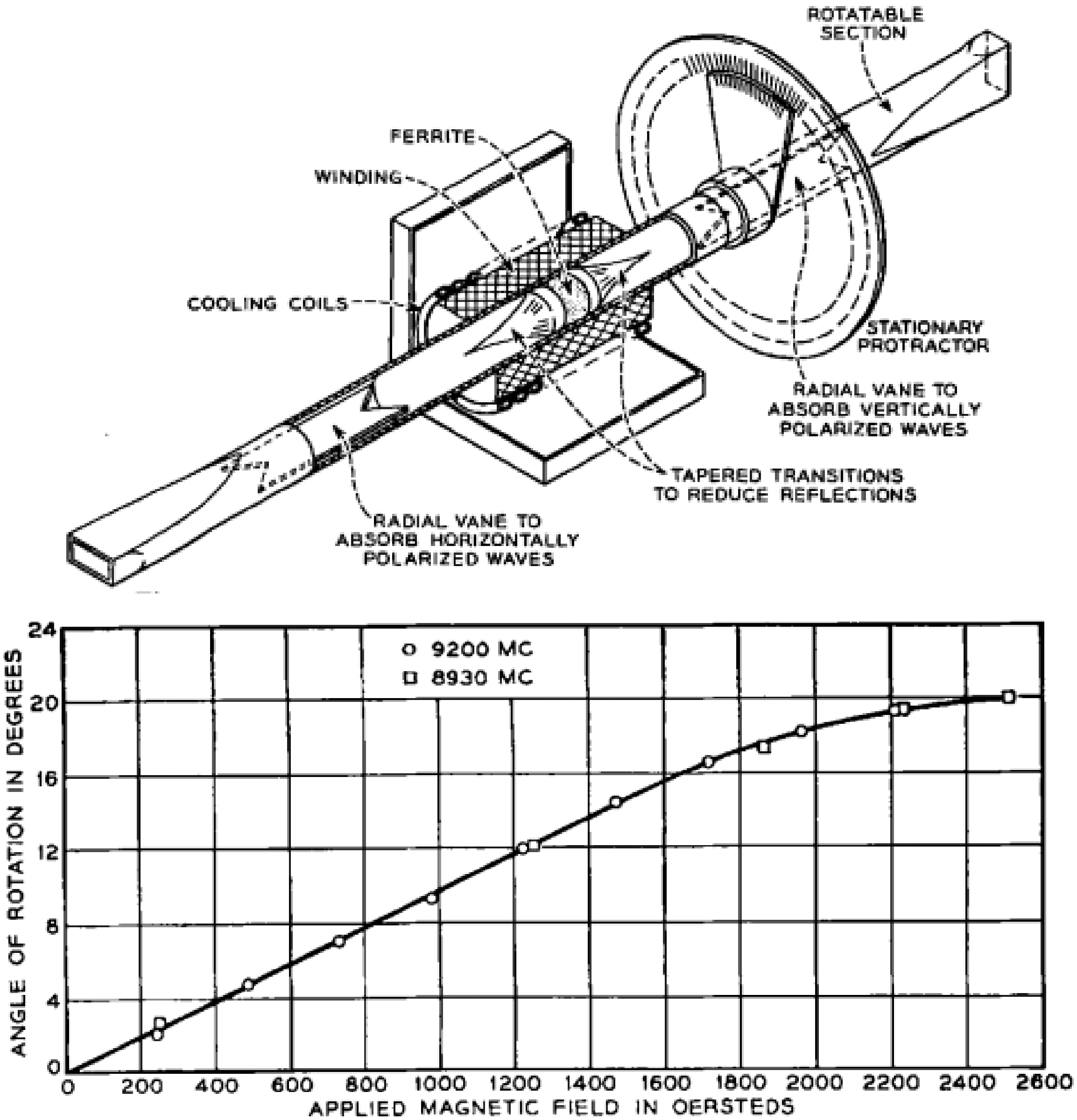

Figure 1.4: Faraday rotation-based circulator as described by [6] (top) and the degree of rotation versus biasing level for two frequencies (bottom).

To this author's knowledge, the first to accurately model and describe and validate the theory behind junction circulators is Bosma [7], based on the work of previous authors

[8]-[10]. From first principles, Bosma described the relationship between the electromagnetic properties of the ferrite resonator and the stripline junction and structure using Green's Function and demonstrated the dependence of the frequency of junction resonance on magnetic saturation, magnetic biasing, and coupling angle.

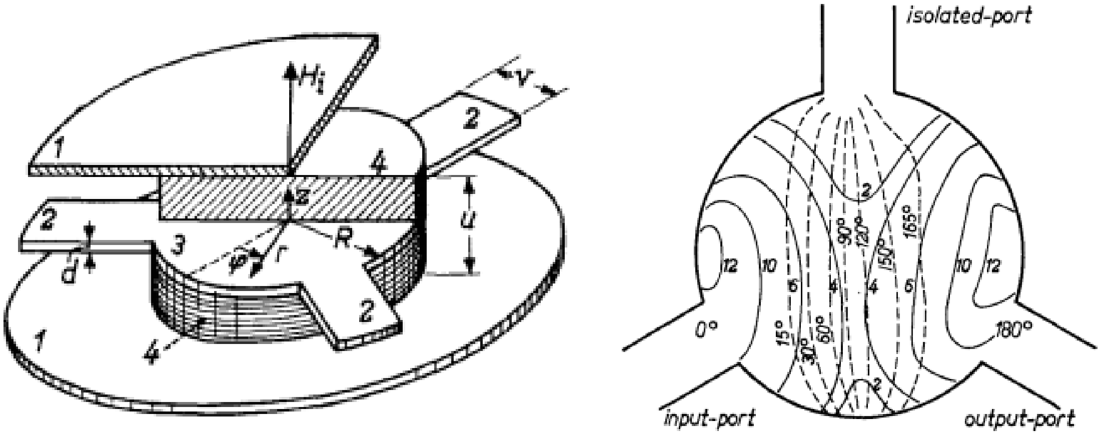

Figure 1.5: Basic circulator structure as adapted from [7] (left), with the measured electric field amplitude in arbitrary units additionally shown (right). Dashed lines are to show areas of equal phase.

The basic theory of stripline-based broadband ferrimagnetic junction circulators was perfected by Helszajn [11]. Through the use of quarter-wave transformers, one can achieve octave bandwidth performance. Additionally, he extracted the relationship between the loaded quality factor of a ferrite junction with all relevant variables in the junction, most notably the ferrite biasing and magnet saturation, the radius of the ferrite, and the feedline coupling angle.

For ferrimagnetic junction circulators, the complexity of design presents a significant obstacle in direct integration. As such, many opt for a commercial off-the-shelf (COTS) solution. Among the most common implementation methods seen in these devices are coaxial connections, drop-in connections, and surface mount connections. A coaxial connection presents a quick and easy solution in circuit integration at the cost of circuit size and structure. Drop-in circulators are the second most common, which involve removing substrate from a circuit board until the circulator device can be inserted, such that the protruding traces in the structure can meet the existing PCB traces [12]. This method is extremely rare in COTS devices, and the exact circulator shape and size are highly dependent on the existing circuit. As such, the circulator engineer will often work with the PCB engineers on the specifications and limitations on device size. Meanwhile, surface mount connections are rare but not nonexistent. Depending on the design direction, these circulators can involve as little alteration to an existing circuit board as the signal traces connecting the circulator to the circulator and the needed ground plane continuity, much the same as any other microstrip or stripline surface mountable device [13].

1.5 Outline

This thesis aims to demonstrate the theory, design, implementation, fabrication, and refinement of a broadband high power, high temperature below resonance ferrimagnetic junction circulator. As such, a section of this thesis will be devoted to each aspect in turn for the circulator.

Chapter 2 covers the basic theory of ferrimagnetic circulators and their modes of operation, along with design considerations ferrimagnetic materials bring to high power and high temperature conditions. As the circulator discussed in this thesis is a below resonance circulator, the closed-form modeling of circulators will be focused on the below resonance mode of operation.

Chapter 3 details the design of the electrical circuit and magnetic biasing circuit of the circulator designed for this thesis. The closed-form solutions will be discussed, along with the simulation and refinement of the circulator. Due to the complexity in simulating a ferrimagnetic circulator in finite element method electromagnetic solvers such as Ansys HFSS, the simulation of the circulator is broken down into several smaller designs that are coalesced and simulated once each section has been tuned. Results will be shown and discussed, with performance changes as a function of several variables, as a way to more intuitively inform the reader of the considerations in the below resonance circulator design.

Chapter 4 discusses the fabrication and testing of the octave bandwidth circulator, along with the testing board designed to test the surface mount integration. The general testing circuit will be analyzed, shown, and discussed, along with the high power and high temperature measurement systems. Input impedance and group delay extraction from measured scattering parameters is additionally discussed.

Chapter 5 goes into detail upon the time domain impedance analysis method that is often used in filter tuning. While most useful for high order filters, this analysis method is of particular interest in circulators due to requiring access to a single port. While all ports of a circulator are accessible at all times, the nonreciprocal nature of the circulator provides a degree of complexity in measurement and analysis that is assuaged by this method that is capable of showing the exact location of an impedance mismatch in a circuit from return loss alone.

Chapter 6 summarizes the work in this thesis and details the conclusions that can be drawn from it and used by future ferrimagnetic engineers. The scientific contribution of this thesis is also discussed at length, along with possible future work and methods of improvement for the work in this thesis.

Chapter 2

Ferrimagnetic Circulator Theory

In the RF and microwave world, the design and construction of circulators and ferrimagnetic devices, in general, are an oft-ignored subject. As such, the basics necessary to understand the content of this thesis will be covered before the design, fabrication, and testing of the circulator in this thesis will be discussed. The non-linear and non-reciprocal effects that can be introduced by utilizing ferromagnetic and biased ferrimagnetic materials are of profound interest in a variety of applications. As always in engineering, there is a trade-off space when ferrimagnetic materials become involved, the two most significant being between bandwidth and power handling nearly regardless of what ferrimagnetic device is being created. The trade-off space will be discussed in detail in this section.

2.1 Introduction to Ferrimagnetics

Ferrimagnetics is an area only rarely studied in the RF and microwave field, and as such, finding a decent introduction to the topic is arduous at best. Many papers and texts often assume that the reader has an understanding already or focus on minor details and skim over much more relevant and impactful details. As such, this thesis will attempt an overview of ferrimagnetics from first principles in order to allow RF and microwave engineers who have no ferrimagnetics experience to understand and implement.

Before any concepts, principles, properties, or definitions are discussed, a few notes need to be made with regards to units and a common notation in ferrimagnetics. For magnetic flux density (B) and magnetic field intensity (H), the traditional SI units (Tesla and Ampere per Meter, respectively) are not used. Instead, ferrimagnetic specialists almost exclusively use their centimeter-gram-second (CGS) unit equivalents, Gauss $(1\,G = 10^{-4}\,T)$ and Oersted $\left(1\,Oe = \frac{1000}{4\pi}\,A/m\right)$, respectively. Initially, this choice seems arbitrary and unnecessary until one remembers that the permeability of free space μ_0 is equal to

$4\pi \cdot 10^{-7}\ H/m$, resulting in a very simple non-magnetic medium permeability of $\mu = 1\ G/Oe$. Thus, in any non-magnetic medium, magnetic flux density and magnetic field intensity can be considered equivalent, dramatically simplifying the mathematics of ferrimagnetic devices.

In addition to units, one should be made aware of a common notation that differs significantly from the rest of the RF and microwave field, in that the symbol for frequency will be either f or ω, depending on the author. Whichever the author uses, it will refer to either ordinary frequency (Hz) or radian frequency (rad/s), almost interchangeably. Initially, this defies all logic and seems prone to copious errors, but is remedied somewhat by the fact that in the vast majority of ferrimagnetic specific equations, frequency is divided by the gyromagnetic ratio γ, which has either the units of $Hz/Oe\ or\ 2\pi \cdot Hz/Oe$ dependent entirely on if ordinary or radian frequency is used, respectively. For the sake of simplicity and to help bridge the gap for those who do not have experience in ferrimagnetics, this thesis will use f for ordinary frequency and ω for radian frequency. In equations that include the gyromagnetic ratio γ, f will be used to align with common ferrimagnetic notation, but the reader should note which frequency used does not matter in such cases.

An additional source of confusion for newcomers to ferrimagnetics is the unit for the magnetic saturation of a material, expressed as either M_S or $4\pi M_S$, usually expressed in Gauss (G). While confusing, these two units are interchangeable, and the additional 4π is not an additional scalar multiplier. The historical reason for this confusing notation lies in the ferrite demagnetization factors N_x, N_y, and N_z, which relate the magnetic field intensity inside the ferrite to that outside in each axis. The sum of the demagnetization factors are normalized to be equal to either 1 or 4π, with magnetic saturation being equal to $4\pi M_S$ or M_S, respectively. The normalization of demagnetization factors to 4π has largely fallen out of favor, with most academic papers assuming a normalization of 1. Demagnetization factors are discussed in further depth later in this section. To keep with the traditional notation, but to help prevent confusion, all instances of magnetic saturation in discussions and equations in this thesis with use $(4\pi M_S)$, separated from the rest of the equation by brackets.

A quick note should be made about “ferromagnetic” vs. “ferrimagnetic, which are sometimes confused for each other. While both classes of material are very similar, the primary difference lies in the strength of their quantum and magnetic effects. When ferromagnetic materials are biased, the structure of the magnetic dipole moments of the material grains, also called domains, are entirely aligned, producing a very powerful magnetic flux density inside the material [14]. As such, permanent magnets are usually created using "hard" ferromagnetic materials, whose coercive field H_C, is very large, making demagnetization immensely difficult. Ferrimagnetic materials, on the other hand, do not produce a uniformly oriented magnetic dipole moment in each domain, providing a degree of cancellation between electrons in the strength of the magnetic flux density. Thanks to this phenomenon, ferrimagnetic materials, also known as "soft" magnetic materials, have a magnetic flux density strength on the order of one-tenth that of comparable ferromagnetic materials. For this thesis, unless otherwise stated, all ferrites mentioned are composed of a "soft" ferrimagnetic material, and all permanent magnets are composed of a "hard" ferromagnetic material.

While the magnetic flux density and magnetic field intensity can be considered equivalent with equal strength and direction in non-magnetic mediums using our new units, calculations become significantly more complex inside a ferrimagnetic medium due to the introduction of magnetization and a magnetic moment due to the externally applied field. B and H are now related by:

$$\bar{B} = \mu_0(\bar{M} + \bar{H}) = [\mu]\bar{H} \tag{2.1}$$

where, μ_0 is the permeability of free space, $\bar{B}$ and $\bar{H}$ are the magnetic flux density and magnetic field intensity, respectively, $\bar{M}$ is the magnetization, and $[\mu]$ is the general permeability tensor. For externally biased ferrimagnetic and ferromagnetic materials, Polder [3] has specific solutions for the tensor, now referred to as the Polder permeability tensor, dependent on the axis of magnetic biasing:

$$[\mu] = \mu_0\left(\left[\overline{U} + [\overline{\chi}]\right]\right) = \begin{bmatrix} \mu & j\kappa & 0 \\ -j\kappa & \mu & 0 \\ 0 & 0 & \mu_0 \end{bmatrix} (\hat{z}\ bias)$$

$$[\mu] = \begin{bmatrix} \mu_0 & 0 & 0 \\ 0 & \mu & j\kappa \\ 0 & -j\kappa & \mu \end{bmatrix} (\hat{x}\ bias) \qquad (2.2)$$

$$[\mu] = \begin{bmatrix} \mu & 0 & -j\kappa \\ 0 & \mu_0 & 0 \\ j\kappa & 0 & \mu \end{bmatrix} (\hat{y}\ bias)$$

where μ_0 is the permeability of free space, $\overline{U}$ is the unitary or identity matrix, and $[\overline{\chi}]$ is the susceptibility tensor, μ is the real part of the permeability tensor, and κ is the imaginary part of the permeability tensor. The elements of the permeability tensor can be calculated directly from the circuit RF frequency, material magnetic saturation, and applied magnetic bias using:

$$\mu = \mu_0\left(1 + \frac{f_0 f_m}{f_0^2 - f^2}\right) \qquad \kappa = \mu_0\left(\frac{f\, f_m}{f_0^2 - f^2}\right) \qquad (2.2)$$

where f is the frequency of operation, f_0 is the ferrimagnetic resonance (FMR) frequency of the material under bias, and f_m is the FMR frequency's magnetic saturation equivalent, which has no physical interpretation. While these frequencies are discussed in greater detail in this thesis in Section 2.2, for the purposes of this explanation, they are defined as:

$$f_0 = \mu_0 \gamma H_0 \quad Hz \qquad f_m = \mu_0 \gamma (4\pi M_S) \quad Hz \qquad (2.3)$$

where γ is the gyromagnetic ratio that will be defined later in this section, H_0 is the magnetic field intensity internal to the ferrite, and $4\pi M_S$ is the magnetic saturation value of the ferrite material. An example of the Polder permeability tensor values versus frequency can be seen in Figure 2.1, which was generated using $f_0 = 1\ GHz$, $f_m = 1\ GHz$, and a ferrite linewidth $\Delta H = 25\ Oe$. The ferrite linewidth is a value defined later in this section of this thesis, but for the moment, it can be simply interpreted as a measure of the magnetic losses of the ferrite, analogous to a dielectric's loss tangent.

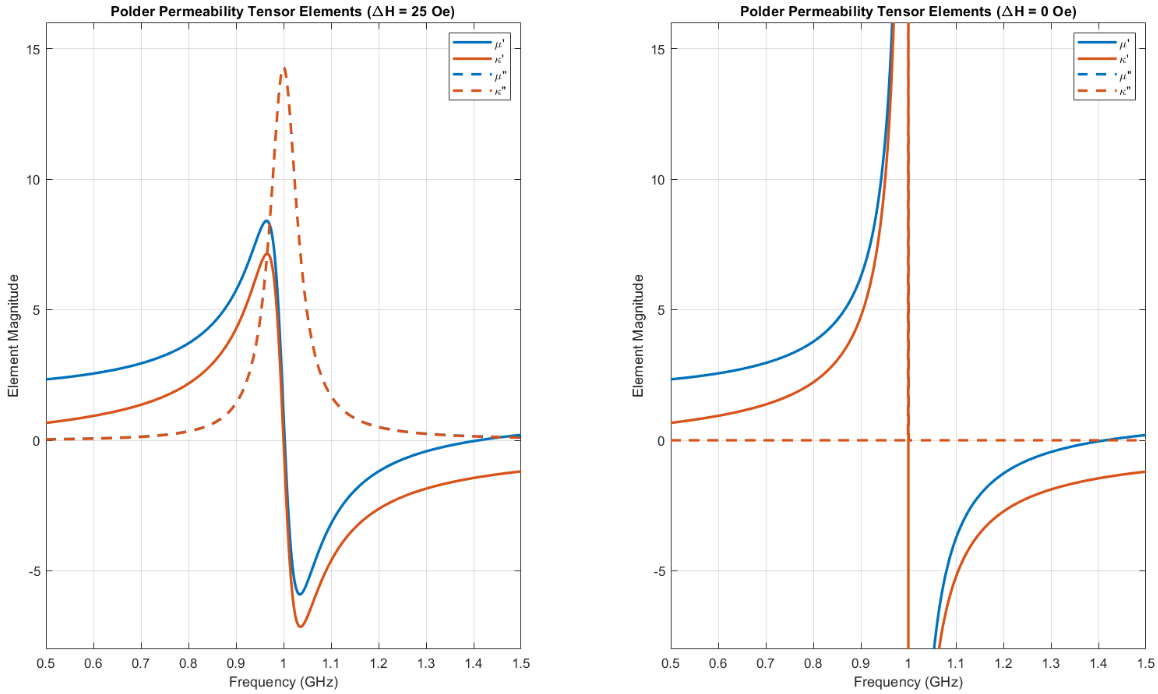

Figure 2.1: Polder permeability tensor elements versus frequency, normalized to the ferrimagnetic resonance frequency. Depicted are identical cases with an arbitrary level of magnetic loss (left), and no magnetic loss (right).

This is, unfortunately, another case in which common ferrimagnetic notation is unintentionally confusing to the newcomer. In (2.2), μ represents the real part of the Polder permeability tensor, while κ represents the imaginary part. There are many cases in ferrimagnetics where a scalar value for permeability can be desirable, such as in calculating the radius for a ferrite disk in a circulator. For such situations, an effective relative permeability is used that is defined as:

$$\mu_{eff} = \frac{\mu^2 - \kappa^2}{\mu} \tag{2.4}$$

Up to this point, the lossless case has been assumed. Of course, this is not the reality. In a practical resonator, there is always some degree of loss, forcing an upper limit on the potential performance of the resonator and a lower limit on the loss. This loss is represented for such cases by including a resistive element to the LC network, creating an RLC circuit. This, of course, makes the resonant frequency complex [15]. For a ferrimagnetic material, the relevant, resonant frequency is the FMR frequency, which is discussed further later in Section 2.2. For the moment, the FMR frequency is the magnetic biasing level dependent resonant frequency at which the imaginary parts of the Polder permeability tensor elements μ and κ become maximized, and the real part of the Polder permeability tensor elements crosse from positive infinity to negative infinity, as in Figure 2.1. When magnetic losses are introduced, this effect is diminished, as will be discussed momentarily. The exact frequency of FMR that is achieved is a simple relation, based only on the DC magnetic field intensity strength inside the ferrite H_0, and the effective Lande g factor of the ferrite material g_{eff}. The Lande g factor is simply a relation of the contributing factors to the total magnetic moment of the electrons in the ferrite material. When the only contribution is spin moments, the Lande g factor is equal to 1, and when the only contribution is orbital motion, the Lande g factor is equal to 2. If both elements are present, this value can increase. For the vast majority of ferrite materials, this value is very close to 2. The Lande g factor is a parameter that is largely independent of magnetic biasing but has experimentally been found to vary when under very high levels of bias [16]. This experimentally found value is called the effective Lande g factor and is usually close enough to the true Lande g factor that it can be safely ignored for design specifications that are not extremely demanding.

The deviation of the complex resonant frequency from the purely real resonant frequency results in the damping factor α:

$$\omega_0 = 2\pi f_0 \quad \rightarrow \quad \omega_0 + j\alpha\omega \tag{2.5}$$

The inclusion of this damping factor makes the values of the ferrite permeability tensor complex, resulting in the much more computationally convoluted form of the tensor elements seen in [15]. It is readily seen from these elements that at the resonance frequency, the imaginary part of the tensor element μ will be maximized. As the damping factor increases, the magnitude of this loss reduces, with the relative width increasing. When looking at datasheets of ferrimagnetic materials, one will see the parameter ΔH, the linewidth of the ferrite. This value is defined as the width of the loss at resonance, at a magnitude half that of maximum. Handily, the damping factor is related to this linewidth by a simple equation:

$$\Delta H = \frac{2\alpha f_0}{\gamma} \quad Oe \tag{2.6}$$

where all the variables are as they have been defined in this section of this thesis. An example of the definition of the ferrite linewidth can be seen in Figure 2.2, where a ferrite linewidth of 100 Oe has been introduced, with a magnetic field intensity inside the material corresponding to 1 GHz. For either frequency at 3 dB down from the maximum value of the magnetic susceptibility.

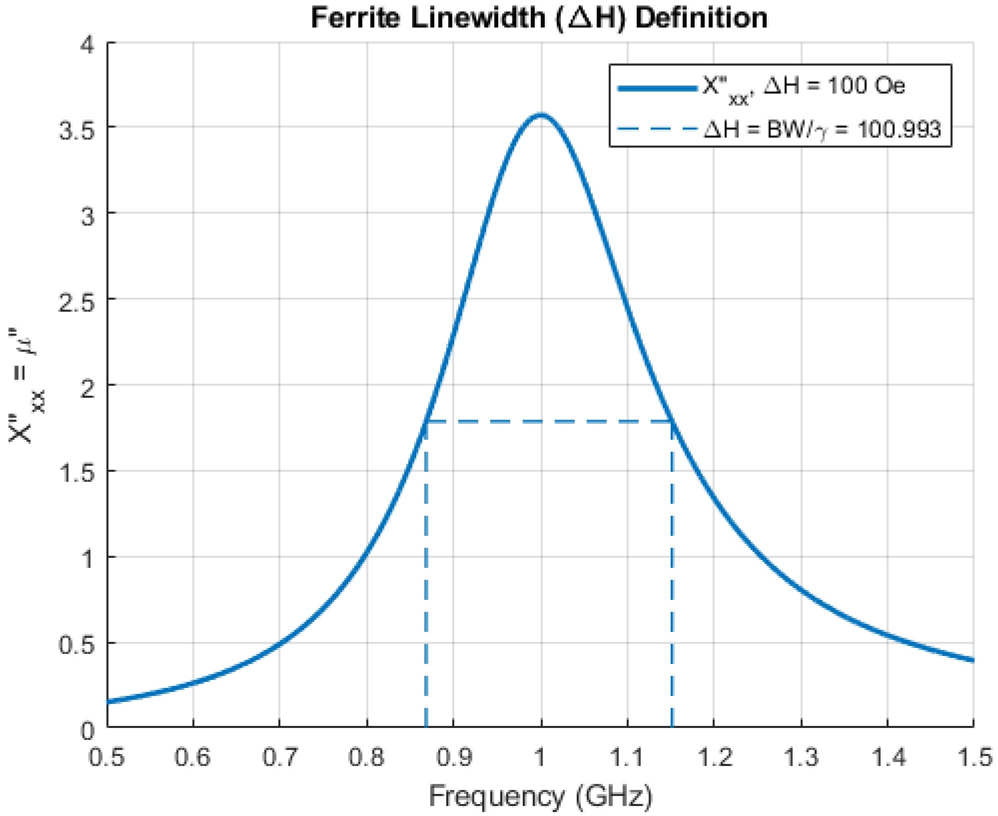

Figure 2.2: Definition of ferrite line width. The bandwidth of the imaginary part of the Polder permeability tensor element μ (marked with dashes) where the magnitude is greater than half the maximum is divided by the FMR frequency, discussed in Section 2.2.

Experiments [17] have shown that the linewidth ΔH does not show the full picture, with the imaginary part of the Polder permeability tensor μ being much higher than expected at the FMR frequency and much lower than expected far away. The effective line width

ΔH_{eff} is typically smaller than ΔH (often a factor of 4 to 10), as the magnetic losses are concentrated at the precession frequency, as in Figure 2.3.

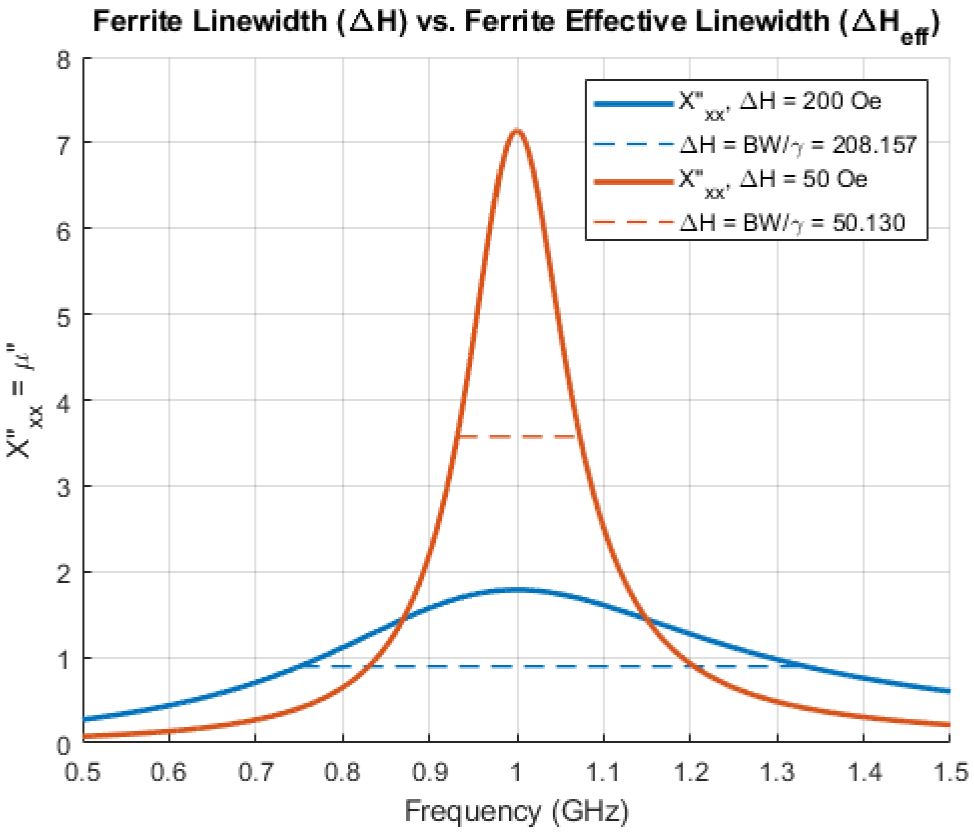

Figure 2.3: Comparison of line width and effective line width. True line width (blue) is applicable when near ferrimagnet resonance, and effective line width (orange) is applicable when far away in frequency.

When unbiased, there is little difference between a ferrite resonator and a dielectric resonator, and the ferrite can be said to have a single resonant mode at its lowest resonant frequency. When biased, this mode splits into two circularly or elliptically polarized modes, rotating in opposite directions, at different frequencies with one slightly above the original frequency and one below. The superposition of these two modes results in what is effectively a single resonant mode that has been rotated around the biasing axis. The amount of splitting is measured by the ratio of the ferrite permeability tensor elements, κ/μ. In three-port junction circulators, the resonator design goal is choosing material and biased such that the fields are canceled at the isolated port and equal between the incident and output ports. The counter-rotating modes have differing permeabilities in addition to the resonant frequency, given by:

$$\begin{aligned} \mu^{+} &= \mu + \kappa = \mu_0\left(1 + \frac{f_m}{f_0 - f}\right) \\ \mu^{-} &= \mu - \kappa = \mu_0\left(1 + \frac{f_m}{f_0 + f}\right) \end{aligned} \tag{2.7}$$

It can be seen from magnetic boundary conditions that when biasing a ferrite with an externally applied DC magnetic field, that the field internal to the ferrite medium will typically be different than the field in free space, while the magnetic flux density will typically be the same in both media thanks to the ferrite having a permeability that is not equal to free space. What is less clear at first glance is the relationship between the internal and external fields versus ferrite shape and orientation relative to the biasing field, which can differ greatly based on application. Thankfully, there is a simple way to relate the magnetic field intensity in differing media through the use of demagnetization factors and Kittel's equation [18]:

$$H_{int} = \sqrt{\{H_{ext} + (N_x - N_z)(4\pi M_S)\}\{H_{ext} + (N_y - N_z)(4\pi M_S)\}} \quad Oe \;\; (\hat{z}\; bias) \tag{2.8}$$

Demagnetization values for various shapes are readily found in the literature [19] - [21]. Of note is the demagnetization factors for a small ferrite sphere $\left(N_x = N_y = N_z = 1/3\right)$, which results in an internal magnetic field intensity equal to that outside the sphere. This relationship is exploited in ferrite material tests in order to measure the magnetic saturation of the material in question [22]. While a spherical ferrite is mathematically interesting and used as a reference for material tests, it has extremely limited applications. The most common ferrite shapes are electrically thin plates $\left(N_x = N_y = 0,\; N_z = 1\right)$ used in junction circulators, and axially thin rods $\left(N_x = N_y = 1/2\,,\; N_z = 0\right)$ used in resonance isolators, phase shifter, and switches [15].

It is at this point the demagnetization curve of magnetic materials, also known as the hysteresis curve, must be discussed. Demagnetization factors and Kittel's equation assume the ferrimagnetic material is saturated, such that all the individual magnetic dipole moments in the ferrite's domains have become aligned. This alignment causes the magnetization of the material to remain approximately constant, regardless of any additional magnetic biasing applied. The relationship between magnetic flux density and magnetic field intensity for biasing levels lower than saturation is far more complicated, as can be inferred from Figure 2.4.

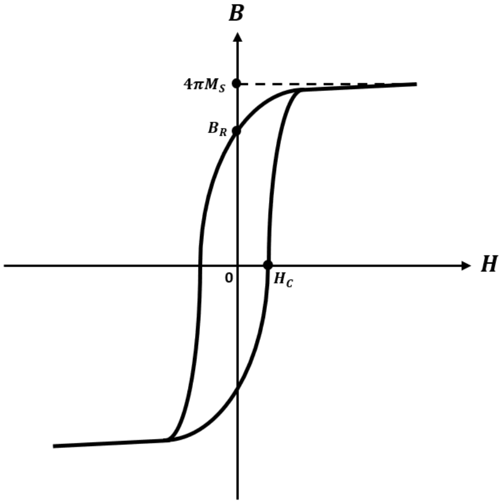

Figure 2.4: Typical demagnetization curve, also known as a hysteresis curve, for a ferrimagnetic material. The points at which several important variables are defined are marked.

As the external biasing increases, the magnetic flux density in the ferrite follows a non-linear curve until it begins to saturate near the value referred to as the magnetic saturation, naturally. Once saturated, decreasing the magnetic biasing to zero does not leave the material demagnetized but rather leaves the material with a magnetization at B_R, the retentivity, also known as the residual flux density [14]. Applying an external bias with the opposite polarity as originally applied to $|H_C|$, the coercive field, will result in a completely demagnetized ferrite material.

A large variety of chemical compositions for ferrimagnetic materials exist, each with its own tradeoffs with its magnetic properties. In general, these chemical variations can be classed in one of three major categories: spinels, garnets, and hexaferrites [23]. Spinels and garnets are composed of crystal structures in which a large number of iron ions exist, sufficient in quantity to make the material ferrimagnetic but not ferromagnetic. Replacing the existing iron ions in the crystal structure with aluminum, cobalt, lithium, yttrium, or any number of similar elements can reduce the magnetic saturation the material is capable of, as well as allowing a degree of control over the magnetic line width. This doping is used to create ferrite materials of almost any combination of magnetic properties. Some of the most commonly used garnet-type ferrites are yttrium iron garnet (YIG) and calcium vanadium garnet (CVG). Some of the most commonly used spinel-type ferrites are lithium and magnesium manganese-based. The primary difference between garnets and spinels that a ferrimagnetics engineer would be interested in is the level of magnetic saturation that can be achieved. Spinels are capable of attaining magnetic saturation values in excess of 3.5 kG at room temperature, whereas an undoped YIG material has a saturation of only 1.8 kG [24]. The final class of ferrite is hexaferrites, which owe their name to their hexagonal crystal structure. Typically, hexaferrites are used for permanent magnets and for high frequency (above Ku band) RF and microwave devices due to the typically very small grain size, which assists performance, as is further described in Section 2.4.

It was made apparent to the author that a broad introduction to magnetic modeling and simulation would be of assistance to readers. While direct mathematical modeling using the equations in this paper was done using MathWorks' MATLAB and circuit design using Keysight's Advanced Design System 2017 (ADS), electromagnetic modeling of ferrimagnetic components was done using the finite element method electromagnet solvers Ansys HFSS and Maxwell. In general, Ansys HFSS was used for the S-band (2 – 4 GHz) electrical circuit, and Ansys Maxwell was used for the DC magnetic biasing circuit. It will be assumed that the reader already has some familiarity with Ansys HFSS, so only the ferrimagnetic details will be discussed. Usage of Ansys Maxwell will be discussed in full.

The implementation of ferrimagnetic materials in Ansys HFSS is simple if one is already familiar with the other aspects of Ansys HFSS. Materials can be defined as normal in virtually all regards, with the single exception of relative permeability. Here, the material must be defined as having a tensor type permeability with each element equal to the corresponding Polder permeability tensor value relative to the permeability of free space. If one is designing a ferrimagnetic device with a passband that is near the FMR frequency, one needs to set a frequency dependency on the permeability tensor. Alternatively, one can leave the permeability tensor as predefined (simple type, equal to 1) and assign a magnetic bias value as an excitation, equal to the internal field magnitude. The direction of bias can be easily varied from there.

Regardless of the method of applying a magnetic bias, the magnetic saturation level must be specified, assuming one is designing a ferrimagnetic device operating at saturation. The ferrite linewidth and the Lande g factor are entered as normal, and they each refer to the effective value rather than the true value.

If one is familiar with Ansys HFSS, then the usage of Ansys Maxwell will be largely familiar, differing largely in defining material properties and in defining excitations. For ferrimagnetic purposes such as those used in this thesis, magnetic excitations are defined solely via material definition, creating little difference between the two. For magnetic materials, one defines the permeability, in this case, a BH curve, as either normal or intrinsic. Additionally, one must define a coercive force and a direction. To create a permanent magnet and thus an excitation, one must use the normal demagnetization curve associated with the material, often found on its datasheet. Ansys Maxwell then automatically defines the coercive point as the demagnetization curve's intercept with the H axis. One then defines the direction of magnitude as the direction of magnetization. As all of the disk magnets discussed in this thesis are normal to the circuit, they are all polarized in $\hat{z}$. To define a non-magnetized magnetic material such as the ferrites and the MuMetal clamp discussed in Chapter 3, one defines the materials as having an intrinsic curve with a coercive force of 0. The final note is the definition of the air box. Similar to antennas in Ansys HFSS, one should define the airbox as being much larger than the circuit in question. As Ansys Maxwell is magnetostatic by definition, there is no rule of thumb for electrical distance, but rather based solely on the largest dimension involved, where the airbox should be at least three times larger in each axis as the circuit. Beyond the unorthodox definition of excitations, the differences between Ansys HFSS and Ansys Maxwell are minimal.

Figure 2.5: Side view of a Maxwell model, depicting ferrites being biased via permanent magnets.

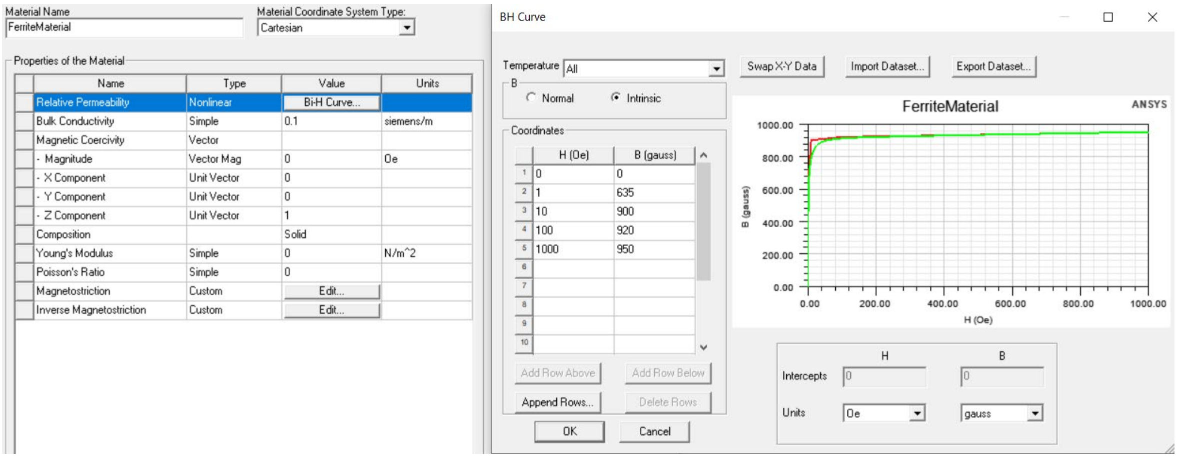

Material Name: FerriteMaterial

Material Coordinate System Type: Cartesian

Properties of the Material

Name	Type	Value	Units
Relative Permeability	Nonlinear	Bi-H Curve...	
Bulk Conductivity	Simple	0.1	siemens/m
Magnetic Coercivity	Vector		
- Magnitude	Vector Mag	0	Oe
- X Component	Unit Vector	0	
- Y Component	Unit Vector	0	
- Z Component	Unit Vector	1	
Composition		Solid	
Young's Modulus	Simple	0	N/m^2
Poisson's Ratio	Simple	0	
Magnetostriction	Custom	Edit...	
Inverse Magnetostriction	Custom	Edit...	

Temperature: All

B: ○ Normal ● Intrinsic

Coordinates

	H (Oe)	B (gauss)
1	0	0
2	1	635
3	10	900
4	100	920
5	1000	950
6		
7		
8		
9		
10		

	H	B
Intercepts	0	0
Units	Oe	gauss

Figure 2.6: Material definition of the initially unmagnetized (non-excitation) ferrimagnetic material. As the material is initially unmagnetized, the material has an intrinsic demagnetization curve.

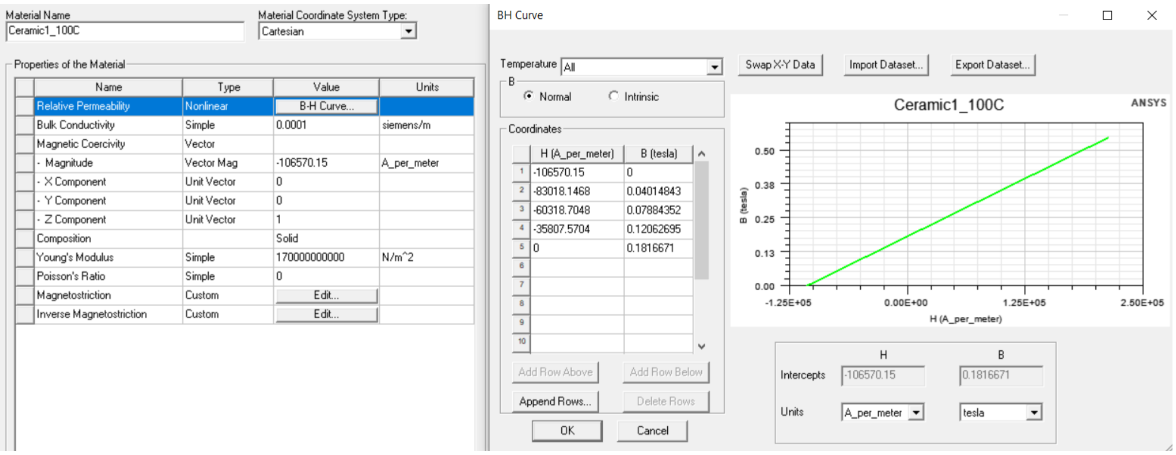

Material Name: Ceramic1_100C

Material Coordinate System Type: Cartesian

Properties of the Material

Name	Type	Value	Units
Relative Permeability	Nonlinear	B-H Curve...	
Bulk Conductivity	Simple	0.0001	siemens/m
Magnetic Coercivity	Vector		
- Magnitude	Vector Mag	-106570.15	A_per_meter
- X Component	Unit Vector	0	
- Y Component	Unit Vector	0	
- Z Component	Unit Vector	1	
Composition		Solid	
Young's Modulus	Simple	170000000000	N/m^2
Poisson's Ratio	Simple	0	
Magnetostriction	Custom	Edit...	
Inverse Magnetostriction	Custom	Edit...	

Temperature: All

B: ● Normal ○ Intrinsic

Coordinates

	H (A_per_meter)	B (tesla)
1	-106570.15	0
2	-83018.1468	0.04014843
3	-60318.7048	0.07884352
4	-35807.5704	0.12062695
5	0	0.1816671
6		
7		
8		
9		
10		

	H	B
Intercepts	-106570.15	0.1816671
Units	A_per_meter	tesla

Figure 2.7: Material definition of the initially magnetized (excitation) permanent magnets. As the material is initially magnetized, the material has a normal demagnetization curve.

2.2 Circulator Modes of Operation

Any given ferrimagnetic circulator can be classed in one of three categories, based on their mode of operation governed largely by the strength of the ferrite's biasing field: Below resonance, resonance, and above resonance. The titular resonance refers to where the gyromagnetic resonance f_0 is located in relation to the passband of the circulator. A standard circulator with non-stringent specifications can be any mode of operation, but all have inherent trade-offs that must be considered if specifications become demanding. The FMR frequency has gone by many names over the years depending on the author and time, and includes such names as gyromagnetic resonance frequency, precession frequency, and the Larmor frequency [18]. For the sake of simplicity, this thesis will use the descriptive, simple, and modern name of FMR frequency. In addition, there is occasionally a frequency denoted as either ω_m or f_m. This frequency has no name as far as this author is aware, as it has no physical meaning and is simply a means of simplification and symmetry with f_0 in ferrimagnetic equations, as the terms in its definition are very commonly together. The FMR frequency f_0 is simply calculated using:

$$f_0 = \mu_0 \gamma H_0 \quad Hz$$
$$f_m = \mu_0 \gamma (4\pi M) \quad Hz \tag{2.9}$$
$$\gamma = \left({}^{g_{eff}}\!/_{2} \right) \cdot 2.8 \ {}^{MHz}\!/_{Oe}$$

where the terms are as defined and described in Section 2.1. $4\pi M$ is used in lieu of $4\pi M_S$ for the magnetic moment to be more general as not all ferrimagnetic devices and applications utilize saturated ferrite materials, and the term magnetic saturation is therefore inappropriate. In designing circulators, it is a very common design decision to assume that the ferrite being biased is saturated, resulting in a ferrite magnetization equal to the ferrite's magnetic saturation point $4\pi M_S$. This is not always the case, such as in a self-biased circulator [1], a special case of a below resonance circulator.

2.2.1 Above Resonance Circulator

The easiest to design of the three major circulator modes of operation is above resonance, as the extremely high biasing makes the ferrite so overly saturated that the impact of many materials and design parameters are insignificant. As the biasing creates a ferrimagnetic resonance frequency far above the operating frequency, resonance losses are small enough to ignore, meaning the imaginary parts of the ferrite permeability tensor are much smaller than their real parts and can be treated as zero. As a rule of thumb dating back to Bosma [25], the above resonance circulator utilizes an internal biasing field resulting in a ferrimagnetic resonance frequency ideally four times greater than the circulator operating frequency.

$$|\mu'| \gg |\mu''| \qquad |\kappa'| \gg |\kappa''| \tag{2.10}$$

Additionally, $\mu \gg \kappa$, allowing the simplification that $\mu_{eff} = \mu$. This unfortunately also leads to a minimal splitting between the split modes in the ferrite, as κ/μ is minimal. The operating frequency and operational bandwidth lie between these frequencies, forcing an above resonance circulator to have minimal bandwidth. While an increasing magnetic saturation corresponds to higher bandwidth, the dramatic increase in the biasing field leads to an overall smaller bandwidth than can be found in the below resonance circulators.

While bandwidth is minimal, the strong biasing ensures that the ferrite's magnetization vector requires a significant amount of RF signal power (and thus high microwave magnetic field H_{RF}) to deviate in direction from the externally applied DC biasing field. As spin-waves (discussed further in Section 2.4) require this deviation, the power handling of the ferrite component of an above resonance circulator is almost arbitrarily high, often in megawatts [26].

2.2.2 Below Resonance Circulator

Below resonance circulators are often considered the most difficult type of circulator to design, as the weak biasing allows resonance losses and other effects to be more prominent than in above resonance circulators. As such, the approximations for the above resonance circulators fall apart. Here, the assumption that the ferrite being biased is magnetically saturated matters, as it is often assumed the ferrite is just saturated, meaning an internal bias of 0 Oe and a magnetization equal to the magnetic saturation point. This assumption leads to a rule of thumb on the upper limit on the magnetic saturation value that can be used for a given frequency, expressed as:

$$4\pi M_S < \frac{f}{\gamma} - H_a \tag{2.11}$$

where H_a is the anisotropy field of the ferrimagnetic material, a measure of the difficulty of changing the direction of magnetization [27]. It should be noted that this inequality does not present a hard limit but is rather a rule of thumb. A below resonance circulator can utilize a magnetic saturation higher than the recommended maximum as long as the design engineer takes into account that the ferrite will not be fully magnetized at lower frequencies in the pass band. This comes at the cost of increased loss at these frequencies, but an overall higher bandwidth can be achieved.

As both internal bias and magnetic saturation are virtually set in stone from the beginning in a below resonance circulator, several simplifications can be made to make the design process as comparatively simple as an above resonance circulator:

$$\begin{gathered} \mu' \cong 1 \\ \mu_{eff} \cong 1 - \kappa^2 \end{gathered} \tag{2.12}$$

Due to this simplification, the effective permeability in a below resonance circulator is less than one, resulting in a ferrite resonator with a much larger radius than in an above resonance circulator, as can be seen in (2.25).

The resonance mode splitting can be measured by the ratio of the ferrite permeability tensor κ/μ as previously mentioned, allowing one a sense of the bandwidth that is attainable, with a larger ratio corresponding to higher bandwidth.

2.2.3 Resonance Circulator

The final type of mode of operation remaining to be discussed is the resonance region. While a circulator operating in this region can technically exist, they are so lossy as to be of virtually no use. At the ferrimagnetic resonance frequency, ferrites exhibit near-complete absorption of energy, resulting in nearly an unusably high insertion loss. As such, one of the only types of ferrimagnetic devices that use this region is two-port isolators. These isolators utilize an off-center slab of ferrite biased such that energy is absorbed by exploiting the interaction between the direction of circularly polarized waves in the ferrite coinciding with the direction of election precession from the bias in only one direction of propagation [15]. Resonance isolators, by definition, operate at resonance, allowing only minimal bandwidth. Unless the waveguide in question is loaded with a thermally conductive dielectric, power handling is minimal due to poor heat transfer away from the ferrite. This leads to an increase in ferrite temperature, decreasing its magnetic saturation value. As the externally applied bias remains constant, the internal bias in the ferrite will increase, increasing the resonance frequency and thus the operational frequency of the isolator.

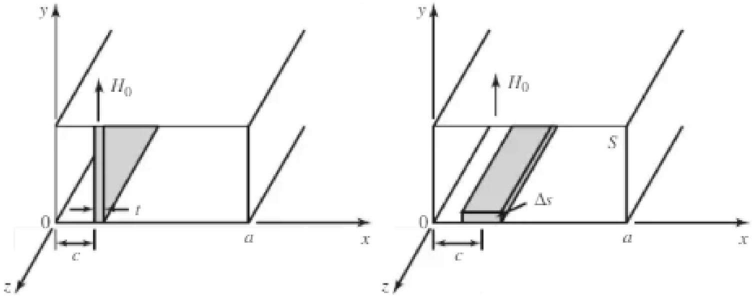

Figure 2.8: Waveguide-based isolator utilizing a ferrite slab, biased perpendicular to the direction of wave propagation. Depicted are an E-plane slab (left), and an H-plane slab (right), as depicted in [15].

A variety of other circulator types exist that use any combination of the three modes of operation but use uncommon or unconventional implementation methods and, as such, are much rarer than the commonly seen ferrimagnetic junction circulator. While a ferrimagnetic circulator with more than three ports can be achieved by chaining circulators together as in Figure 2.9, a Faraday rotation can be employed to achieve a similar effect by inserting a ferrimagnetic cylinder in the middle of a waveguide, biased along the cylinder axis. Strategic rotation of the output ports allows a similar non-reciprocal scattering matrix.

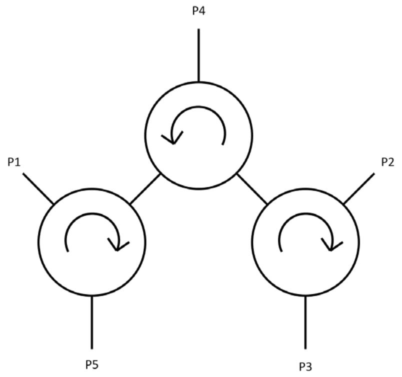

Figure 2.9: Architecture of an arbitrarily high port circulator composed of chained together three-port circulators.

$$[S] = \begin{bmatrix} 0 & 0 & 0 & 0 & 1 \\ 1 & 0 & 0 & 0 & 0 \\ 0 & 1 & 0 & 0 & 0 \\ 0 & 0 & 1 & 0 & 0 \\ 0 & 0 & 0 & 1 & 0 \end{bmatrix} \tag{2.13}$$

2.3 Below Resonance Operation – Closed-Form Modeling

Up to this point, the mathematics behind the circulator has only been glazed over, or vague trade-offs mentioned but not quantified. To minimize the spreading of information, this section of the thesis is meant as a beginning-to-end guide to the design of a general ferrimagnetic below resonance junction circulator. While some standard simplifications will be made, they will be preceded by the full closed-form variation of the equation where applicable.

A ferrimagnetic junction circulator is a device composed of a microstrip or stripline architecture, where three transmission lines meet at 120° angles of each other between a ferrimagnetic medium. A ferrimagnetic junction circulator can be modeled as a first-order filter, with a shunt RLC resonator representing the ferrimagnetic junction itself. It is worth noting that the reactive portion of the resonator can be modeled as a quarter-wavelength transmission line, with a line impedance of $Z = \pi/(4B')$, where B' denotes the slope of the ferrite's input susceptance near the resonant frequency. Meanwhile, the resistive element of the model represents the inverse of the conductance, $R = 1/G_r$, near the junction's resonance frequency. The RLC and admittance descriptions are related using:

$$R = \frac{1}{G_r} \qquad L = \frac{1}{2\pi f_0 Q_L G_r} \qquad C = \frac{Q_L G_r}{2\pi f_0} \tag{2.14}$$

where Q_L is the loaded quality factor of the ferrite junction defined later in this chapter. The input impedance, when viewed on a Smith chart, produces a very nicely shaped impedance response that is centered on the real axis, mirrored on either side. It has historically been found that one of the best ways to impedance match this response over a wide range of frequencies is via quarter-wave transformers implemented on the transmission lines just outside of the ferrite and conductor junction. With no transformers, the return loss of the junction has only one reflection null with poor performance at the resonance frequency determined by the ferrite material, junction radius, and applied bias, along with the input conductance in circulators generally being much lower than the standard system impedance of 50 Ω. When a single transformer is added with a carefully chosen impedance, the return loss can be made to have two nulls, as the response of the circulator has been matched to slightly over 50 Ω at the center frequency, with the response at the corner frequencies "folded" over 50 Ω. This process can be generalized, with the number of reflection nulls capable of being generated being equal to $n_{RL,null} = n_{QWT} + 1$. As will be discussed later in this section, the process of choosing the correct impedances for each transformer becomes exponentially more difficult as transformers are added, forcing a practical upper limit on two or three transformers when using this method. Fortunately, the transformer impedance solutions are well defined for a transformer network consisting of one or two transformers, thanks to Helszajn [28]. To determine the impedance matching circuit required, one must simply know the operational frequency band and the minimum return loss of the circulator in the passband. A circulator designer can also specify and design for a maximum return loss, which can improve broadband performance and increase the allowable trade-off space with other parameters at the cost of increased computational complexity. The terms used regardless of quarter-wave transformer quantity are:

$$BW = \frac{f_2 - f_1}{f_0} = 2\frac{f_2 - f_1}{f_2 + f_1}$$
$$S_{max} = \frac{1 + 10^{-RL_{min}/20}}{1 - 10^{-RL_{min}/20}} \qquad S_{min} = \frac{1 + 10^{-RL_{max}/20}}{1 - 10^{-RL_{max}/20}}$$
$$K^2 = \left(\frac{S_{min} - 1}{2\sqrt{S_{min}}}\right)^2 \qquad \varepsilon^2 = \left(\frac{S_{max} - 1}{2\sqrt{S_{max}}}\right)^2 - K^2 \tag{2.15}$$
$$\theta_0 = \frac{\pi}{4}(2 - BW) \qquad \beta = tan^2\theta_0 + \frac{sin\theta_0}{cos^2\theta_0}$$

where, f_1 and f_2 are the lower and upper frequencies in the passband, and RL_{min} and RL_{max} are the minimum and maximum return loss in dB permitted in the passband. All other variables are newly defined in the set of equations. Using the variables established in (2.15), one can calculate the impedance matching network for a one transformer network (n = 2) using:

$$a = K^2 + \varepsilon^2 \qquad b = 2\beta\varepsilon^2 - K^2 \qquad c = \beta^2\varepsilon^2$$
$$n_1 = \sqrt{2\sqrt{(a+1)c} - b + 1} - \sqrt{2\sqrt{ac} - b}$$
$$n_2 = \sqrt{a+1} - \sqrt{a} = \frac{1}{\sqrt{S_{max}}} \qquad d_0 = 2\sqrt{c} \tag{2.16}$$
$$G_r = \frac{n_1^2}{Z_0} \qquad B' = \frac{\pi n_1 d_0}{4Z_0} \qquad Q_L = \frac{B'}{G_r} = \frac{\pi d_0}{4n_1}$$
$$Z_{QWT1} = \frac{n_2 Z_0}{n_1} = \sqrt{\frac{Z_0}{S_{max}G_r}}$$

The input impedance at the center frequency can be calculated as:

$$Z_{in} = \frac{Z_{QWT}^2}{G_r} \tag{2.17}$$

For a circulator using a two quarter-wave transformer impedance matching network (n = 3), the terms used to calculate the quarter-wave transformer impedances and resonator admittance are:

$$\begin{gathered}
p = -\left[2 + \frac{\varepsilon^2}{1+K^2}\left(\frac{2+sin\theta_0}{cos\theta_0}\right)^2\right] \\
q = 1 - \frac{2\varepsilon^2}{1+K^2}\frac{sin\theta_0(2+sin\theta_0)(1+sin\theta_0)}{cos^2\theta_0(1-sin\theta_0)} \\
r = -\frac{\varepsilon^2}{1+K^2}\left(tan\theta_0\frac{1+sin\theta_0}{1-sin\theta_0}\right)^2 \\
a = q - \frac{p^2}{3} \qquad b = 2\left(\frac{p}{3}\right)^3 - \frac{pq}{3} + r \\
n_{32} = \sqrt{1+K^2}
\end{gathered} \tag{2.18}$$

The next set of equations depend on the value of $c = (b/2)^2 + (a/3)^3$. If $c \geq 0$, the next set of equations are:

$$\begin{gathered}
A = \sqrt[3]{-\frac{b}{2} + \sqrt{\left(\frac{b}{2}\right)^2 + \left(\frac{a}{3}\right)^3}} \qquad B = \sqrt[3]{-\frac{b}{2} - \sqrt{\left(\frac{b}{2}\right)^2 + \left(\frac{a}{3}\right)^3}} \\
X_1 = -\left(\frac{A+B}{2} + \frac{p}{3}\right) \qquad X_2 = \frac{\sqrt{3}}{2}(A-B) \\
t_1 = \sqrt{A+B-\frac{p}{3}} \qquad |t_2|^2 = \sqrt{X_1^2 + X_2^2} \\
t_2 + t_2^* = \sqrt{2\left(X_1 + \sqrt{X_1^2 + X_2^2}\right)} \\
n_{22} = \sum\nolimits_1 \sqrt{1+K^2} = (t_1 + t_2 + t_2^*)\sqrt{1+K^2} \\
n_{12} = \sum\nolimits_2 \sqrt{1+K^2} = [|t_2|^2 + t_1(t_2 + t_2^*)]\sqrt{1+K^2} \\
n_{02} = \sum\nolimits_3 \sqrt{1+K^2} = t_1|t_2|^2\sqrt{1+K^2}
\end{gathered} \tag{2.19}$$

If $c < 0$, then one uses the next set of equations to calculate n_{22}, n_{12}, and n_{02}:

$$\phi = tan^{-1}\left[-2\frac{\sqrt{-\left(\frac{b}{2}\right)^2 - \left(\frac{a}{3}\right)^3}}{b}\right]$$

$$X_1 = \sqrt{2\left(\sqrt{-\frac{a}{3}}\, cos\frac{\phi}{3}\right) - \frac{p}{3}}$$

$$X_2 = \sqrt{-\frac{p}{3} - \left(\sqrt{-\frac{a}{3}}\, cos\frac{\phi}{3}\right) + \left(\sqrt{-a}\, sin\frac{\phi}{3}\right)} \tag{2.20}$$

$$X_3 = \sqrt{-\frac{p}{3} - \left(\sqrt{-\frac{a}{3}}\, cos\frac{\phi}{3}\right) - \left(\sqrt{-a}\, sin\frac{\phi}{3}\right)}$$

$$n_{22} = \sum\nolimits_1 \sqrt{1 + K^2} = (X_1 + X_2 + X_3)\sqrt{1 + K^2}$$

$$n_{12} = \sum\nolimits_2 \sqrt{1 + K^2} = (X_1 X_2 + X_2 X_3 + X_1 X_3)\sqrt{1 + K^2}$$

$$n_{02} = \sum\nolimits_3 \sqrt{1 + K^2} = (X_1 X_2 X_3)\sqrt{1 + K^2}$$

The next step to calculate the impedance values for the $n = 3$ quarter-wave transformer matching network is the calculation of n_{21}, n_{11}, and n_{01}. If no upper limit was set on circulator return loss and isolation ($S_{min} = 1$), then we use the following set of equations:

$$n_{31} = K \qquad n_{21} = \varepsilon\frac{2 + sin\theta_0}{cos\theta_0}$$
$$n_{11} = 0 \qquad n_{01} = \varepsilon\, tan\theta_0 \frac{1 + sin\theta_0}{1 - sin\theta_0} \tag{2.21}$$

However, if an upper limit on return loss and isolation was specified, or if desired by the circulator engineer, then one runs through equations (2.16) – (2.20) once again, replacing all instances of $1 + K^2$ with K^2. When n_{32}, n_{22}, n_{12}, and n_{02} are reached, they are renamed n_{31}, n_{21}, n_{11}, and n_{01}, respectively. Finally, resonator admittance and transformer impedances to achieve the desired bandwidth, return loss, and isolation are calculated as:

$$
\begin{gathered}
n_3 = n_{32} - n_{31} \qquad n_2 = n_{22} - n_{21} \\
n_1 = n_{12} - n_{11} \qquad d_0 = n_{02} + n_{01} \\
G_r = \frac{n_1^2}{Z_0} \qquad B' = \frac{\pi n_1 d_0}{4Z_0} \qquad Q_L = \frac{B'}{G_r} = \frac{\pi d_0}{4n_1} \\
Z_{QWT1} = \frac{Z_0 n_2}{n_1 + n_3} \qquad Z_{QWT2} = Z_{QWT1}\frac{n_3}{n_1}
\end{gathered}
\tag{2.22}
$$

With quarter-wavelength transformers, the input impedance of the circulator at the center frequency is calculated to be:

$$
Z_{in} = \frac{1}{G_r}\left(\frac{Z_{QWT1}}{Z_{QWT2}}\right)^2 \tag{2.23}
$$

Once these values have been calculated, the next step is generating the desired resonator admittance at the passband center frequency. If no solution is found for the specified parameters, or if the given solution is unrealizable, one can run through the equations again for a variety of pairings of maximum and minimum return loss to achieve a variety of resonator admittance and transformer impedances.

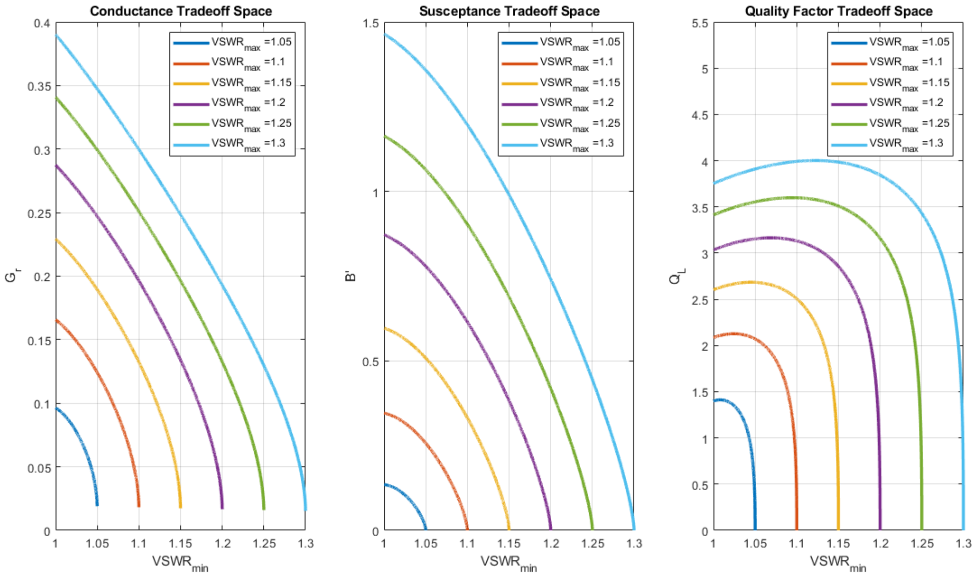

Figure 2.10: Ferrite resonator characteristics for varying levels of minimum and maximum VSWR in the passband. Bandwidth assumed constant at 20%, with one quarter-wave transformer used.

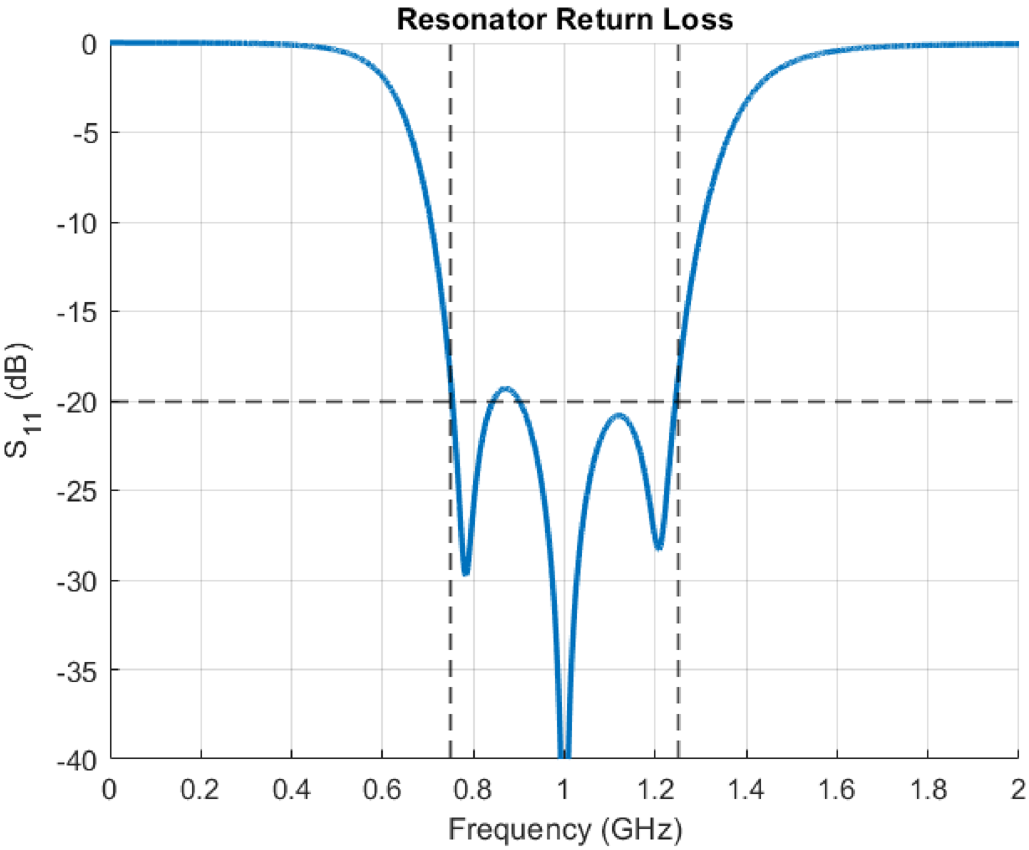

Figure 2.11: Example return loss response for an arbitrary input of $S_{min} = 1.00$ $(RL_{max} = \infty\ dB)$, $S_{max} = 1.22$ $(RL_{min} = 20\ dB)$, BW = 500 MHz (0.75 GHz to 1.25 GHz) generates a shunt RLC resonator with R = 1.2742 Ω, L = 132.0 pH, C = 191.9 pF, Z_{QWT1} = 21.4812 Ω, Z_{QWT2} = 3.4292 Ω.

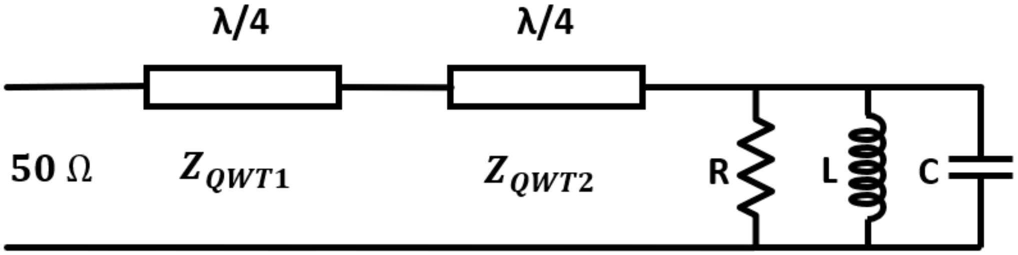

Figure 2.12: Circuit schematic for the return loss response seen in Figure 2.11.

As the ferrites used in ferrimagnetic junction circulators act as resonators, they have a loaded and unloaded quality factor Q_L and Q_U, respectively. The loaded quality factor derived by Fay and Comstock [29] uses the ferrite's stored energy and the power coupled to the stripline transmission line coupled to the ferrite junction. While an equation for the true unloaded quality factor exists, it can be difficult to realistically ascertain several of the parameters involved. Therefore, Comstock derives an approximation for the general loaded and unloaded quality factor of a below resonance circulator:

$$Q_L = 1.48\frac{2\pi f R^2 \varepsilon_r \varepsilon_0}{G_r d}$$

$$Q_U = \frac{1}{\left|\frac{\mu_{eff}''}{\mu_{eff}'}\right| + tan\delta} \cong \frac{1}{\frac{\gamma^2(4\pi M_S)}{2f^2} + tan\delta} \tag{2.24}$$

where R is the effective radius of the disc-shaped ferrite junction, ε_r is the relative permittivity of the ferrite material, G_r is the conductivity of the ferrite at resonance (not the FMR frequency), and d is the thickness of the ferrite disks.

Once the ferrite material has been chosen, the next step in the below resonance circulator design process is determining the method of transmission line integration. Microstrip, stripline, and waveguide circulators are all common in COTS devices. Typically, stripline circulators are more common than microstrip circulators, as they are less lossy and capable of greater bandwidths due to not having a frequency-dependent effective dielectric constant. As such, microstrip circulators are typically only used when the specifications of a circulator are not demanding. Waveguide circulators are almost always below resonance and are capable of extremely low insertion loss over a very broad frequency range. Regardless of the chosen implementation, the overall mathematics do not differ significantly as they are in terms of the ferrite characteristics and transformer impedances. Where they do differ, the differences will be noted and discussed.

At this point, the shape and radius of the ferrite are chosen, such that it resonates at the center frequency of the passband. The most common shapes for ferrites in ferrimagnetic circulators are disc, triangular, and hexagonal geometries. Regardless of the shape, the ferrite resonators are all defined to have a radius equal to the distance between the center of a face on the ferrite, and its farthest edge, as in Figure 2.14. The radius of the ferrite is then calculated using:

$$R = \frac{(kR)}{2\pi f_0 \sqrt{\mu_{eff}\mu_0\varepsilon_r\varepsilon_0}} = \frac{c\ (kR)}{2\pi f_0 \sqrt{\mu_{eff}\varepsilon_r}} \tag{2.25}$$

where c is the speed of light, f_0 is the resonant frequency (not the FRM frequency), and μ_{eff} is the effective relative permeability of the ferrite under biasing. The term kR is a shape-dependent term that additionally dependent on biasing. Values of kR for common center conductor shapes when weakly magnetized (i.e., in below resonance circulators where $\kappa/\mu < 0.3$) are listed in Table 2.1 [30].

Table 2.1: Shape factor (kR) values for common junction shapes

Junction Shape	kR Value
Disc	1.84
Triangle (Side Coupled)	2.45
Triangle (Apex Coupled)	2.45
Hexagonal	2.00

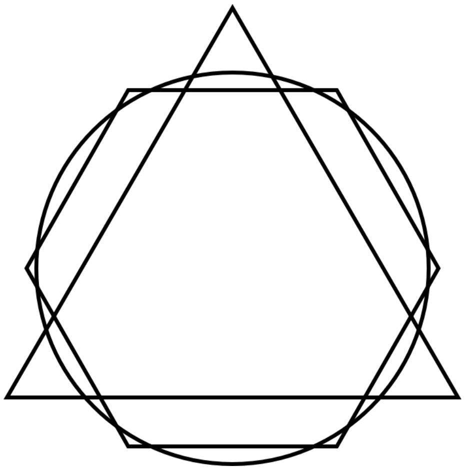

Figure 2.13: Overlayed ferrite geometries with equal resonant frequencies.

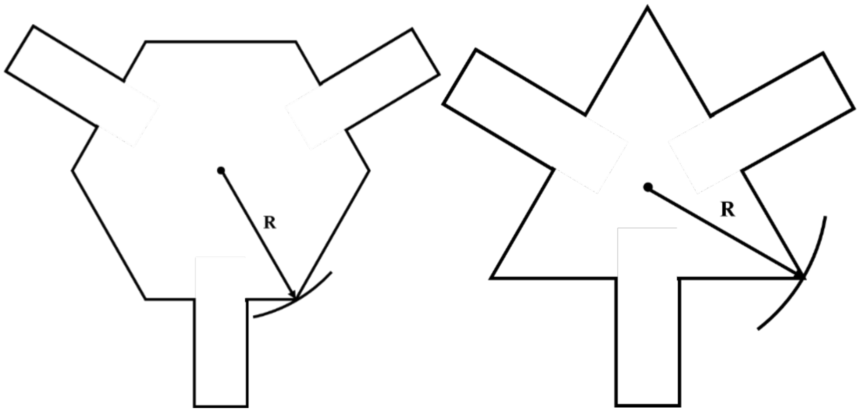

Figure 2.14: Definitions of radius for a center conductor geometry of a hexagon (left) and a side coupled triangle (right).

With the ferrite shape chosen, the center conductor geometry and ferrite thickness must be decided upon in order to generate the input admittance at resonance that is desired for maximum bandwidth. Typically, the shape of the ferrite aligns with the shape of the center conductor, greatly simplifying the design process. Exceptions to this include “wye” center conductor geometries, either with or without stubs. The center conductor geometry most strongly impacts the resonator’s conductance (G_r) and susceptance slope (B') largely inversely of each other, with little overall impact to the loaded quality factor. The resonator’s input conductance and susceptance slope both vary inversely with ferrite thickness. Because of these tradeoffs, if a significantly different resonance conductance is desired, the most effective method is altering the shape and orientation of the center conductor. With the same ferrite thickness and resonance frequency, a side-coupled triangular resonator will have a conductance on the order of three times higher than a disk resonator, with an apex-coupled resonator a conductance one-third of a disk resonator. This is due to the increased shunt resonator characteristic introduced by the electrically long 90° shunt stubs as seen from the lines coming into the junction for the side-coupled triangle and lack thereof for the apex-coupled triangle.

The ferrite radius thus calculated has assumed there are no fringing fields at the boundary between the ferrite and the surrounding dielectric. These fringing fields lead to the ferrite appearing larger than reality, lowering the center frequency. To compensate, the effective radius must be calculated, and the true radius of the ferrite must be adjusted such that its effective radius is equal to the previously calculated radius. To calculate the effective radius, one can treat the center conductor in the circulator as a disk between ground planes. For a stripline structure, Wheeler [31] derives the capacitance between the center conductor and equally spaced ground planes, which can be used to calculate the effective radius:

$$R_{eff} = R_{true}\frac{C_2}{C_a}$$

$$C_a = \frac{\varepsilon_0\varepsilon_r\pi R^2}{d} \tag{2.26}$$

$$C_2 = \left(8R\varepsilon_0\frac{1+\varepsilon_r}{2} + \frac{2\varepsilon_0\varepsilon_r R^2}{d}\right)\left(1 - \frac{1}{4 + 2.6\frac{R}{d} + 2.9\frac{d}{R}}\right)$$

With the operational mode, biasing level, and ferrite material chosen, the desired resonator admittance known, and the radius calculated, the next step is choosing the coupling angle between the transmission line and the center conductor junction, where the coupling angle (ψ) is defined as $\psi = sin^{-1}(W/2R)$, where W is the width of the transmission lines at the junction. Typically, the ideal value is interpolated from a table [32], but it can be directly calculated using (2.27) by choosing a coupling angle that provides the desired input admittance:

$$Z^0 = Z_0 + Z_{-3} + Z_3 \qquad Z^+ = Z_1 + Z_{-2} \qquad Z^- = Z_{-1} + Z_2$$

$$Z_n = \frac{j3\sqrt{\mu_{eff}}Z_\psi sin^2(n\psi)}{n^2\pi\psi}\left[\frac{1}{\frac{J_{n-1}(kR)}{J_n(kR)} - n\left(\frac{1 + \left|\frac{\kappa}{\mu}\right|}{kR}\right)}\right]$$

$$A = -\frac{1}{2}(Z^+ + Z^-) + Z^0 \qquad B = \frac{\sqrt{3}}{2}(Z^+ + Z^-) \tag{2.27}$$

$$R_{in} = \frac{3A^2B - B^3}{3(A^2 + B^2)} \qquad X_{in} = Z^0 - \frac{AR_{in}}{B} \qquad Z_{in} = R_{in} + jX_{in}$$

$$G = \frac{R_{in}}{R_{in}^2 + X_{in}^2} \qquad B = -\frac{X_{in}}{R_{in}^2 + X_{in}^2} \qquad B' = \frac{\omega}{2}\frac{dB}{d\omega}$$

One ultimately obtains the required ferrite thickness from (2.24) in order to generate the correct G_r. The dielectric constant of the dielectric substrate surrounding the ferrite medium is determined by the need to maintain the junction coupling angle and the impedance of the first quarter-wave transformer. If the circulator engineer does not have control over the substrate thickness and/or dielectric constant of the substrate, returning to (2.15) with new parameters is likely required.

2.4 High Power Considerations

In a ferrimagnetic device, there are two principle worries an engineer must consider in high power conditions: spin-waves and ferrite overheating. The former is capable of absorbing all incident power in the device, and the latter capable of mismatching the circulator, degrading performance.

In addition to spin-waves, ferrite overheating from high levels of power is of principle concern, leading to a severe impedance mismatch as the ferrite's resonance frequency for the externally applied bias and resonance conductance shift. This is due to the magnetic saturation value of a ferrimagnetic material changing dramatically with temperature, which is discussed in detail in Section 2.5. In order to prevent the ferrite's core temperature from changing beyond the ambient temperature, steps must be taken in cooling the material. The steps necessary vary wildly on the tolerance of the circulator specifications and the maximum power the ferrite is expected to handle. If only low power levels are expected and the specifications are minimally demanding (i.e. low return loss and bandwidth), a thermally conductive path in planar contact with the ferrite can prove enough to assuage the impact of heating from high RF signal levels [33]. Additional methods include heat sinks and fan cooling. In extreme cases, water cooling could be used to keep ferrite temperatures low. Due to the extreme difficulty of incorporating water cooling into a commercial off-the-shelf (COTS) microwave device, this method is rarely used. The most common cooling method is thermally conductive, high surface area node physically in contact with the device's ferrites [33].

Spin-waves will be excited in the ferrite medium is the magnetic component of the RF signal (H_{RF}) is of a sufficient magnitude at any given location. As any power above the critical limit will effectively be lost, preventing power level spikes in any given location in the ferrite medium is essential. A common source of location-specific power level spikes are transmission line discontinuities in width. In a ferrimagnetic circulator, this is almost always from the transmission line to the center conductor transition in the ferrite region. Power levels in a below resonance circulator can be increased by removing these discontinuities, such as with tapering.

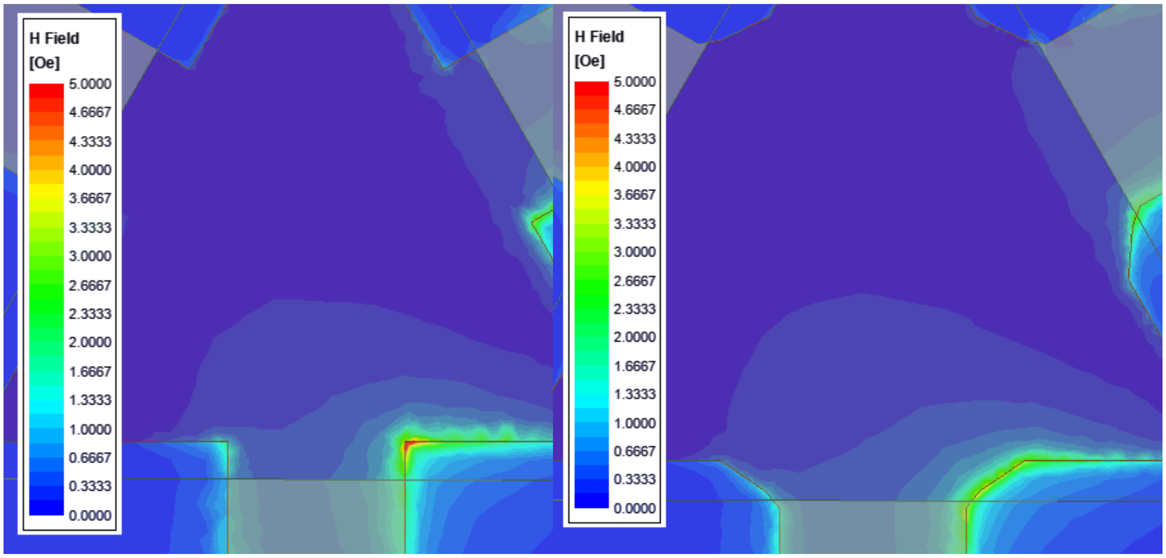

Figure 2.15: Close up of H_{RF} magnitude, with (right) and without (left) tapering, both at the same phase. With the inclusion of a taper, an equivalent junction will produce fewer local maximums of magnetic energy with lower magnitudes.

The point at which spin-waves will begin to be excited in a below resonance ferrimagnetic circulator is fortunately simple, by calculating the spin-wave line width [34]:

$$\Delta H_k = \frac{H_{RF}\gamma(4\pi M_S)}{f} \tag{2.28}$$

where, H_{RF} is the magnitude of the magnetic field intensity component of the propagating signal, and as such, is proportional to the square root of the incident power. All the other variables are as defined in earlier sections of this thesis. As frequency is in the denominator, one can expect that below resonance circulators operating at higher frequencies will have lower power handling than similarly designed circulators operating at lower frequencies. The spin-wave line width is sometimes, but not always, listed on a ferrite's datasheet. This value is somewhat controlled by the manufacturer of the ferrite material, as it is largely controlled by the grain size of the ferrite. The typical range for the average grain size is on the order of 10 to 20 microns [35]. This grain size is capable of being reduced at the cost of a significantly increased price. A smaller grain size corresponds to higher spin-wave line width and thus higher power handling.

In a below resonance circulator, the power handling will almost always be limited by the spin-wave line width. For an above resonance circulator, the extreme levels of magnetization from the bias make the ferrite's magnetization vector difficult to misalign, pushing the typical power handling into the megawatts. It is, therefore, only in the above resonance circulators that one needs to account for other high power considerations, such as the power capacity of a transmission line due to breakdown voltage. Generally, the power capacity of a transmission line in a printed circuit board implementation will be measured in kilowatts [26].

The final major limiter in power handling for junction circulator comes from the heat generated by the power dissipated in the dielectric and ferrite regions of the transmission line, as no substrate is completely lossless. The maximum power, in this case, is whatever leads to the maximum rise in temperature the circulator engineer allows. To compute the maximum power in this case, one must know the maximum temperature rise ΔT, the thermal conductivity of the substrate σ_T, the insertion loss (IL) per unit length, and the dimensions of the transmission line. The relation is thus derived from [33] using simple rearrangement:

$$P_{in,max} = \frac{\Delta T_{max}\ \sigma_T\ A}{d(1 - 10^{-IL_{dB}/10})} \tag{2.29}$$

where d is the distance between the center conductor and the corresponding ground plane. A refers to the cross-sectional area that encompasses the majority of the fields passing through the transmission line, effectively being the area that is being heated.

2.5 High Temperature Considerations

As mentioned previously, the magnetic saturation point of a given ferrimagnetic material changes significantly as a function of temperature. Generally, ferrites are only ferrimagnetic for a range of temperatures, outside of which point the material becomes paramagnetic [14]. This temperature range is commonly referred to in specifications as the storage temperature of the device. The upper temperature at which a ferrite loses its ferrimagnetic properties is commonly known as its Curie Temperature. To the best of the author's knowledge, there does not exist a name for the lower temperature point, which is seen only for conditions of extreme cold or for heavily doped ferrimagnetic materials with very low magnetic saturation values. Outside of this temperature range, the ferrite material becomes paramagnetic.

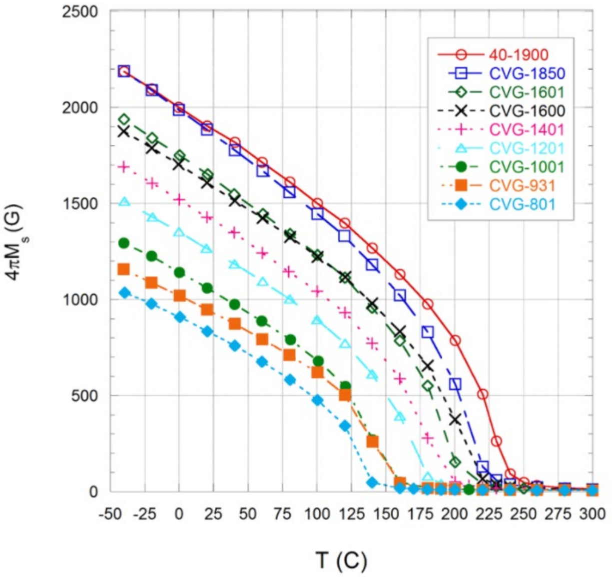

Figure 2.16: Magnetic saturation versus temperature for a variety of calcium vanadium garnet (CVG) ferrites, from [24]. Materials are named after their chemical composition, followed by their magnetic saturation at room temperature.

The second major consideration for a circulator at high temperatures is thermal expansion, as circulators are almost invariably tightly enclosed devices with multiple discrete materials of varying thermal conductivities and thermal expansion coefficients. Regardless of construction, all circulators will be composed of a dielectric material, a ferrimagnetic material, and an electrical conductor. Typically, the thermal expansion coefficient for a ceramic material is much lower than the thermal expansion coefficient of metals [36]. Unless one is working at temperatures greatly exceeding 100 °C, even the worst case of thermal expansion will be negligible. As an example, a meter of copper (thermal expansion coefficient of $16 * 10^{-6} \frac{m}{m\,°C}$) will expand a mere 1.2 mm when being heated to 100 °C from 23°C.

2.6 Conclusions

The basics of ferrimagnets and the inherent limitations as they relate to RF and microwave devices, specifically circulators, were presented. The large variety of potential devices and functions that are made realizable and practical by the introduction of ferrimagnetic materials were described, and the varying modes of operation for circulators were discussed and characterized.

The closed-form expressions for the design of broadband and high-performance circulators were detailed, with several example circulator resonator performances shown, as well as the trade-off spaces shown. Important temperature and power effects involving ferrimagnetic materials were described, which will be utilized to allow the designed circulator to operate at high temperature and high power conditions.

With the basics of ferrimagnetic devices now known to the reader, the design of the high power, high temperature, and high performance surface mountable circulator can now be detailed.

Chapter 3

Ferrimagnetic Circulator Design

A high temperature and high power ferrimagnetic below resonance circulator with surface mountable technology integration is designed using the information as presented in Chapter 2. This circulator design is then simulated using a popular finite element method (FEM) electromagnetic solver, Ansys HFSS. Due to the varying layers of design involved in ferrimagnetic circulators, each part of the simulation process is designed and simulated in stages. The interwoven nature of the simulations, the closed-form design of the circulator is done up front, with the simulations created at the end of the process. As this thesis assumes the reader is largely inexperienced with ferrimagnetics, the ferrite junction portion of the simulations involves a great deal of stress-testing the simulation to uncover the trade-off space near the discussed design solution. The circulator designed and simulated in this section will be later fabricated and measured in Chapter 4.

3.1 Electrical Circuit Design

A ferrimagnetic below resonance circulator was designed for the specifications listed in Table 3.1. A summary of the critical design variables is listed in Table 3.2. Due to the requirement of extremely wide bandwidth, considerations for an above resonance design were quickly abandoned despite the high power requirement. While a below resonance circulator can compensate for high power requirements by choosing a ferrite material with a high spin-wave line width ΔH_k, achieving the required amount of frequency splitting in the lowest order mode for an above resonance circulator is not possible using currently known and understood methods due to the high internal field inside the ferrite that is by definition present. While an increase in magnetic saturation generally corresponds to an increase in bandwidth, all else being equal, an increase in magnetic field biasing leads to a decrease in bandwidth. Overall, the impact of the biasing is felt more strongly than the magnetic saturation, even if the biasing is kept minimal.

Table 3.1: Summary of below resonance circulator specifications

Parameter	Value
Bandwidth	S-band (2 – 4 GHz)
Return Loss (RL)	≥ 20 dB
Insertion Loss (IL)	≤ 0.8 dB
Isolation (ISO)	≥ 20 dB
Operational Temperature	85°C to 100°C
Storage Temperature	-40°C to 120°C
Power Handling	≥ 50 W (47 dBm)
Integration	Surface Mount Technology (SMT)
Size	≤ 1” x 1” x 0.5”

The decision to design a below resonance circulator based on the specifications leads to the next step of the design process, the choice of ferrite material. Equation (2.11) shows us that based on the minimum frequency in the desired passband, the recommended maximum magnetic saturation $4\pi M_S$ is approximately 715 G in order for the ferrite to be fully magnetically saturated at all frequencies. However, as a higher magnetic saturation allows for broader bandwidth [28], it was decided to go slightly above the rule of thumb maximum magnetic saturation to 900 G. To compensate for the change in $4\pi M_S$ versus temperature, the chosen value was even higher. In the end, the material used was Pacific Ceramics’ CVG-1201, which has a magnetic saturation of 1200 G at room temperature, and 920 G at 100 °C. At the time the material was purchased and chosen, the spin-wave line width of this material not published by the vendor, so the 2.0 Oe ΔH_k spin-wave line width was not taken into account in the initial prototype.

Stripline technology was chosen for the structure over microstrip in order to prevent dispersion of the effective dielectric constant over frequency. In order to minimize the footprint of the device (1” x 1”), a high dielectric constant would be required, making the elimination of frequency-dependent changes in the effective dielectric constant critical.

Additionally, the choice of stripline increases power handling by roughly a factor of two by spitting the microwave power between two ferrites. The increase is not exactly two due to a degree of fringing fields outside of the dielectric substrate in a microstrip circuit when a similar substrate with an effective permittivity equal to the relative permittivity of the stripline. The effective permittivity of a microstrip line is given by [37]:

$$\varepsilon_{r,eff} = \frac{\varepsilon_r + 1}{2} + \frac{\varepsilon_r - 1}{2}\left[\left(1 + 12\left(\frac{h}{W}\right)\right)^{-1/2} + 0.04\left(1 - \left(\frac{W}{h}\right)\right)^2\right] \quad when\ \frac{W}{h} < 1$$
$$\varepsilon_{r,eff} = \frac{\varepsilon_r + 1}{2} + \frac{\varepsilon_r - 1}{2}\left[\left(1 + 12\left(\frac{h}{W}\right)\right)^{-1/2}\right] \quad when\ \frac{W}{h} \geq 1 \qquad (3.1)$$

The decision was made to utilize a two quarter-wave transformer impedance network, despite the dramatic increase in size, as the substrate's dielectric constant could be increased to compensate. A thick side coupled triangular ferrite was utilized as it generated the desired resonator conductance (G_r) at the cost of somewhat increased ferrite thickness. In addition, for the same ferrite material and resonance frequency, a side-coupled triangle has the lowest footprint in the x-y plane of the common ferrite shapes.

With these preliminary decisions made, the required resonator admittance and quarter-wave transformer impedances were calculated using (2.15) – (2.22), for a maximum VSWR in the passband of 1.06, a minimum VSWR in the passband of 1.00, a bandwidth of 67%, and an ideal loaded quality factor of 0.54:

Table 3.2: Ideal Ferrite resonator electromagnetic characteristics

Parameter	Value
f_0	3 GHz
Gr	86 mS
B'	0.044
Q_L	0.54
ψ	0.36
Z_{QWT1}	37.8 Ω
Z_{QWT2}	18.3 Ω

For this conductance value, the desired coupling angle is calculated using (2.27) to be $\psi = 0.36$. For the specified return loss, isolation, and bandwidth specifications, sweeping S_{min} and S_{max} over all their possible values generate a range of values for resonator conductance G_r that allows the circulator to meet specifications, 0.7 S to 1 S, approximately. Using (2.24) and adjusting for the change from a disk to a side coupled triangular ferrite, this presents a ferrite thickness range of 2 mm to 2.9 mm. This range is reduced somewhat when one considers that the high dielectric constant substrate will put an upper limit on ferrite thickness to prevent the stripline ground plane to ground plane distance from exceeding a quarter-wavelength at the maximum frequency, where electrical distance is minimized. The dielectric constant of the substrate must also be high enough such that two quarter-wave transformers with a 3 GHz center frequency can fit inside a 1” x 1” space. Finally, the stripline must be thick enough that the second transformer with the higher impedance of 34.4 Ω does not become vanishingly small and simultaneously remain wide enough to carry 47 dBm, while the lower impedance line at the junction does not become larger than the junction or greater than a quarter-wavelength in width, as discussed further in Sections 2.4 and 3.5.2.

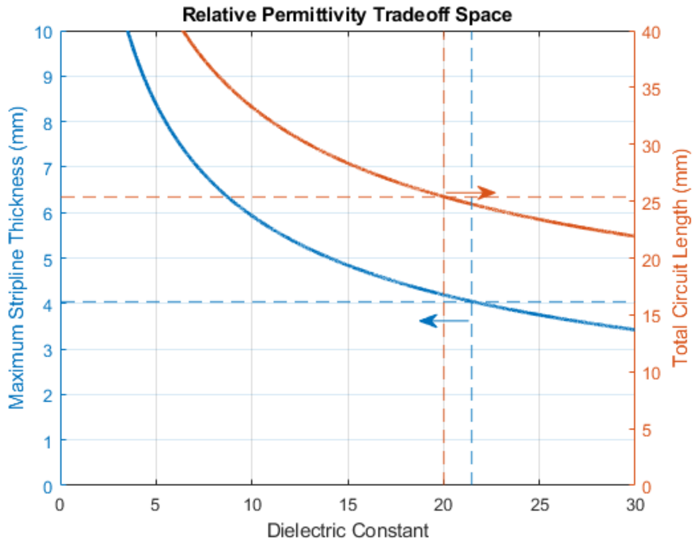

Figure 3.1: Trade-off space for ferrite thickness, and thus stripline ground plane to ground plane spacing. To maintain a maximum footprint of 1”x1”, the dielectric constant of the stripline substrate must be at least 20. To allow a ferrite thickness of 2 mm and a trace thickness of 50 µm without the stripline thickness exceeding one quarter-wavelength at the maximum frequency (4 GHz), the dielectric constant of the stripline substrate must be under 21.5.

These considerations in tandem narrow in on a single solution for the electromagnetic characteristics of the ferrite junction, as described in Table 3.2. In order to use existing commercially available materials, MCT-20 (ε_r = 20) procured from Island Ceramics was chosen for the dielectric substrate, with triangular CVG-1201 ferrites procured from Island Ceramics were chosen for the ferrite material. Due to the narrow band of solutions for thickness, as seen in Figure 3.1, the ferrites were chosen to be 2 mm in thickness. For this thickness, the effective radius of the ferrites to achieve a ferrimagnetic resonance at 3 GHz for the magnetic saturation and will be somewhere in the vicinity of 9.8 mm. An exact calculation is futile, as the kR values in Table 2.1 are only for weakly magnetized ferrites where the polder tensor elements satisfy the condition that $|\mu| \gg |\kappa|$, which is not the case here. For a highly magnetized below resonance circulator, kR values will drop to approximately half that in Table 2.1.

The center conductor, as is generally the case, was designed to be of approximately the same shape as the ferrite, with a somewhat smaller radius. An initial starting point of a center conductor radius 75% that of the ferrite was chosen, an oft-used rule of thumb in circulator design to simplify matters.

As the circulator was designed for below resonance operation, it was very susceptible to power loss from spin-waves. Rearranging (2.28), the maximum RF magnetic field intensity (H_{RF}) magnitude that could exist in the ferrite junction before exciting spin-waves is:

$$H_{RF} = \frac{f\,\Delta H_k}{\gamma\,(4\pi M_S)} = 2.33\ Oe \quad (3\ GHz,\ \ 23°C) \tag{3.2}$$

It was desired to remove any sharp corners in the center of the ferrite junction in order to spread out any local maximums of magnetic energy, as can be seen in an example Ansys HFSS simulation model in Figure 2.15. The largest source of local maximums of magnetic field intensity would be from the sharp transition from the stripline feeding lines to the triangular ferrite junction. Thus, a taper was included to smooth out the transition. Each triangular taper was defined to have a length equal to half the difference between the ferrite radius and the center conductor radius, allowing the taper to spread to the edge of the ferrite junction. The width of the taper on each side of the stripline was empirically set to be 1 mm, to prevent any unwanted changes in the input admittance of the ferrite junction.

3.2 Magnetic Biasing Circuit Design

Up to this point, the generation of the DC biasing field has been ignored in favor of discussing the ferrite's internal DC bias. Ultimately, in a ferrimagnetic junction circulator, it is desirable to fully saturate the ferrite material in question with a uniform external DC field. Typically, the shape of ferrites in this type of circulator can be modeled as a thin disk with a biasing normal to surface. Using equation (2.8), the required applied field for a ferrite of this type simplifies to:

$$H_{ext} = H_{int} + 4\pi M_S \tag{3.3}$$

This approximation does not hold with a ferrite disk with a high aspect ratio between height and radius or for a ferrite with an atypical shape, such as a triangle or hexagon. In this case, the demagnetization factors change significantly, ultimately requiring a smaller external field to accomplish the same internal field. The ferrites in the junction of the circulator described in this thesis are triangular, with a radius to height aspect ratio R/H of 4.25. The demagnetization factors for a thick disc-like shape polarized normal to the primary face are described in [30] to be determinable by the eccentricity e of the shape, given by:

$$e = \sqrt{4\left(\frac{R}{H}\right)^2 - 1} \tag{3.4}$$

where R is the radius of the ferrite, and H is the thickness. Helszajn then uses this eccentricity value to directly calculate the demagnetization factor along the biasing axis, and from this, the other demagnetization factors:

$$\begin{gathered} N_Z = \frac{1 + e^2}{e^3}\left[e - tan^{-1}(e)\right] \\ N_x \cong N_y = \frac{1 - N_z}{2} \end{gathered} \tag{3.5}$$

For the electrically thick triangular ferrite presented in this thesis, the demagnetization factors and the relationship between the internal and external DC magnetic field using Kittel's equation in (2.8) comes out to be:

$$\begin{gathered} N_z \cong 0.84 \qquad N_x \cong N_y \cong 0.08 \\ H_{int} = 0 = H_{ext} + (N_x - N_z)4\pi M_S \\ \rightarrow \quad H_{ext} = (N_z - N_x)4\pi M_S \cong 700\ Oe \end{gathered} \tag{3.6}$$

As the below resonance circulator was designed with the bandwidth optimal internal DC field of 0 Oe, the required external field to be produced is 700 Oe. In order to produce a bias field of this strength uniformly, two magnets, one on either side of the stripline structure, are placed with the ferrites at their center. To ensure the ferrites are saturated everywhere, it is desirable that the biasing magnets have a larger radius than the ferrites to minimize the presence of fringing fields at the magnet edges that are both weaker are not aligned in $\hat{z}$.While this simple strategy in and of itself is enough to create a uniform field, there are many well-known methods [38] to increase uniformity, most notably the inclusion of a C-clamp composed of a magnetically conductive material such as iron or cold-rolled steel. When the clamp is hitched over the far faces of the magnets, the magnetic flux produced by the magnets follows the path of least resistance, or in this case, reluctance – the magnetic equivalent of resistance. The inclusion of this clamp provides a magnetic flux return path that minimizes flux leakage, thus reducing the amount of energy needed for the same magnetic field intensity between the two magnets. As such, the magnet thickness can be reduced while simultaneously creating a more uniform field. After some deliberation, MuMetal was chosen as the magnetically conductive clamp material due to its extremely high permeability allowing a minimal cross-section. 14 mil thick MuMetal was purchased from Magnetic Shield Corporation.

Due to the metal enclosure and the ferrites themselves, the minimum distance between the magnets $s = t_{line} + 2t_{GND} + 2d_{ferrite} = 4.25\ mm$. There are many types of permanent magnets to choose from, from ceramic to neodymium. As neodymium is among the strongest permanent magnets, using them in this design would result in vanishingly thin magnets. From intuition, ceramics magnets, while among the weakest permanent magnets, are still strong enough to generate the needed magnetic field without being thick enough to violate the maximum device height of 25.4 mm (0.5”). To determine the necessary magnet thickness to generate the required H_{ext}, one needs to calculate the magnetic reluctance of the magnetically conductive clamp and the magnetic reluctance of the electric circuit between the magnets. Apart from the ferrites themselves, no part of the electric circuit is magnetic ($\mu_r = 1$) so they can be treated like air. The ferrites are assumed to be magnetically saturated, such that the effective permeability $|\mu_{eff}| \cong 1$, with the Polder permeability tensor elements $|\mu| \cong 1$ and $|\kappa| < 0.3$. However, this is not the case for this particular circulator. At the center frequency of 3 GHz, $|\mu_{eff}| \cong 0.26$, $|\mu| \cong 1$ and $|\kappa| \cong 0.86$. Fortunately, the ferrites comprise the vast majority of the air gap, such that we can treat the effective permeability as the permeability of the “air” gap.

To calculate the magnet thickness and type needed, as well as clamp dimensions and permeability needed, a leakage factor F defined as the ratio between the total magnetic flux density, and the magnetic flux density needed in the ferrite region [38]:

$$F = 1 + \frac{1.7\, U_m\, L_g}{A_g} \left[\frac{L_p}{L_p + L_g} + 0.67 \frac{0.67\, L_m}{0.67\, L_m + L_g + 2\, L_p} \right] \tag{3.7}$$

where a subscript of g denotes a property of the air gap, p a property of the pole pieces if used, and m a property of the permanent magnets. U refers to the perimeter of the magnets, L refers to length/height, and A refers to the area of the air gap at any point along the gap length. It is worth noting that L_m refers to the total magnet length and not necessarily individual magnet length. If a circulator were to use a magnet on either side of a stripline circulator, such as in this thesis, then the length of each magnet would be $0.5L_m$. Such a biasing structure is depicted in Figure 3.2.

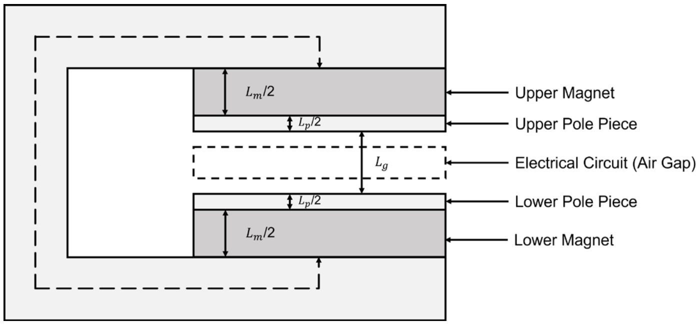

Figure 3.2: Typical biasing structure of a ferrimagnetic junction circulator.

Without a low reluctance clamp, the total magnet length and area required can be derived using:

$$L_m = \frac{B_g L_g}{H_d} \qquad A_m = \frac{B_g A_g}{B_d} \tag{3.8}$$

where, B_g refers to magnetic flux density in the gap between the magnets, which is equivalent to the applied magnetic field intensity (H_{ext}) if the gap can be treated as an air gap. A_g is the cross-sectional area of the gap, equivalent to the surface area of the normal face of the ferrites. B_d and H_d are the magnetic flux density and magnetic field intensity, respectively, of the biasing magnets, which may be read from their demagnetization curve. Magnet vendors will additionally provide a maximum energy product BH_{max} with the unit of MGO_e. The exact operating point of the magnets will depend on the magnet dimensions and their implementation, which can be simply denoted using a parameter called the permeance coefficient. This coefficient is discussed further in Section 3.5.6. Due to fringing fields in the air or ferrite gap, the length of the gap L_g is not the true length between magnets, but instead, an effective length is given by:

$$L_g = \left(R_g + R_i\right) A_g \tag{3.9}$$

where, R refers to the reluctance of a given path, with R_g being the reluctance of the air or ferrite gap, and R_i being the reluctance of the flux return path consisting of a high permeability material. Regardless, the reluctance is given by:

$$R = \frac{L}{\mu A} \tag{3.10}$$

where L refers to the length of the path, A refers to the cross-sectional area, and μ refers to the relative permeability of the path. As the flux return path is almost invariably of a very high permeability material, this results in an effective gap length only slightly larger than the true gap length.

To compensate for flux leakage, one must adjust the cross-sectional area of the magnets to provide as uniform as possible magnetic field intensity between the permanent magnets. This will require an adjustment to the radius of the magnets but not to the magnet thickness as the strength of the field between the points corresponding to the center of the magnets' faces is not changing. The new magnet area is now:

$$A_m = \frac{FH_{ext}A_g}{B_d} \tag{3.11}$$

The fruits of this labor result in ultimately smaller magnets in both thickness and radius, along with magnetic shielding protecting the rest of the circuitry from the high biasing field levels. The inclusion of a magnetic clamp dramatically reduces the magnetic field intensity outside of the region of the magnetic circuit and focuses the field between the magnets to be more uniform in both strength and direction.

A clamp consisting of an almost arbitrarily high relative permeability will serve to allow for a near-perfect magnetic return path, and therefore near-perfect magnetic shielding. MuMetal is a very useful material for this application, a mostly nickel alloy that has a relative permeability of upwards of 100,000. This high value provides a clamp with an immensely small reluctance almost regardless of thickness. As can be seen from hysteresis curves, this does not provide the full picture, as permeability is maximized in most materials for low levels of magnetic field intensity. While MuMetal has immensely high relative permeability, this value quickly diminishes when the material saturates and the magnetic flux density ceases to increase. For MuMetal, this occurs for a magnetic field intensity level of 0.1 Oe, significantly below the biasing level of this circulator. Therefore, we can consider the clamp in this situation to be saturated, resulting in a flux density of 8 kG. As we desire a biasing level of 700 Oe, we can consider the relative permeability of the clamp to be 8.7. While a thickness of 14 mils of this material is far from the ideal case of 0 reluctance, it is far better than the clampless case. A minimal clamp size was chosen for malleability reasons, and the magnets were thickened to compensate.

Before the permanent magnet solution can be finalized, the operating point of the magnets must be determined. Before iteration to more accurately determine the location on the hysteresis curve the magnets operate, an initial point can be approximated by calculating the permeance coefficient P_c. The permeance coefficient is analogous to the relative permeability of the magnet, as it describes the relationship between the magnetic flux density and the magnetic field intensity of the magnet at its operating point. For either quadrant two or four of the hysteresis curve, one can draw outwards from the origin, slope equal to -1 times the permeance coefficient. The intersection of the demagnetization curve of the magnet and the permeance coefficient line is the operating point of the magnet. While it is simple to calculate the permeance coefficient for a single disk magnet surrounded by a nonmagnetic medium, calculating the exact permeance coefficient for the magnetic biasing circuit discussed in this thesis is an exercise in futility that is more easily extracted from an Ansys Maxwell simulation.

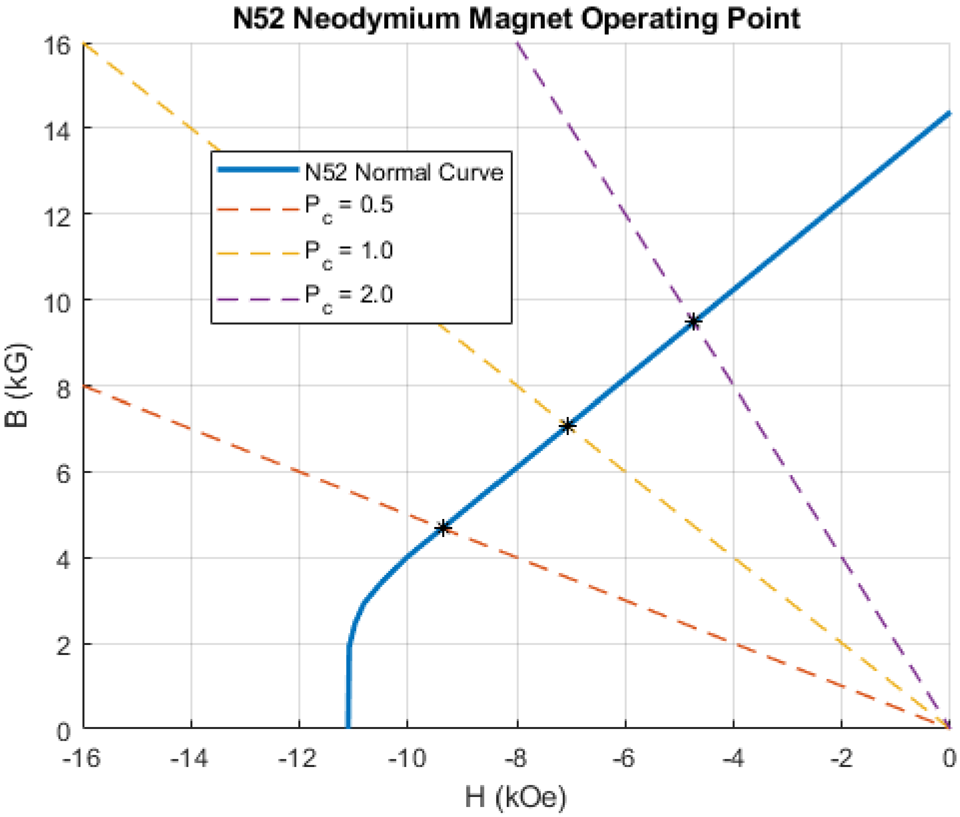

Figure 3.3: Operating point extraction example for N52 grade neodymium (from [39]) magnet for varying known permeance coefficients. Operating points (B_d, H_d) can be read from the intersection points marked with asterisks (*).

Using (3.7) – (3.11), we find that a pair of ceramic grade 1 ($BH_{max} = 1.05\ MGOe$) magnets each with a thickness of $d_{magnet} = 2.5$ mm spaced 6 mm apart using 14 mils thick MuMetal will generate a magnetic field of approximately 920 Oe, assuming a width equal to the enclosure width, 25.4 mm. Ceramic 1 magnets (CM-0279) with a radius of 0.355 inches and a thickness of 0.1 inches were procured from Magnet Kingdom [40].

3.3 Surface Mount Integration

The circulator enclosure is designed to allow a surface mountable connection within a greater circuit board. In many cases, this type of connection is preferable to a coaxial connection or direct drop-in implementation due to the simplicity of integration. A coaxially connected can easily be added to an existing design but adds a degree of complexity to the circuit footprint, making minimization difficult. Coaxially connected circulators are by far the most common type of circulators seen in COTS devices but are rarely the ideal implementation. Meanwhile, a drop-in implementation circulator requires a significant amount of alteration to an existing board and severely limits the degrees of freedom in which an engineer can design the circulator and the surrounding circuitry. Because of this, drop-in connections are virtually never seen in COTS devices and are typically custom-made for a specific board. Surface mountable circulators are a rare and emerging technology and possess almost none of the disadvantages that inherently come with more common implementation methods. Surface mountable circulators, along with other surface mountable devices, provide extreme ease of integration, with only minimal alteration required for integration.

The circulator in this thesis was designed for integration using surface mount technology, as specified in Table 3.1. This is accomplished by the inclusion of a pseudo wirebond technique, wherein openings at the ports of the grounding enclosure spaced from the upper ground plane to 0.1 mm below the signal trace would convert the stripline transmission line into an air microstrip transmission line via a 90° bending, which would be reversed upon reaching the circuit board. After this, the pseudo-wirebond would be soldered to the circuit board's signal trace, with the circulator's ground found in the enclosure would be directly soldered to the circuit board's ground. The width of the wirebond was chosen to have an impedance of 50 Ω when exiting the dielectric substrate through the opening. The spacing for the lower lip of the grounding enclosure was chosen such that the width of the wirebond would be approximately that of the 34.4 Ω transformer, but not exactly. The visual difference between the two would later serve as a fabrication reference for trace location. Ultimately, the width of the trace was selected to be 0.5 mm.

3.4 Mode Suppressing Vias

It was predicted that introducing cavity mode suppressing vias into the circulator enclosure would be required due to the electrically large footprint the circulator would require, thanks to the introduction of a large quantity of quarter-wave transformers. The complexity of the circuit makes the closed-form calculation of the lowest order cavity resonance somewhat challenging, but an approximation can be gained by calculating the resonance frequency of a 1”x1” cavity filled entirely with MCT-20. The equation for the resonance frequency of a rectangular cavity is known to be [15]:

$$f_{mnl} = \frac{c}{2\pi\sqrt{\varepsilon_r \mu_r}} \sqrt{\left(\frac{m\pi}{a}\right)^2 + \left(\frac{n\pi}{b}\right)^2 + \left(\frac{l\pi}{d}\right)^2} \tag{3.13}$$

where, m, n, and l correspond to the order of the resonance in each dimension, with a, b, and d being the length of the dimensions, respectively. The geometry of the cavity is as depicted in Figure 3.4.

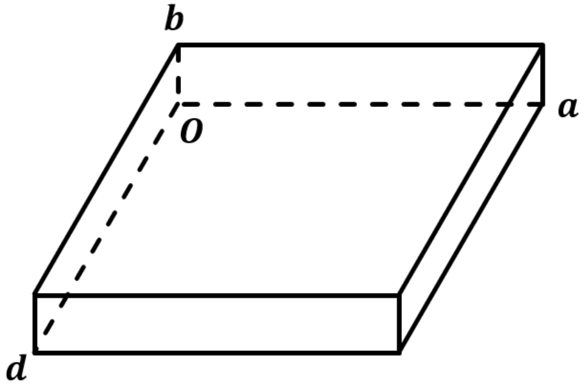

Figure 3.4: Definition of the geometry used to calculate the cavity resonance frequency as in (3.13).

As the footprint of the enclosure is significantly larger than the thickness, the lowest order cavity resonance will be f_{101}. With the approximation of the assumption that no signal trace is present and the ferrite is replaced with MCT-20, we have an initial assumption of the lowest cavity resonance at $f_{101} = 1.867\ GHz$.

A series of vias were implemented along the stripline transmission lines and around the triangular ferrite discs, with enough special separation to prevent degradation in performance. Due to the Tetris-like nature of the thick ceramic dielectric pieces, the traditional implementation of mode suppressing vias is impractical. Instead, large holes were drilled by Island Ceramics in order to incorporate steel screws to act as both mode suppressing vias and structural rigidity. Eigenmode simulations and closed-form modeling of the vias are discussed in Section 3.5.4.

While it is desirable to set the distance between mode suppressing vias to a maximum of $\lambda/20$, the extreme brittleness of the MCT-20 material forced the practical placement of the 2 mm diameter steel screws acting as vias to 3 mm from edge to edge. For MCT-20, a substrate with a relative permittivity of 20, this spacing corresponds to 0.18λ at the maximum operating frequency of 4 GHz. Due to the displacement of the ferrite junction to be closer to ports 2 and 3, this spacing only exists near port 1.

The mode suppressing vias were placed close enough to the transmission lines to prevent a cavity resonance in the passband but were additionally placed far enough away that the impedance of the transmission lines was minimally altered. This spacing was found to be 2 mm from the edge of the low impedance 16.6 Ω quarter-wave transformer, or 7.2 mm apart. An additional spacing of 2 mm away from the ferrite junction was found to minimize the impact on circulator performance, as will be discussed in the Ansys HFSS simulations in Section 3.5.2. Due to the circular symmetry of the circulator near the low impedance transformer, these vias exist on all sides of the ferrite. All the design decisions thus considered ultimately create a circulator with the geometry roughly approximated in Figure 3.5.

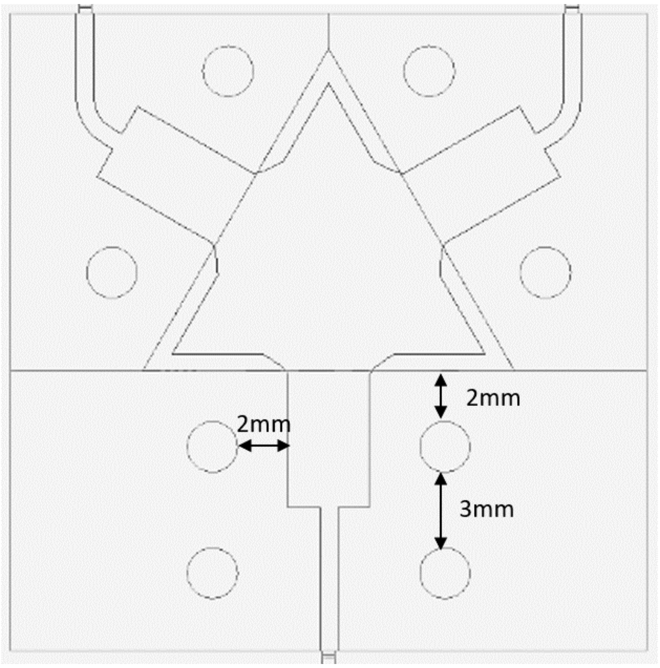

Figure 3.5: Approximation of the circulator enclosure that is to be simulated and refined.

3.5 Simulated Circulator

The below resonance ferrimagnetic circulator designed in Section 3.1 was modeled and tuned in Ansys HFSS, a popular finite element method time-harmonic electromagnetic solver. The elements of the circulator involving only DC magnetic fields were modeled and tuned in Ansys Maxwell. Due to the high complexity of circulators and the interconnectedness of individual sections, the electromagnetic simulation of the circulator was split into a series of individual simulations that were separately tuned. Only after all designs converged on their idealized values was the full circulator simulated.

As a general rule, HFSS simulations presented in this thesis have a consistent coloring scheme, as detailed in Table 3.3.

Table 3.3: Ansys HFSS Material color assignments.

Material	Color
Copper	Orange
Solder	Black
MCT-20	Green
RO 4350b	White
CVG-1201	Grey

3.5.1 Resonator Conductance Simulation

As mentioned in Section 2.1, a ferrimagnetic junction circulator can be modeled as a first-order shunt RLC resonator. Before any other simulations can be performed, the ferrite radius and conductor junction radius and shape need to be tuned such that the ferrite resonates at the designed center frequency with the desired susceptance slope, conductance, and loaded quality factor. Figure 3.7 depicts the Conductance Measurement design setup as modeled in HFSS. The center conductor in the junction is shown in a birds-eye view in Figure 3.6, allowing an intimate view of the tapering between the triangular resonator and the stripline feeding lines. This tapering provides no advantage in impedance and was used solely to prevent local maximums of H_{RF} magnetic energy through which spin-waves can be excited and power handling can be reduced, as described in Section 2.4.

Figure 3.6: Closeup of the center conductor of the junction used in all simulation models and the tapering that prevents local maximums of RF magnetic energy.

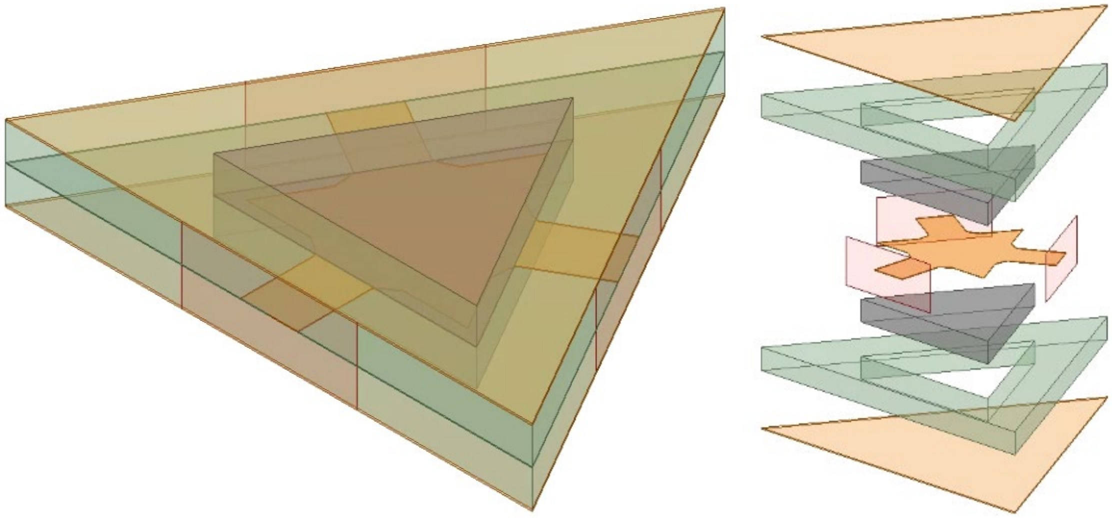

Figure 3.7: HFSS model of ferrite resonator admittance simulation, isometric view (left), and an exploded dimetric view (right).

The input admittance and quality factor of the ferrite junction were simulated and extracted from the HFSS model in Figure 3.7 for a variety of variables to demonstrate an example of the tradeoff space present in ferrimagnetic devices. To properly extract the input admittance of the junction itself with minimal impact from extraneous structures, each port of the model was de-embedded to the ferrite face. Input impedance was extracted from Port 1, with the impedance Ports 2 and 3 set to the ideal junction resistance at resonance, 11.6 Ω. The input admittance and loaded quality factor for the nominal case with all variables were set to those listed in Table 3.2 is depicted in Figure 3.8.

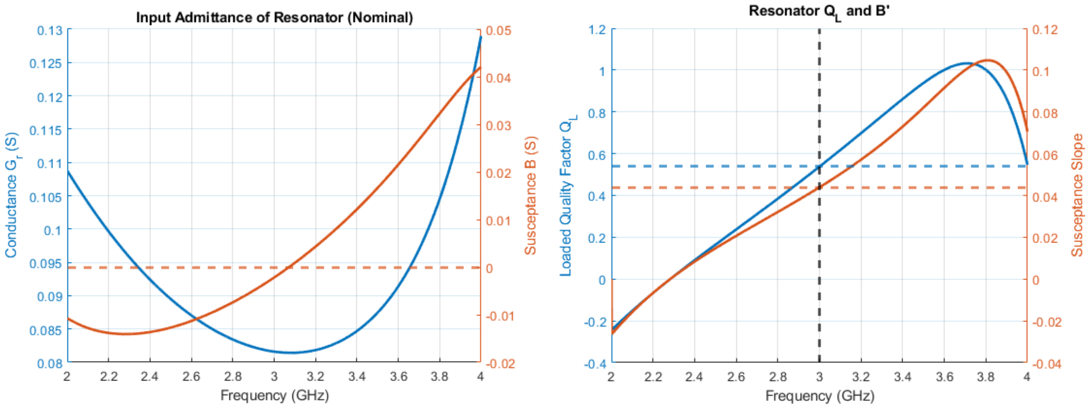

Figure 3.8: Nominal input admittance of the ferrite resonator (left) and the loaded quality factor and susceptance slope of the resonator (right) in the passband.

The conductance measurement simulation model was varied across several parameters to gain a more thorough understanding of the tradeoff space of this design, which will additionally be helpful for the novice ferrimagnetics engineer. For Figure 3.9 – Figure 3.13, the key values extracted are the resonant frequency (where susceptance crosses 0 Ω), the input admittance (conductance and slope of susceptance), and the loaded quality factor. For all of the parameter sweeps, the radius of the ferrite was be swept as well, in 0.5 mm increments from 7 mm to 10 mm. It is important to note that in the conductance measurement model, the radius of the center conductor was defined as a percentage of the radius of the ferrite, with a nominal value of 84%. This value will only change where explicitly stated. It is additionally important to note that each line plotted has what seems arbitrary beginning and ending points. For all cases in Figure 3.9 – Figure 3.13, a point is only included if resonance is found in the passband of 2 GHz to 4 GHz. If resonance occurs outside of this range, or if susceptance never truly crosses over the 0 Ω threshold, the relevant point was ignored. For all figures, a vertical line was included for the nominal ferrite radius and a horizontal line for the ideal values, as calculated in Section 3.1.

A trend seen in each figure regardless of the secondary sweeping variable was a decrease in resonant frequency as radius increases, a logical trend due to the inverse relationship between the size of a resonator and the frequency of its lowest resonant mode. Additionally, the input conductance at the resonant frequency increases with the ferrite radius (and thus conductor radius), and the additional cross-sectional area of the junction acts as a shunt resistor in the RLC model of a ferrite junction, lowering resistance and thus increasing conductance. The slope of the input susceptance decreases with ferrite thickness, quickly saturating for ferrite thicknesses above 2.0 mm. The loaded quality factor of the ferrite junction resonator additionally decreases with ferrite thickness, saturating for values over 2.0 mm. From this, it can be determined that one will not get additional bandwidth by increasing the ferrite thickness over 2.0 mm, and will only serve in achieving a lower input conductance.

The first variable swept was ferrite thickness, in 0.4 mm increments from 1.2 mm to 2.8 mm. For any given ferrite radius value, the resonant frequency decreases as the ferrite thickness increases, as an increase in thickness corresponds to an increased effective radius, as per (2.26). The impact of ferrite thickness on the effective radius quickly saturates for values greater than 2 mm. Input conductance predictably decreases as ferrite thickness increases, as the resistive part of the RLC model of the ferrite junction has a smaller value due to reduced distance between the center conductor and either ground plane.

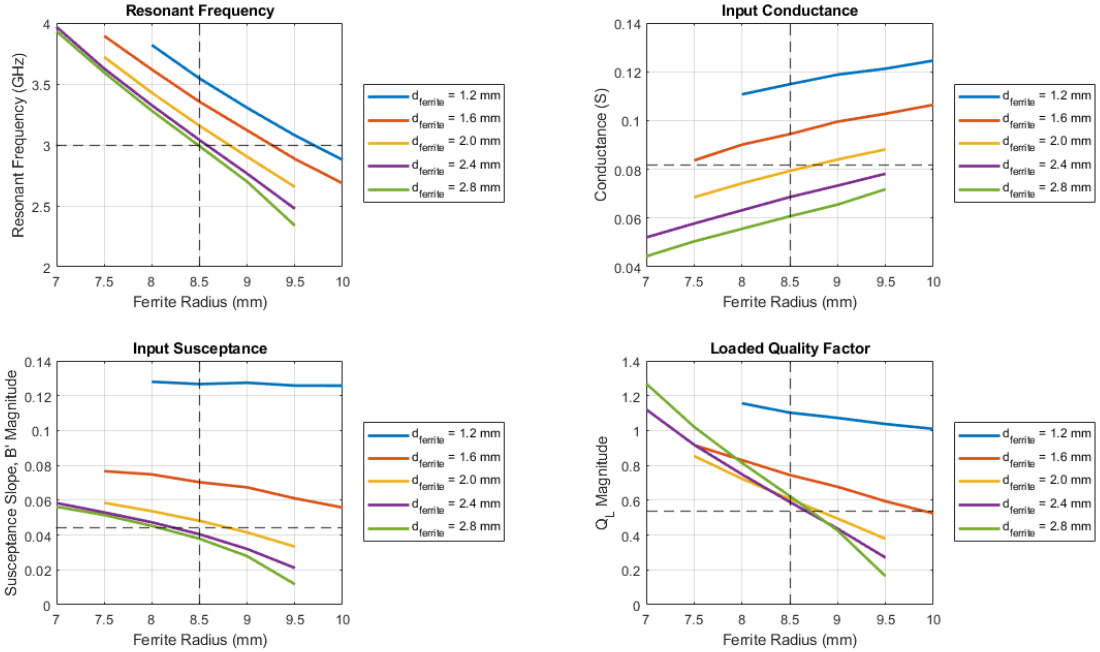

Figure 3.9: Ferrite resonator resonant frequency, input admittance, and loaded quality factor as a function of ferrite radius and ferrite thickness. The stripline input line width, the ferrite saturation and biasing, and the center conductor radius were all kept at nominal as described in Table 3.2.

The radius of the center conductor was varied, defined as a ratio of the ferrite radius and the true center conductor radius, R_f/R_c, in increments of 0.1 from 0.7 to 0.9, with an additional point at 0.99, as a center conductor radius equal to the ferrite radius causes issues with the model due to the tapering between the stripline feeding lines and the center conductor. Simulations that resulted in a resonant frequency in the passband of 2 GHz to 4 GHz have their resonant frequency, input admittance, and loaded quality factor depicted in Figure 3.10. As expected for a resonator, the resonant frequency decreases as the center conductor radius increases, in addition to the radius of the ferrite. The input admittance of the junction is seen to be incredibly sensitive to the center conductor radius, with the loaded quality factor seen to decrease as the center conductor radius increases. As the quality factor of a shunt resonator is inversely proportional to the resonant frequency, this passes a basic sanity check and allows one to choose a ferrite thickness of 2 mm for a ferrite radius of 8.5 mm to provide the idealized performance.

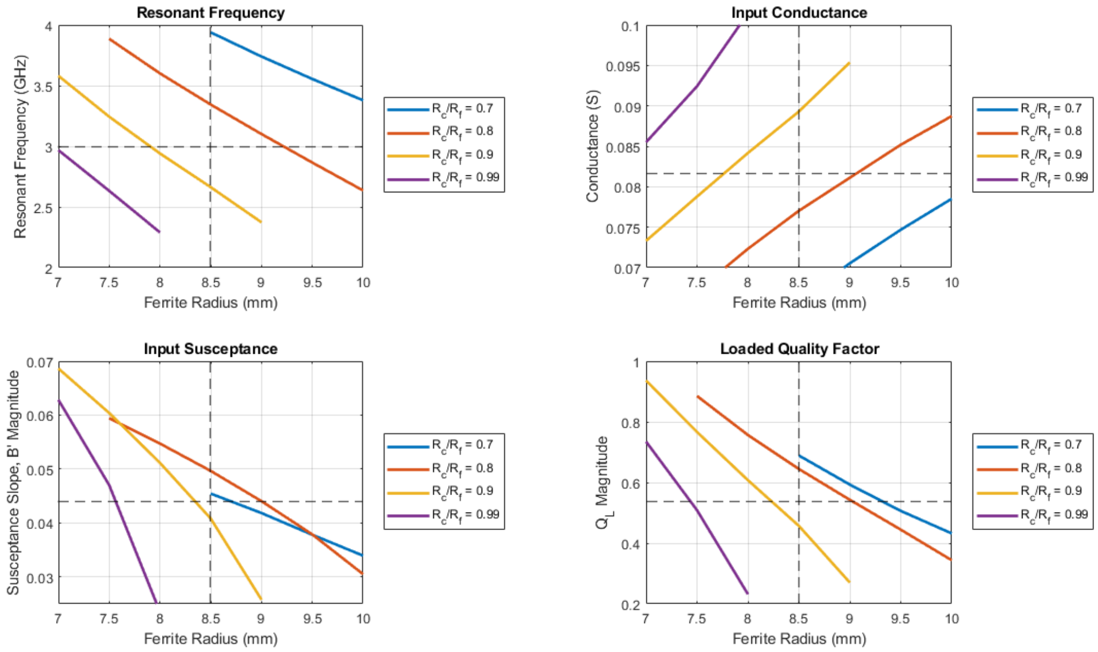

Figure 3.10: Ferrite resonator resonant frequency, input admittance, and loaded quality factor as a function of ferrite radius R_f and center conductor radius R_c, as a ratio. The stripline input line width, the ferrite saturation and biasing, and the ferrite thickness were all kept at nominal as described in Table 3.2.

The width of the center conductor was varied in increments of 0.8 mm from 1.6 mm to 5.2 mm. For this sweep, the physical dimensions of the taper were kept consistent, as the model for the taper is defined to have a static width and a length equal to half the difference between the ferrite radius and the center conductor, such that the tapering extends to the edge of the ferrite. Therefore, only the distance between the triangular tapers changed with the stripline feeding line sweep. The resonant frequency and the input conductance of the ferrite junction are found to be nearly independent on the width of the stripline feeding lines, and therefore nearly independent on the coupling angle ψ. However, the susceptance slope and loaded quality factor do vary somewhat for overly low values. As the width of the transformers feeding into the ferrite junction would be 3.2 mm wide for a ferrite thickness of 2 mm and a surrounding dielectric constant of 20, the nominal coupling angle of $\psi = 0.36$ is chosen.

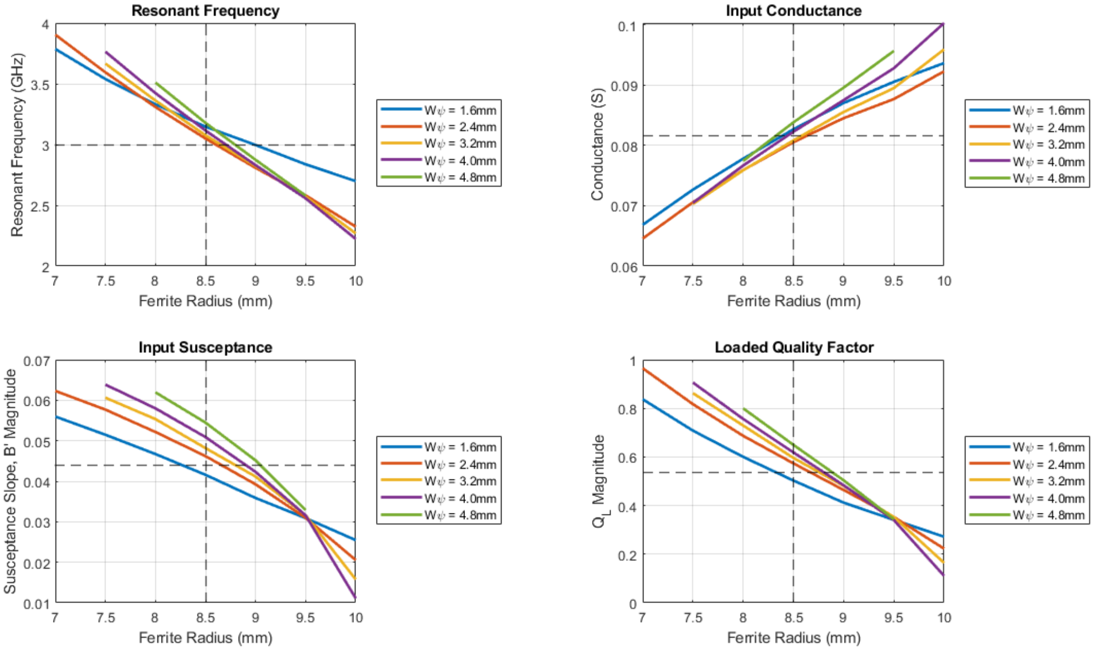

Figure 3.11: Ferrite resonator resonant frequency, input admittance, and loaded quality factor as a function of ferrite radius and stripline input line width. The ferrite saturation and biasing, the ferrite thickness, and the center conductor radius were all kept at nominal as described in Table 3.2.

The magnetic saturation of the ferrite was varied in increments of 200 G, from 500 G to 1300 G. The biasing internal to the ferrite was kept constant at 0 Oe by increasing the applied bias field accordingly. An increase in magnetic saturation is shown to result in an overall lower resonant frequency, along with an increase in input conductance and a decrease in input susceptance slope. As stated previously in Section 2.1, an increase in a ferrite's magnetic saturation will lead to an overall higher bandwidth, all else being equal. This can be seen in the loaded quality factor Q_L, which is inversely proportional to bandwidth.

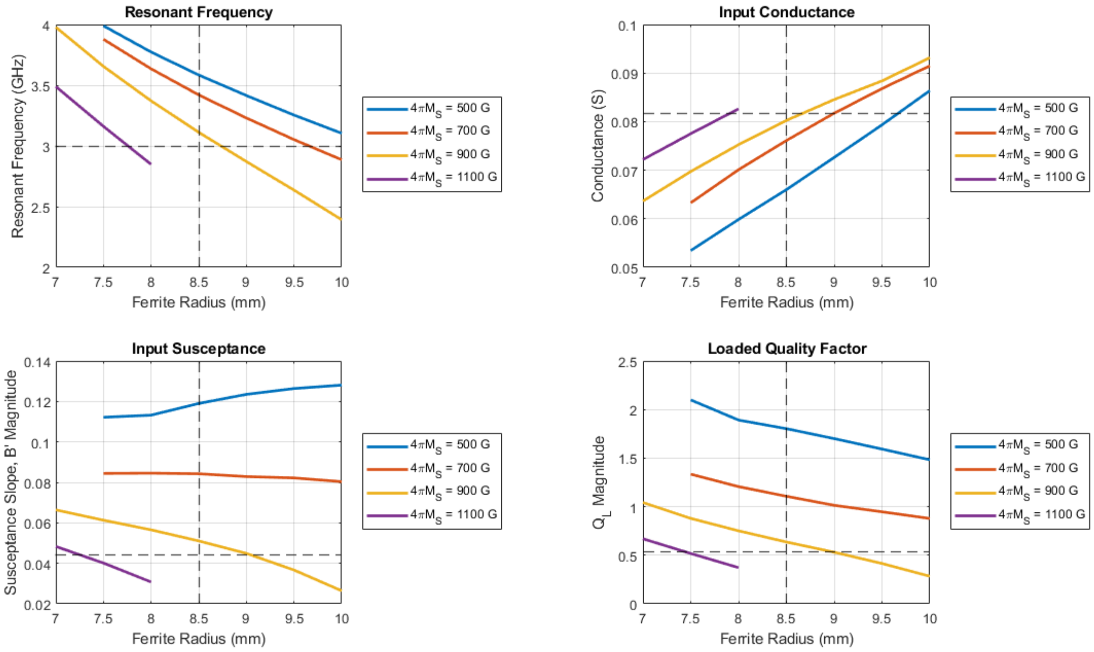

Figure 3.12: Ferrite resonator resonant frequency, input admittance, and loaded quality factor as a function of ferrite radius and ferrite saturation. The ferrite biasing, the ferrite thickness and the center conductor radius were all kept at nominal as described in Table 3.2.

The relative permittivity of the dielectric substrate surrounding the ferrite junction was varied in increments of 5, from 5 to 25. All physical dimensions were kept constant. The relationship between this variable and the performance of the ferrite junction was found to be simple and predictable, as the surrounding dielectric has minimal interaction, with only fringing fields outside of the junction and the impedance of the stripline feeding lines providing any difference in performance. An increase to the dielectric substrate relative permittivity is found to decrease the resonant frequency for any given value of ferrite radius, as well as increasing the input conductance and slope of susceptance at said frequency. The relative permittivity is found to have minimal impact on the loaded quality factor of the resonator.

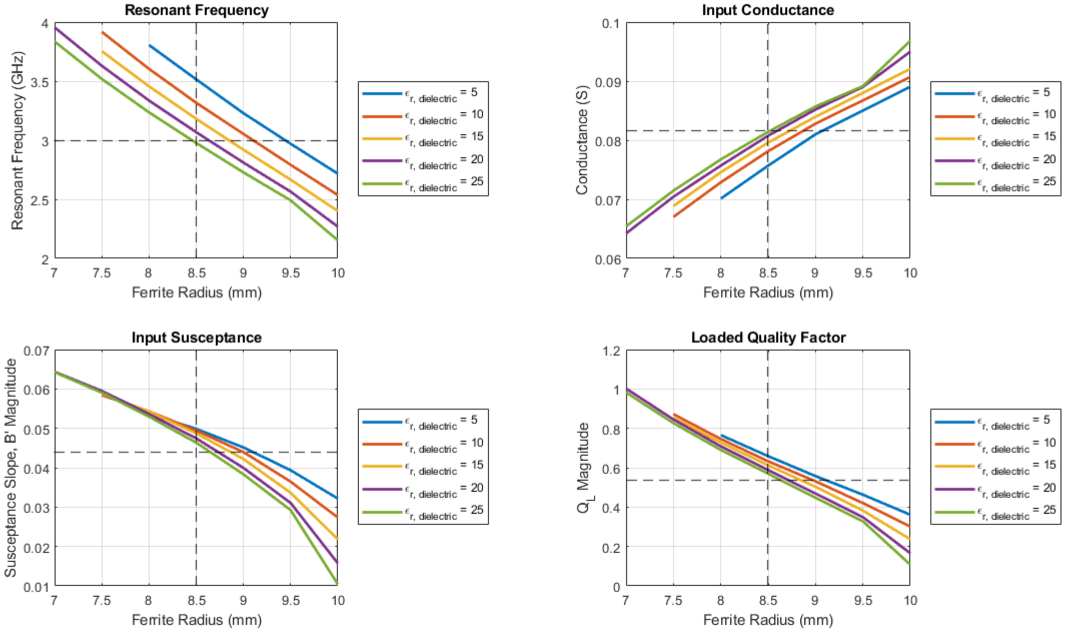

Figure 3.13: Ferrite resonator resonant frequency, input admittance, and loaded quality factor as a function of ferrite radius and substrate dielectric constant. The ferrite saturation and biasing, the ferrite thickness, and the center conductor radius were all kept at nominal as described in Table 3.2.

From (2.15) – (2.22) and Figure 3.9 – Figure 3.13, the ferrite junction physical and electromagnetic properties that provided the idealized resonator characteristics are depicted in Table 3.4. These values are used in the rest of this section in all further simulations.

Table 3.4: Ferrite Junction Characteristics

Parameter	Value
R_f	8.5 mm
R_c	7.14 mm (0.84 R_f)
d	2 mm
$4\pi M_S$	920 G
ε_r	20
L_{QWT}	5.4 mm
W_{QWT1}	0.7 mm
W_{QWT2}	3.2 mm

3.5.2 Simplified Circulator Simulation

With the physical dimensions and the electromagnetic properties of the ferrite tuned, the next step of the simulation process is to incorporate and tune the quarter-wave transformers. At first glance, this seems a simple task, but in reality is the bulk of the tuning process, thanks to the fact that the absolute width of the transmission line coming into the ferrite junction is as important a parameter as the impedance of the line itself. At the idealized ferrite thickness $d = 2mm$, coupling angle $\psi = 0.36$, and surrounding substrate dielectric constant $\varepsilon_r = 20$, the stripline transmission line width becomes vanishingly small, such that the fringing field contributions to the line's characteristic impedance become substantial in comparison to the capacitance between the ground planes and the center conductor. At this width to ground plane spacing ratio, most closed-form models of stripline impedance fall apart, and the true width of the lines needed must be extracted via a FEM EM solver such as Ansys HFSS. As such, separate Driven Modal simulations were created to calculate the impedance of the lines, as can be seen in Figure 3.14. These simulations were used to find the correct width at which the impedance of the transmission lines matched that of the ideal seen in Table 3.2.

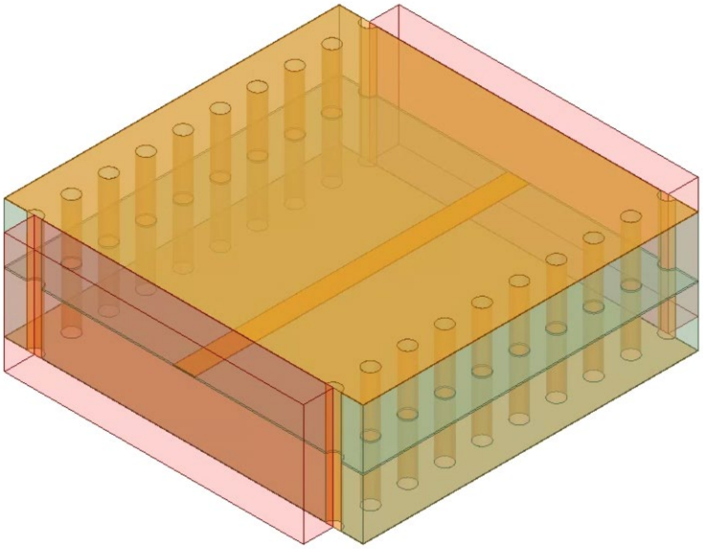

Figure 3.14: Stripline impedance simulation model. Mode suppressing vias are placed λ/20 apart for 4 GHz, the highest frequency in the circulator passband.

Once the widths for the idealized Z_{QWT1} and Z_{QWT2} were known, they were implemented in the simplified simulation model. From this point, one tunes the width and thus impedance of the lines as necessary to achieve the desired broadband performance. If no broadband solution can be found, one must go back to (2.15) – (2.22) and find another solution set to attempt. For the device presented in this thesis, it was found that the nominal width for the quarter-wave transformers was 0.7 mm and 3.2 mm, respectively. These values are used as the nominal case for the remainder of this thesis.

With the dimensions and electromagnetic properties of the ferrite junction known, the transformers were incorporated into the design in a simplified hexagonal model, as depicted in Figure 3.15. It was found that the inclusion of an airgap in the model had minimal impact on performance.

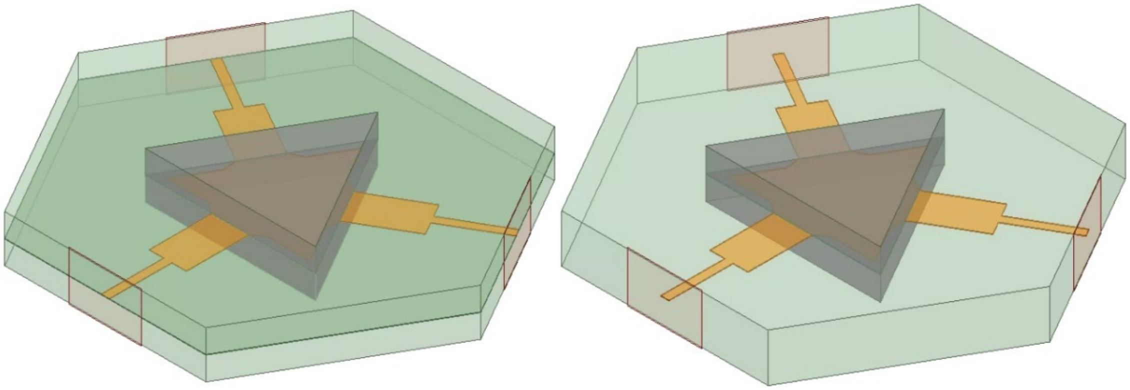

Figure 3.15: HFSS simplified model for circulator performance, hexagonal model, with (left) and without (right) an airgap for the signal trace.

The aforementioned Driven Modal simulation models were simulated to obtain the circulator's performance as measured by scattering parameters. Due to the circular symmetry of this model, and circulators in general, only three scattering parameters need to be analyzed: S_{11} in order to determine return loss, S_{21} in order to determine insertion loss, and S_{31} in order to determine isolation. The scattering parameter performance for the models in Figure 3.15 is depicted in Figure 3.16.

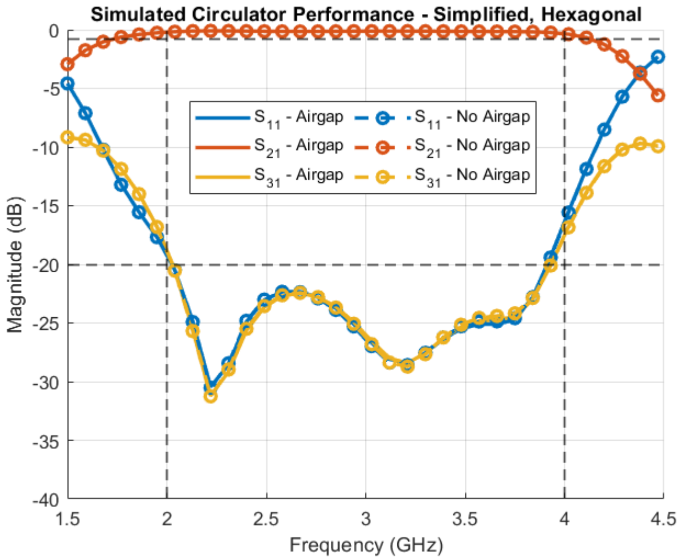

Figure 3.16: Simulated performance of the simplified hexagonal circulator model at the operational temperature of 100°C, with and without airgaps included in the model. Performance was found to not differ significantly between models.

The group delay of the simplified hexagonal simulation models was derived by taking the derivative of the phase of S_{21} with respect to frequency, and are depicted in Figure 3.17.

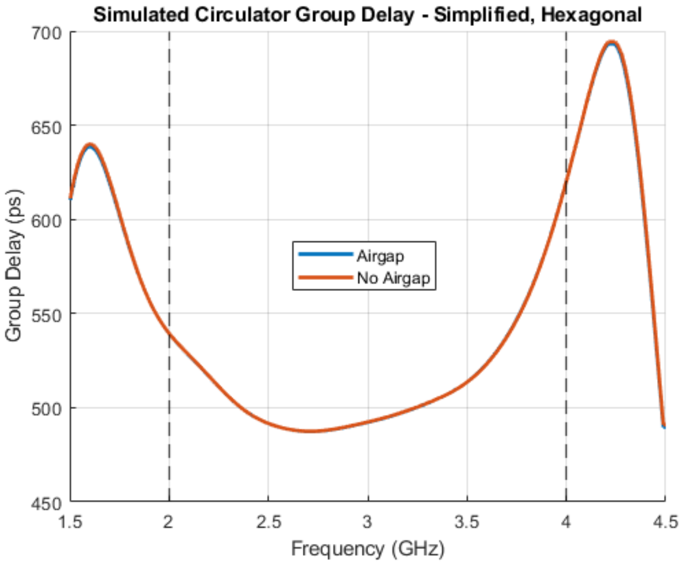

Figure 3.17: Simulated group delay of the simplified hexagonal circulator model at the operational temperature of 100°C, with and without airgaps included in the model. Performance was found to not differ significantly between models.

Once the simplified hexagonal model was solved for broadband performance, the traces leading to ports 2 and 3 were bent to make the model rectangular in order to best fit into a 1”x1” space. The low impedance traces connecting to the ferrite junction were left alone, while the higher impedance traces were bent, following a circular arc of a high enough radius to prevent significant changes in performance. While the rule of thumb in the arc is to define the radius as being at least four times the width of the line in question, it was found for this device a radius of 2.5 times the trade width allowed for a minimal impact on performance. The various simplified models with a rectangular configuration are depicted in Figure 3.18.

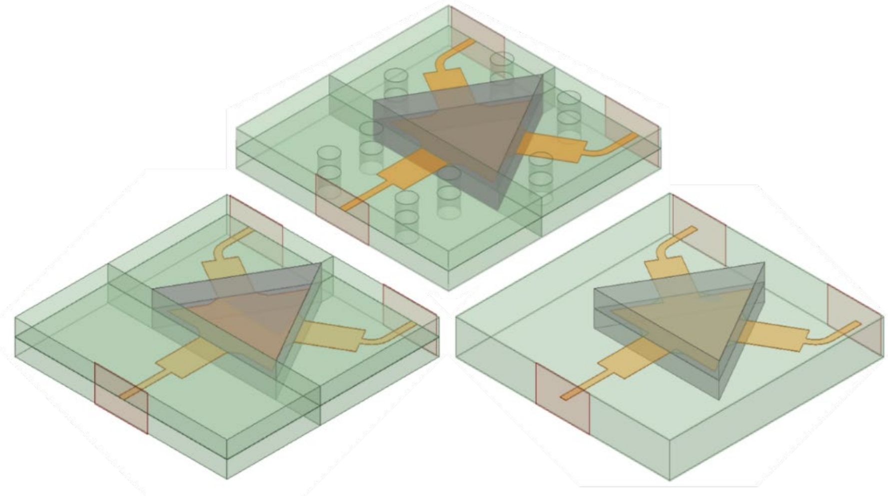

Figure 3.18: HFSS simplified models for circulator performance, with curved traces near ports two and three to simplify integration and minimize size. Pictured are the basic simulation model (right), the model with airgaps between components (left), and the model with mode suppressing vias and airgaps between components (top).

The simplified rectangular models were built in Ansys HFSS as Driven Modal simulations. As with all other Driven Modal simulations in this thesis, first-order basis functions were used with analytical solution frequencies set at 2 GHz, 3 GHz, and 4 GHz. At least 10 passes (15 in more complex simulations later on) were simulated, with at least 5 passes (7 in more complex simulations) with less than 0.01 ΔS required for convergence. The scattering parameter performance of all three simulation models is depicted in Figure 3.19. The difference in performance when including the mode suppressing vias was found to be minimal, as predicted in Section 3.4. Overall, the largest contributor to changes in performance was the inclusion of an air gap. As the inclusion of the airgap layer allows the effective dielectric constant of the stripline to fall below the relative permittivity of the material that only worsens as frequency increases, one can expect the performance to differ from the nominal case with no airgap. In addition to scattering parameters, the group delay for each model was derived by taking the derivative of the phase of S_{21} with respect to frequency, and are depicted in Figure 3.20.

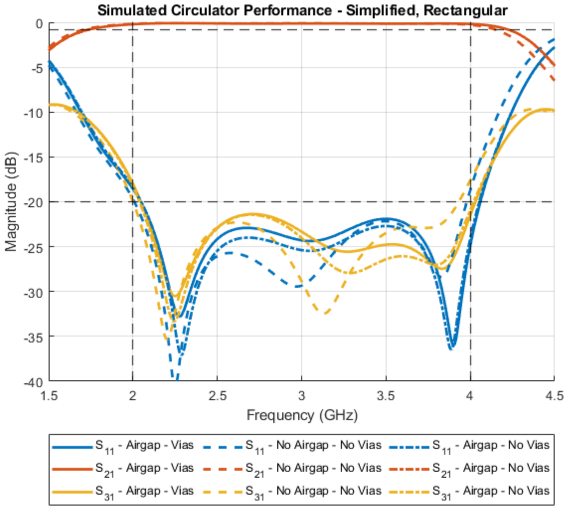

Figure 3.19: Simulated scattering parameters for the rectangular simplified simulation models depicted in Figure 3.18, at operating temperature (100°C).

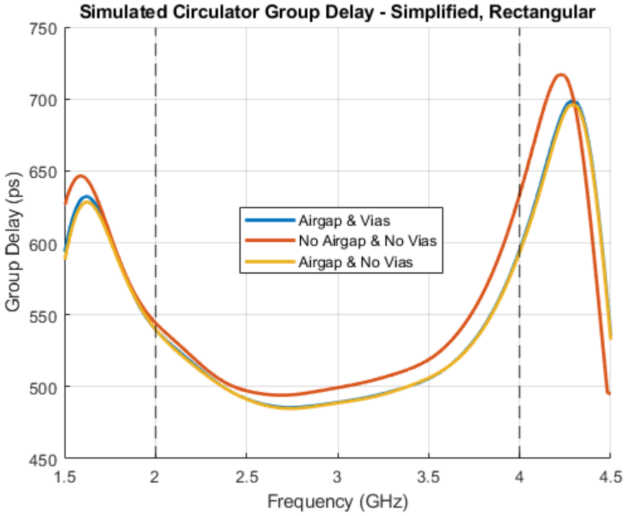

Figure 3.20: Simulated group delay for the rectangular simplified simulation models depicted in Figure 3.18, at operating temperature (100°C).

Through this tuning process, it was found that the nominal widths for the transmission lines arrive at a broadband solution for the relevant specifications presented in Table 3.2. The tuned dimensions and electromagnetic properties of the circulator are listed in Table 3.5.

Table 3.5: Optimized Circulator Design Parameters

Parameter	Optimized Value	Original Value
H_0	0 Oe	0 Oe
$4\pi M_S$	920 G	920 G
$R_{ferrite}$	8.5 mm	9.8 mm
$R_{conductor}$	7.14 mm (0.84$R_{ferrite}$)	
$d_{ferrite}$	2 mm	
$\varepsilon_{r,\ ferrite}$	14.3	
$\varepsilon_{r,\ substrate}$	20	
ZQWT1	34.4 Ω	37.8 Ω
W1	0.7 mm	
L1	2.7 mm	
ZQWT2	16.6 Ω	18.3 Ω
W2	3.2 mm	
L2	2.7 mm	

3.5.3 Surface Mount Integration Simulation

As the circulator is designed for surface mount integration, a test board was designed on which the enclosure could be placed. The testing board was designed for grounded coplanar waveguide transmission lines to make electrical connections between ground planes simple. To minimize the impact of the board on the circulator performance, the lines of the board were all at system impedance, 50 Ω. The transmission lines coming out of the enclosure were bent at 90° angles and modeled as system impedance air substrate microstrip lines. The circulator's grounding enclosure was designed around this, with openings for the trace occurring for each port. The openings were 3.41 mm wide, preventing any major change to the impedance of the trace, with a height of 2.27 mm. The opening stretches from the top ground plane to just under the stripline trace, forming a lip that acts as a microstrip ground plane during the bending transition. The substrate properties and transmission line dimensions are detailed in Table 3.4. A 2-mil layer of solder with a conductivity of 7 MS was included between the grounded coplanar waveguide to microstrip connection and between the testing board ground to metal enclosure ground, as depicted in Figure 3.23, in order to maintain realistic integration. The pseudo-wirebond microstrip lines were varied in their bending and location relative to the enclosure while in isolation to check robustness and impact on circulator performance. The limits of this performance were kept to a point such that the trace maintained a connection to the trace of the microstrip and did not contact the grounded coplanar waveguide's top ground planes.

The testing board with a simple 50 Ω through line was simulated in isolation. The length was kept consistent with the size that would exist when the enclosure would be included, at 46 mm, or 0.7λ at the center frequency of 3 GHz. The testing board is of a grounded coplanar waveguide transmission line technology, with a line width of 1 mm, and a spacing between the signal and ground copper of 0.2 mm. The substrate is Rogers RO4350B with a thickness of 30 mils.

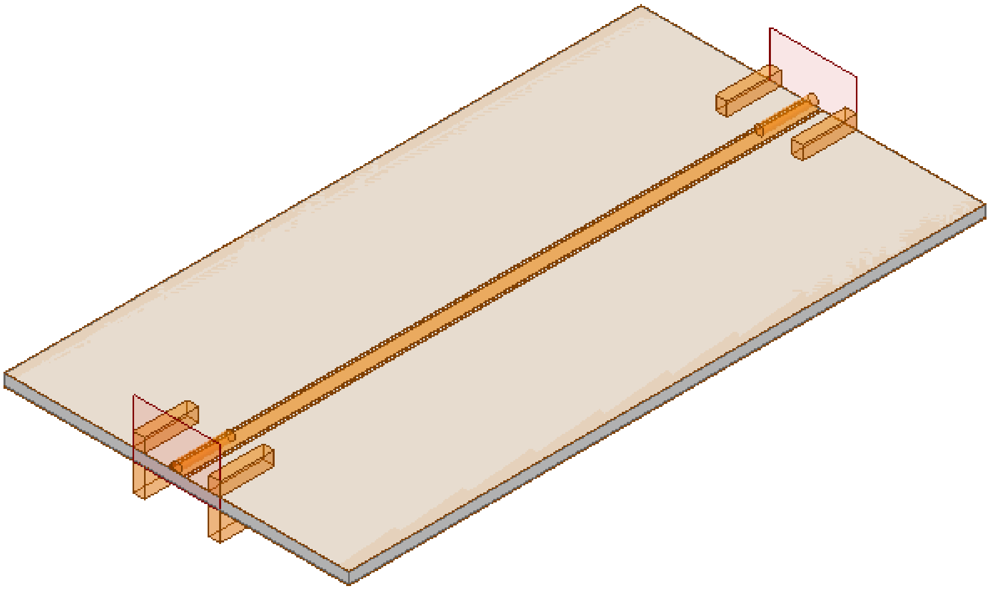

Figure 3.21: A simulation model of a 0.7λ line at the circulator center frequency, with the SMA modeled at the ports.

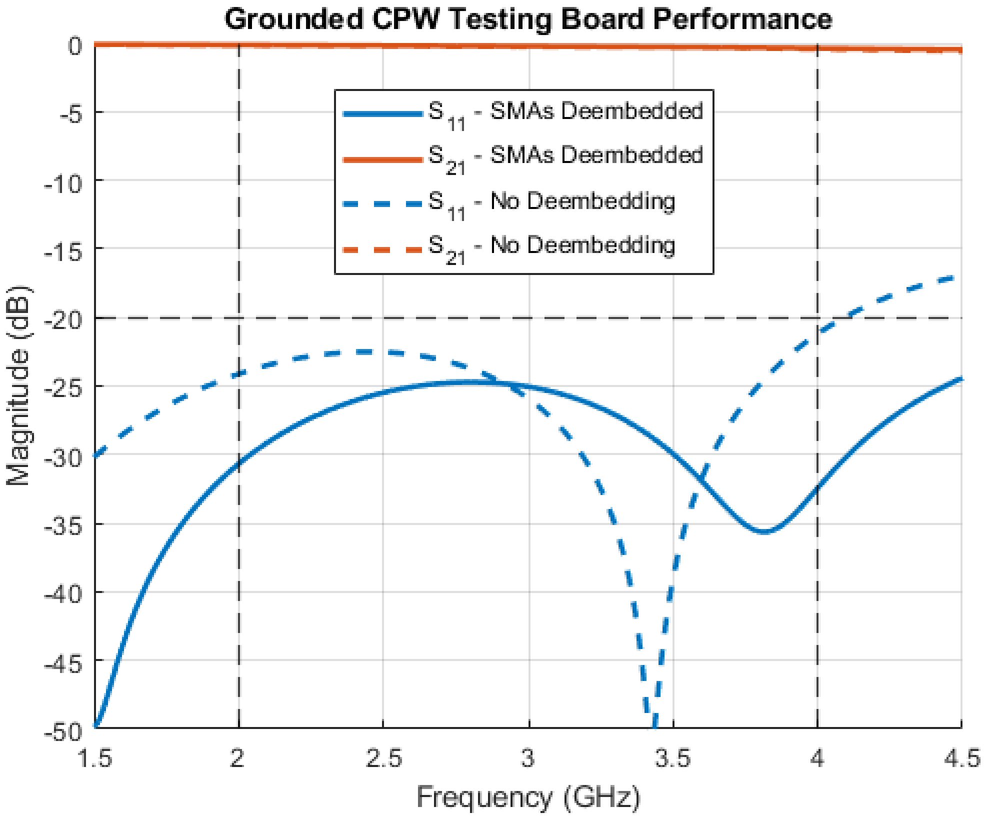

Figure 3.22: Performance of the simulation model of Figure 3.21, with and without de-embedding the SMAs out.

As displayed numerous times in previous subsections, the input impedance at any of the ports of the circulator enclosure is very close to 50 Ω, with the impedance of the lines at the ports being 34.4 Ω. All but the testing board and the enclosure were removed in creating a new simulation model to test the pseudo-wirebond surface mount integration implementation as seen in Figure 3.24, with the impedance of the microstrip line at 50 Ω, and the impedance of the stripline at 34.4 Ω. Both ports were de-embedded to the pseudo-wirebond air microstrip line. Port 1 was de-embedded to the edge of the testing board solder, pictured in grey. Port 2 was de-embedded to the boundary between the stripline's MCT-20 substrate and the air. Both ports were normalized to 50 Ω. Due to the de-embedding, the impedance of the stripline trace is inconsequential, although the width was kept at 0.7 mm to maintain realism.

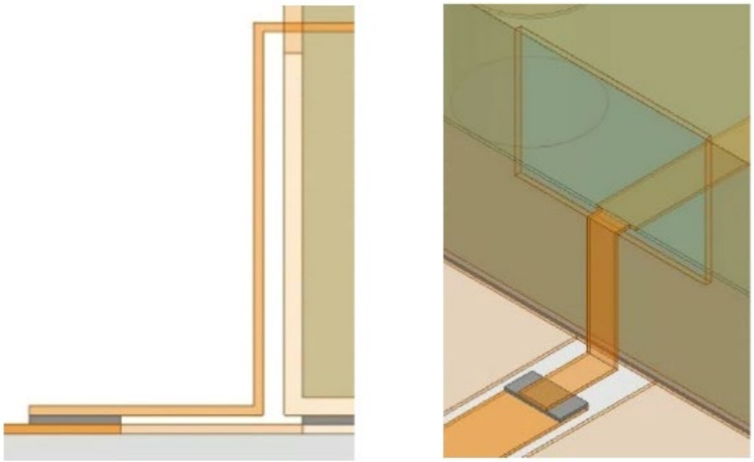

Figure 3.23: Side view and isometric view of stripline to microstrip transition as modeled in simulations. Solder (grey) is included to garner a realistic simulation performance.

The pseudo-wirebond air microstrip transmission line was varied in its location and in the degree in bending to ascertain the degree of alteration to performance an imperfect fabrication could cause. The degree of bending was varied from the nominal 90° to a minimum of 60°, in 5° increments. Additionally, the physical location of the bend was varied in $\hat{x}$ and $\hat{y}$ independently. The physical translation in $\hat{x}$ was varied from 0 mm to 1.2 mm in 0.3 mm increments, and the physical translation in $\hat{y}$ was varied from -0.4 mm to 0.4 mm in 0.2 mm increments, bringing the signal trace adjacent to the ground plane of the grounded coplanar waveguide transmission line of the testing board.

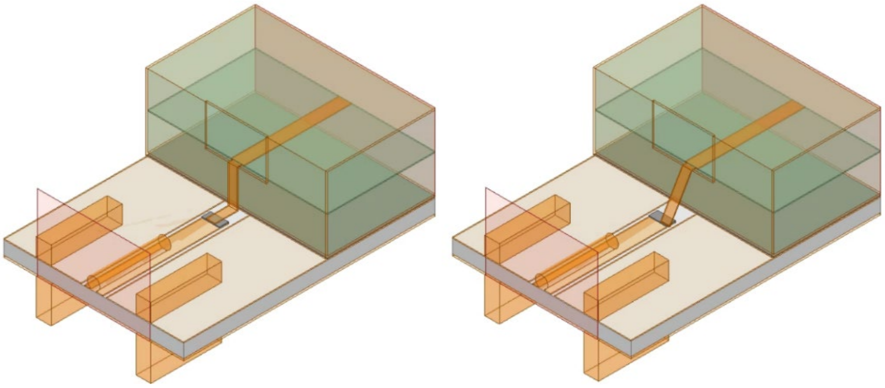

Figure 3.24: A simulation model for ascertaining the performance of the wirebond. Pictured are the models for the ideal situation of a 90° bend and no translational offset (left), and an extreme situation of a 60° bend with a 0.4 mm offset in the direction perpendicular to the signal trace.

The scattering parameter S_{11} was simulated for the pseudo-wirebond model for each of the sweeping variables independently. It was found that the return loss did not dip below 20 dB in the passband for a bending angle greater than 75°, an $\hat{x}$ translation less than 0.25 mm, and for no $\hat{y}$ translation, as can be seen in Figure 3.25.

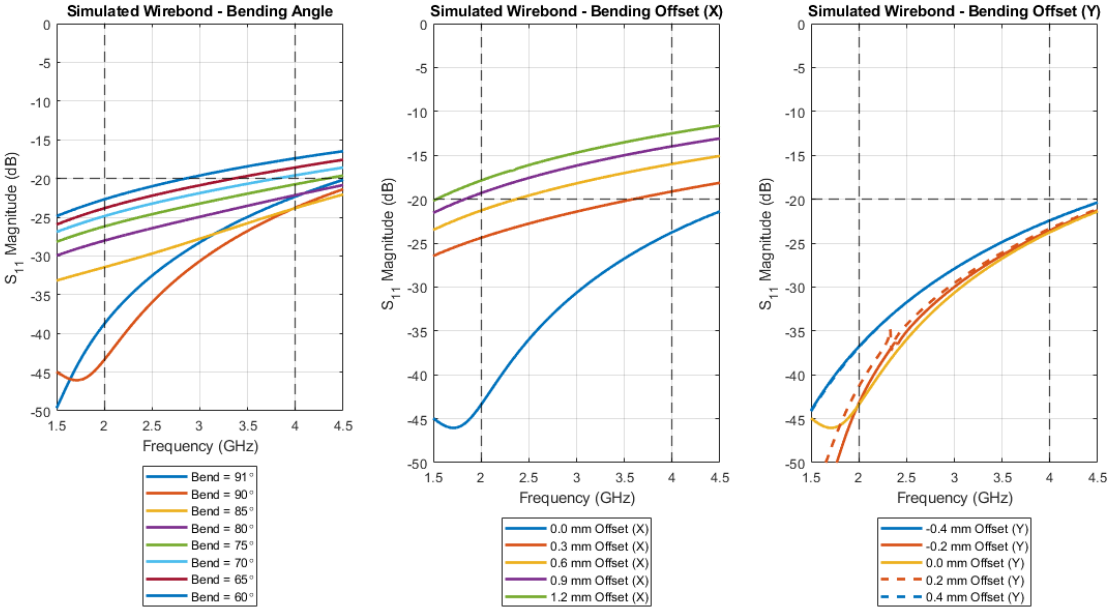

Figure 3.25: Simulation results for the model depicted in Figure 3.24, with each variable swept in isolation. Performance was seen to not degrade under 20 dB of return loss for a bending angle of under 15° under the nominal, an offset of 0.2 mm in $\hat{x}$, for no offset in $\hat{y}$ so long as no ground contact is made using the signal trace.

The circulator enclosure was added to the testing board with the ideal pseudo-wirebond transitions in simulation. All dimensions were kept as previously defined. The simulation model is depicted in Figure 3.26. The simulated results of this model, both with and without the SMAs de-embedded, are depicted in Figure 3.27. The performance is seen to only minimally changing, with the SMAs marginally reducing the bandwidth and reducing the number of reflection nulls in the passband from 3 to 2. The isolation in the passband continues to meet the specifications as stated in Table 3.1.

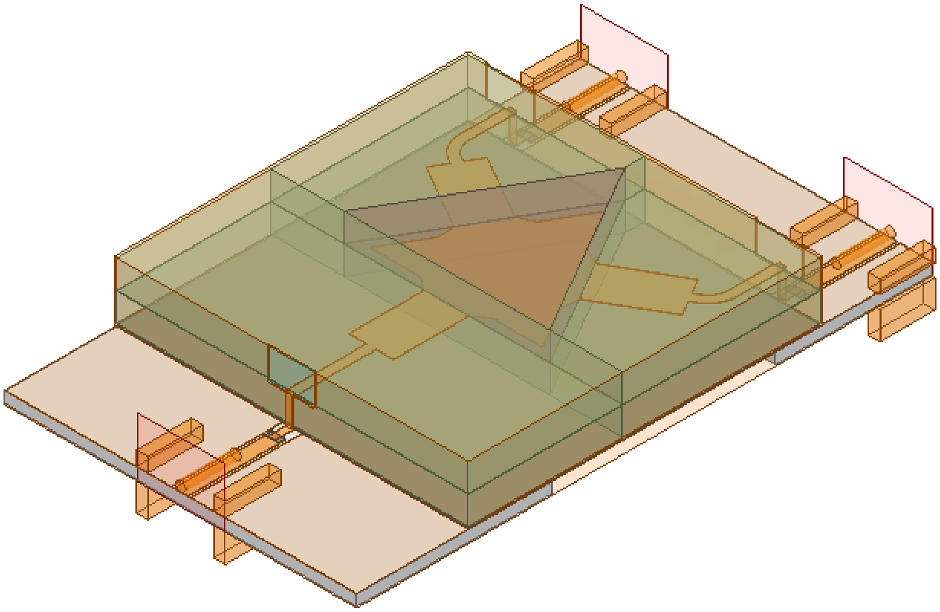

Figure 3.26: HFSS model of the full electrical circuit of the circulator, with the testing board, included.

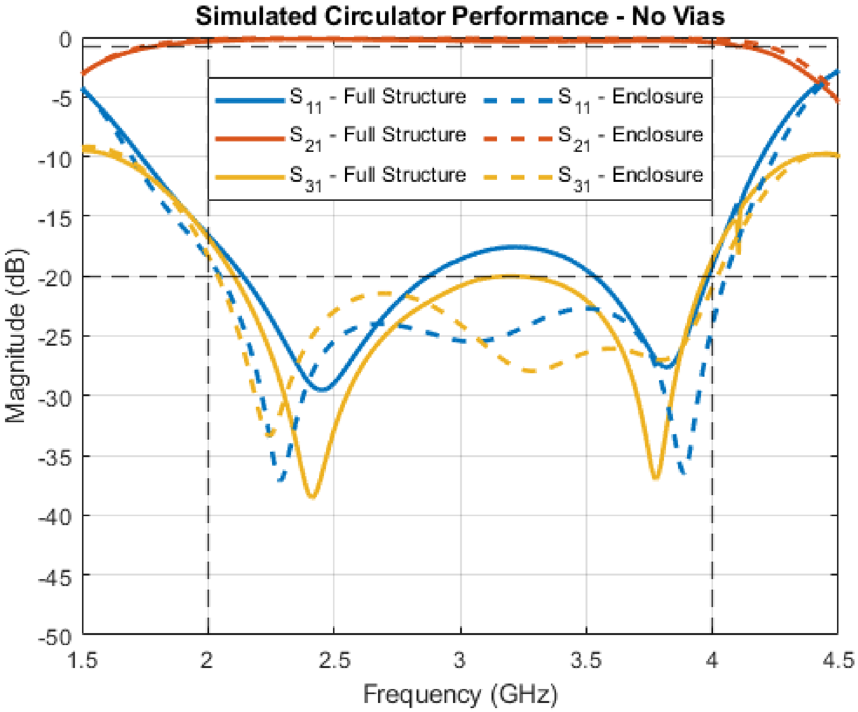

Figure 3.27: Simulation scattering parameters for the below resonance circulator with a testing board used for integration, with SMAs included. The performance of the simplified simulation described in Section 3.5.2 is included as an overlay.

3.5.4 Circulator Cavity Eigenmode Simulation

In anticipation of the cavity resonance in the circulator enclosure, an eigenmode simulation was performed in Ansys HFSS. At least as of Ansys EM 20.1, magnetic biases on ferrimagnetic materials are not supported in eigenmode simulations. Therefore, instead of a ferrite material under a magnetic bias, the ferrites were modeled using a dielectric material with a permeability equal to the Polder permeability tensor, rather than directly assigning a material magnetic saturation and magnetic bias. As the dielectric medium around the ferrites is not a continuous medium, air gaps were included that separated the pieces from each other. The minimum frequency in the eigenmode simulation was set to be well under the first cavity mode calculated in Section 3.4, at 1 GHz. The lowest order cavity resonance occurs at 1.467 GHz, using the optimized values listed in Table 3.5. This value is lower than anticipated in Section 3.4, as predicted. This is due to the air gaps and the ferrites having significantly lower dielectric constants than the MCT-20, creating an electrically smaller cavity.

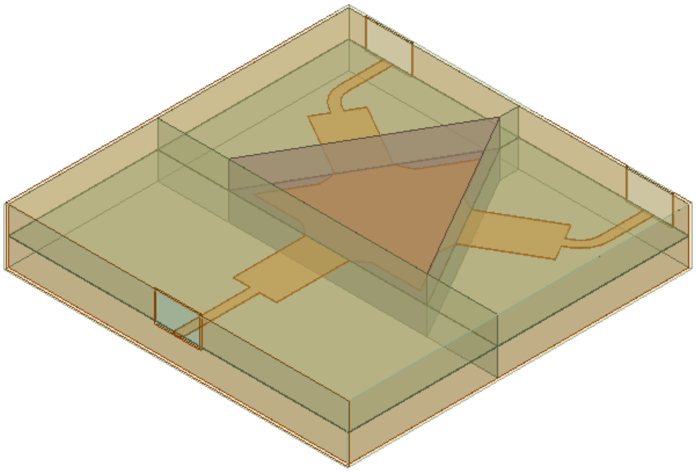

Figure 3.28: HFSS model of Eigenmode simulation for the circulator enclosure, without mode suppressing vias.

As this is well under the passband of the circulator, mode suppressing vias were introduced to bring the frequency above the passband. As steel screws were used, the material of the screws was modeled as steel with a conductivity of 1.1 MS/m and a loss tangent of 0, as is the default value used in Ansys HFSS. The steel screws were soon fused with the grounding enclosure and modeled as the same material due to minimal difference in performance. Another eigenmode simulation was run in Ansys HFSS, with the same lowest frequency as previously set. With the inclusion of the mode suppressing vias, the lowest order cavity resonance is now seen at 4.01 GHz. The first ten cavity resonance modes are depicted versus frequency in Figure 3.30.

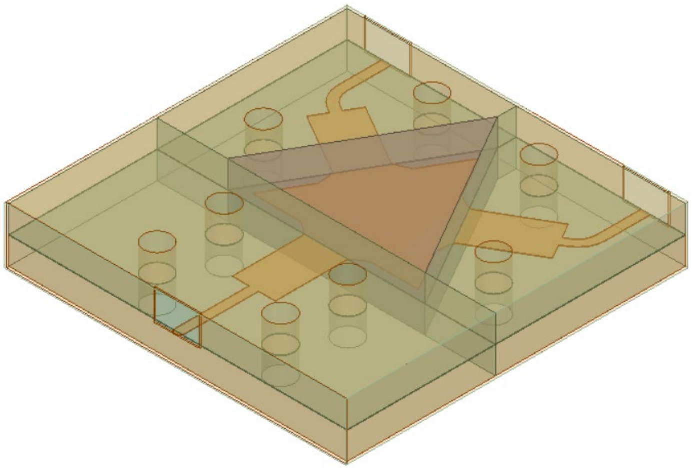

Figure 3.29: HFSS model of Eigenmode simulation for the circulator enclosure, with mode suppressing vias.

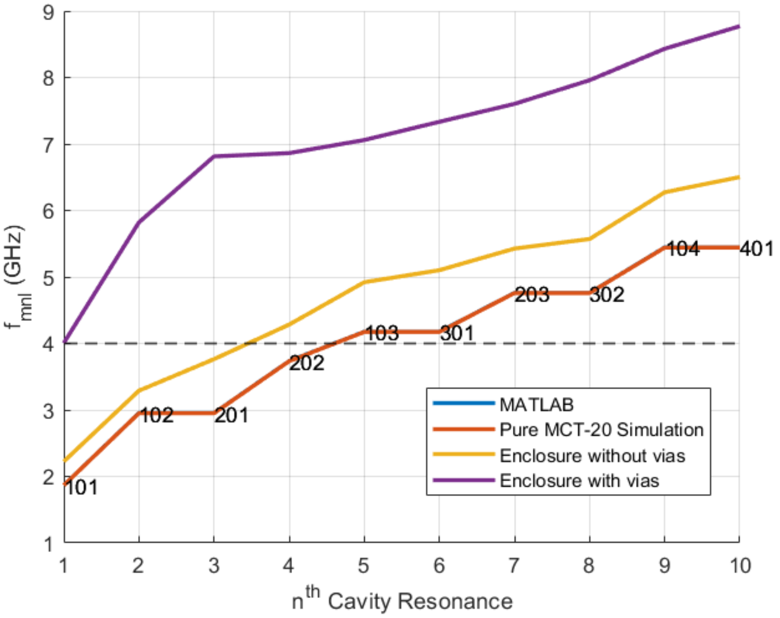

Figure 3.30: First ten cavity resonances of circulator enclosure. Depicted is the enclosure with and without mode suppressing vias, as well as the ideal case of a 25.4mm by 25.4mm by 4.05mm cavity of MCT-20. For the ideal case, the order of the resonance frequency f_{mnl} as defined in Section 3.4 is displayed at the corresponding point.

3.5.5 Simulation with Mode Suppressing Vias

The simplified simulation model described in Section 3.5 was updated to include a stripline to microstrip transition, a testing circuit board, and mode suppressing vias. Solder was placed in between all connecting points of the circulator device and the testing board, as previously discussed.

The stripline to microstrip transition is as described in Section 3.5.3, and the mode suppressing vias are spaced as in Section 3.5.4. SMAs were included in the simulation model to gain a realistic expectation of performance for testing purposes.

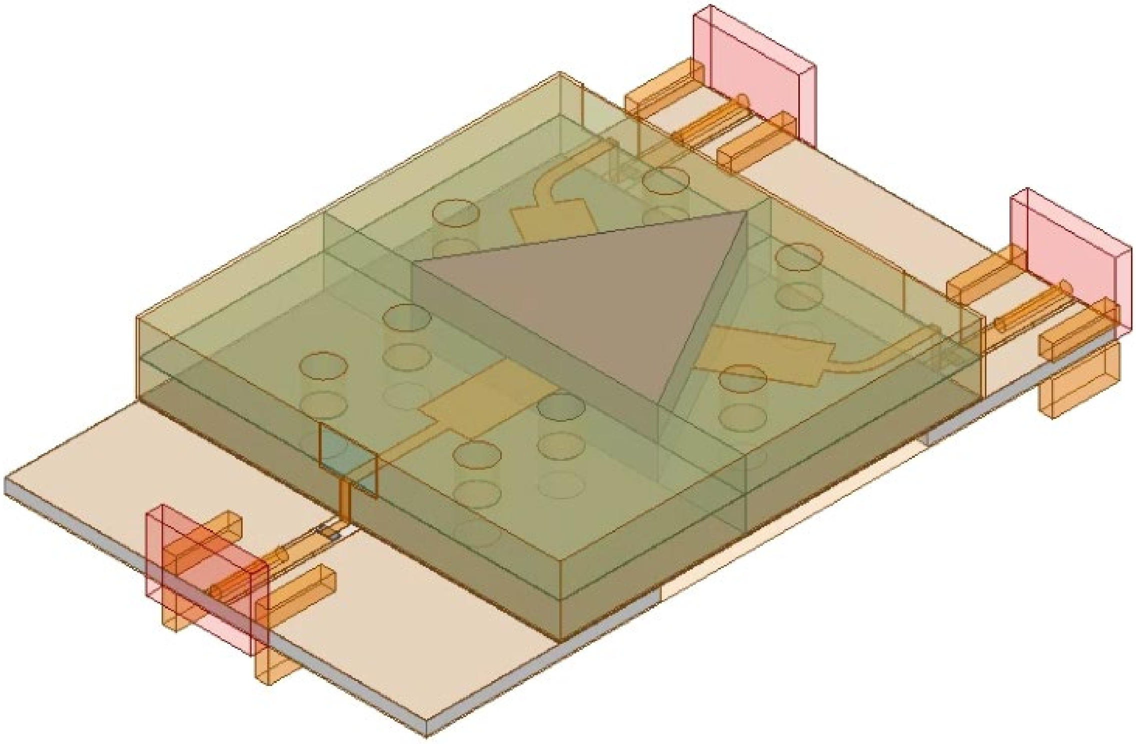

Figure 3.31: HFSS model of the full electrical circuit of the circulator, with the testing board, mode suppressing vias, and SMA connectors.

The simulated results of this model, both with and without the SMAs de-embedded, are depicted in Figure 3.32. The vias are found to only marginally reduce the return loss and isolation in the passband while retaining the general shape. The impact of the SMAs is identical to that found in Section 3.5.3.

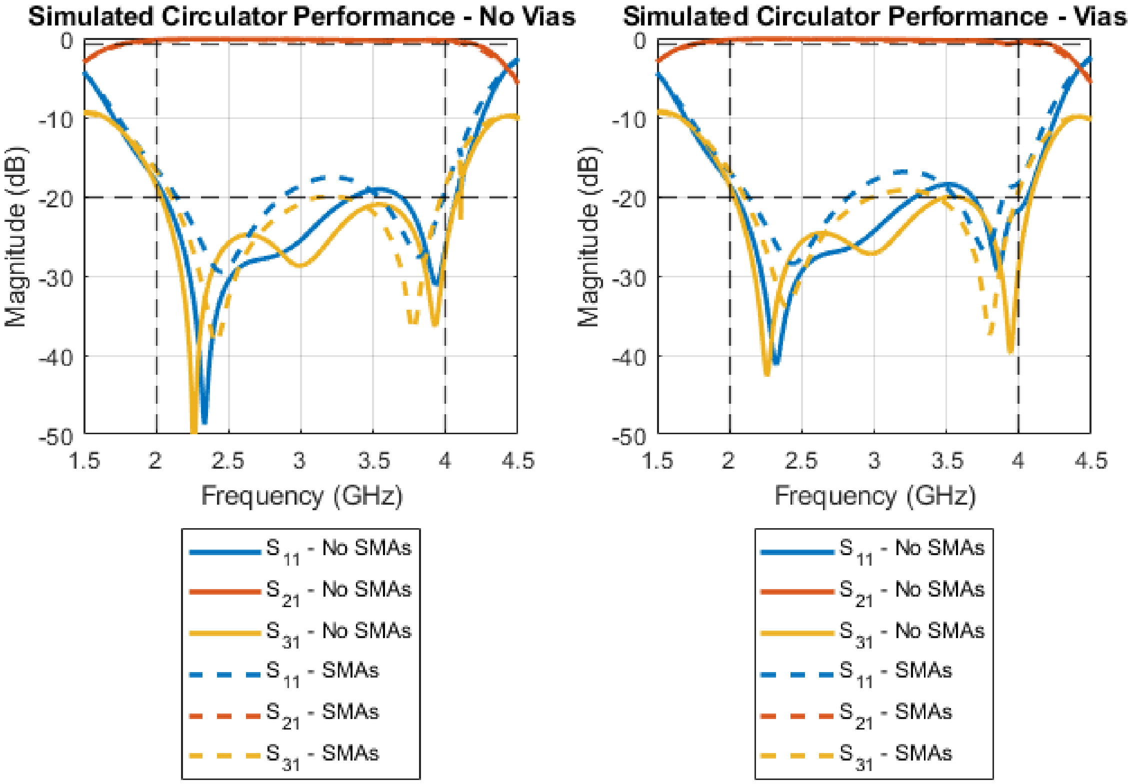

Figure 3.32: Scattering parameters of the full simulated circulator device.

3.5.6 Nonuniform Magnet Biasing Simulation

In order for a circulator to function, the ferrites must be biased to saturation. For testing purposes, this can be accomplished using electromagnets, but for a more permanent solution, permanent magnets must be utilized, self-biased circulators being the exception. Using (2.8), it is seen that the required biasing for this circulator is 700 Oe. In Section 3.2, it was found that a pair of 0.1 inches thick Grade 1 Ceramic ($BH_{max} = 1.05\ MGOe$) magnets 6 mm apart with a MuMetal c-clamp with a thickness of 14 will result in a magnetic field strength of 920 Oe between the magnets, assuming an air gap. Ansys Maxwell was then used to confirm the dimensions of the magnets would result in the required field strength.

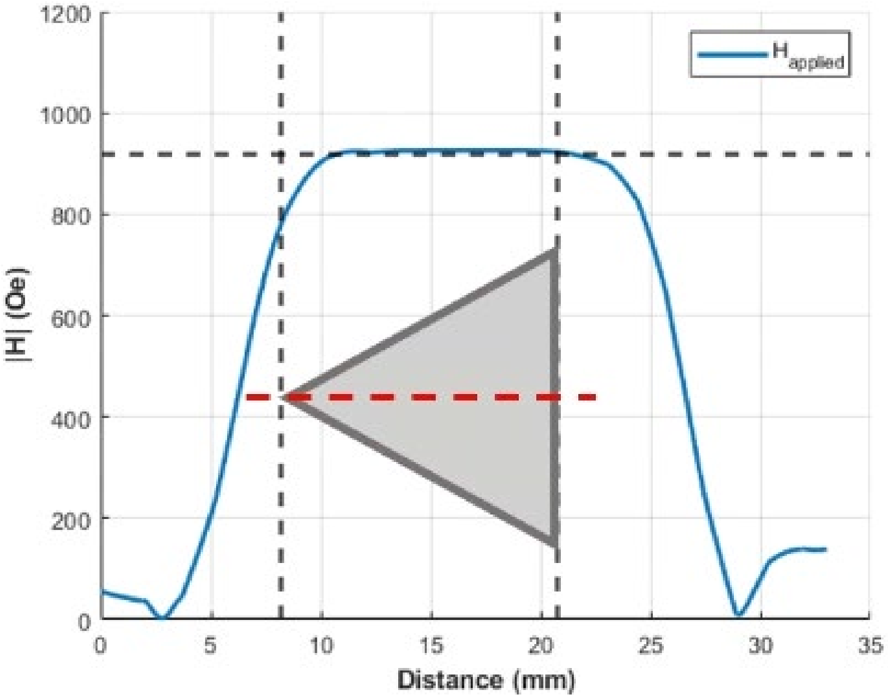

Figure 3.33: Applied magnetic field intensity strength in the enclosure region in the X-Y plane between the ferrites.

It was desirable to find stock magnets from vendors to minimize costs. Ultimately, CM-0279 magnets were purchased from Magnet Kingdom [40]. The magnetic field generated by these magnets over the volume is plotted in Figure 3.35 (Generated using the model in Figure 3.34), with the magnitude of the applied field in the gap between the ferrites plotted in Figure 3.33. Ansys HFSS and Ansys Maxwell are capable of linking simulation data in order to bias ferrimagnetic material nonuniformly. This feature was then used to bias the ferrites non-uniformly in the "Simulation With Vias" driven model simulation described in Section 3.5.5.

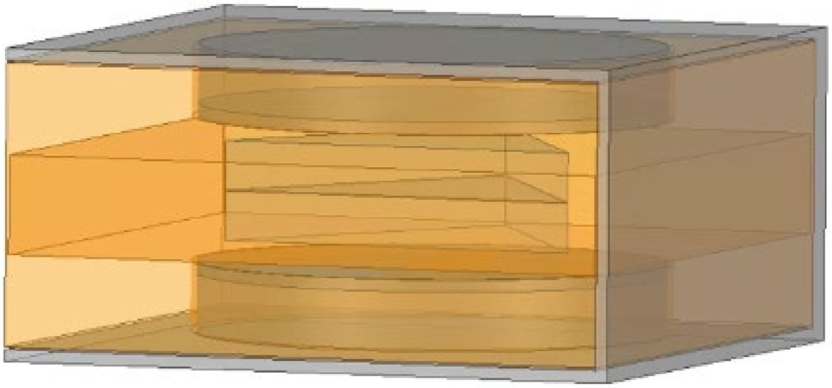

Figure 3.34: Ansys Maxwell simulation model of non-uniform biasing using permanent magnets. As the simulation is magnetostatic, all nonmagnetic materials are modeled as copper for visualization purposes. Magnetically, all that is present is the MuMetal C-clamp, the magnets, the pole pieces (MuMetal) under the magnets, and the ferrites in the center.

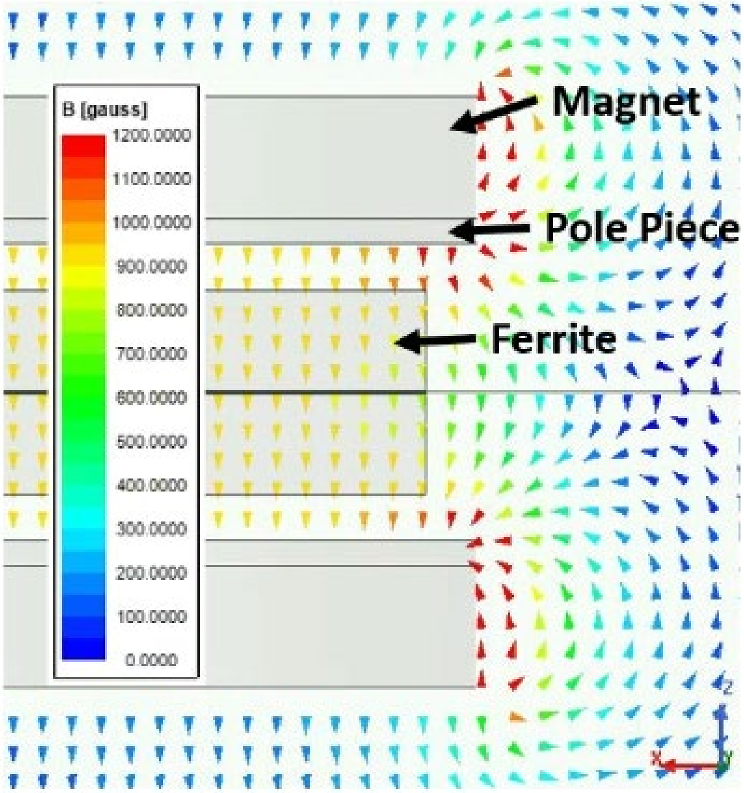

Figure 3.35: Vector plot of the simulated magnetic flux density in the circulator device, using stock magnets and MuMetal.

The simulation model described in 3.5.5 and seen in Figure 3.31 was reused for final tuning, with nonuniform biasing being the only difference of note. Figure 3.36 depicts the difference in full circulator device performance for uniform versus non-uniform biasing levels.

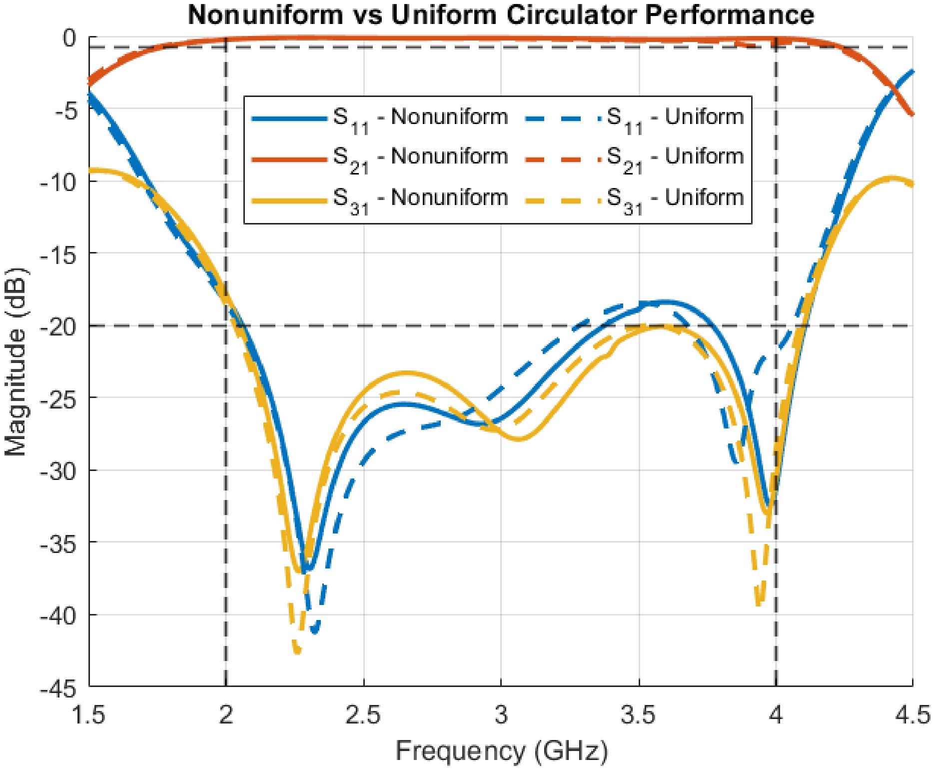

Figure 3.36: Circulator scattering parameters for ideal uniform biasing and permanent magnet non-uniform biasing.

3.6 Conclusion

An octave bandwidth ferrimagnetic below resonance circulator with surface mount integration was designed and simulated in stages. The closed form solution using the methods and equations discussed in Chapter 2 was found, in terms of the junction resonant frequency, input admittance, and quality factor. The necessary quarter wave transformer line impedances were additionally calculated, along with the required circuit dimensions and substrate electrical properties needed in order to realize a minimal footprint and realizable transmission line widths.

The magnetic biasing circuit that generates a magnetic field intensity high enough to magnetically saturate the ferrite junction was discussed and simulated, utilizing a magnetic

C-clamp and two ceramic magnets in order to minimize magnetic flux outside of the intended ferrite junction.

The surface mount integration method utilizing an air microstrip transmission line as a pseudo-wirebond was designed assuming perfect placement and a standard system impedance. The method in which steel screws were utilized to simultaneously act as cavity resonance suppressants in the circulator enclosure as well as additional structural rigidity in the surface mount implementation was discussed in full.

When the circulator was fully designed in a closed-form fashion, the circulator was simulated and stress-tested in stages using Ansys HFSS. The core of the circulator, the ferrite junction, was first discussed with the possible resonant frequency, input admittance, and quality factor trade-off space shown for a variety of variables. When the junction was fine-tuned, the quarter wave transformers were tuned using a simplified hexagonal model of the enclosure, with the characteristic impedances of the lines extracted using a dedicated simulation design. The lines for ports 2 and 3 were then curved to allow for a rectangular enclosure whilst minimizing changes in performance. The air microstrip transmission line acting like a pseudo wirebond was simulated and found to have minimal reflection for most possible imperfect placements. Eigenmode simulations were performed to find mode suppressing via placements that would push the lowest order cavity resonance in the enclosure above the passband.

With the circulator designed, simulated, and stress-tested for a large quantity of variables, fabrication can begin. Once fabricated, the circulator will additionally need to be measured at low and high power conditions, in addition to room temperature and 100 °C conditions.

Chapter 4

Circulator Fabrication and Testing

The high power and high temperature ferrimagnetic below resonance circulator designed in Chapter 3 were fabricated, and its performance was measured. The fabrication method is shown, and the varying measurement setups are discussed in which performance can be garnered for low (-10 dBm) and high (47 dBm) power conditions, as well as room temperature (23°C) and high temperature (100°C) conditions. Measured results are seen to be imperfect and are discussed with possible causes simulated.

4.1 Testing Circuit Fabrication

As the circuit to be tested is designed with surface mount integration, a circuit board was designed on which the circulator could be tested. While the impact of the testing board impedance could be de-embedded out, it is a far simpler task to design the board with a system impedance of 50 Ω to minimize the impact on the circulator's performance as read by the vector network analyzer on which the circulator is measured. To allow simple ground connection and to have maximum control over the transmission line widths, the testing board was designed using grounded coplanar waveguide transmission lines, with the dimensions described in Section 3.5.3. Via holes corresponding to the mode suppressing vias in the circulator enclosure were milled into the substrate for surface mount integration purposes. This testing board can be seen as fabricated at the far left of Figure 4.1.

4.2 Circulator Fabrication

In order to fabricate the circulator, the enclosure, substrate, ferrites, and trace were subdivided into discrete pieces. All conductive pieces were fabricated by Fotofab, while the dielectric and ferrite pieces were fabricated by Island Ceramic. The center conductor was fabricated out of 50-micron-thick copper, while the enclosure was fabricated out of

8.5-mils-thick Nickel Silver. The cut locations in the dielectric substrate were chosen such that they did not occur over a transmission line, with the exception of the substrate to ferrite transition and for the trace coming in from port 1. The dielectric substrate pieces were fabricated out of 2-mm-thick MCT-20 from Pacific Ceramics. The ferrite pieces were fabricated out of 2-mm-thick CVG-1201 from Pacific Ceramics.

The conductive enclosure serving as the ground plane for the circulator was split into two major sections: One part that forms the bottom face and the four smaller side faces, and another part that forms the top face with extending fingers. When fabricated, the bottom part of the enclosure was folded into place with the bottom layer of dielectric and ferrite pieces in place. The side faces of the enclosure were then clamped and soldered together.

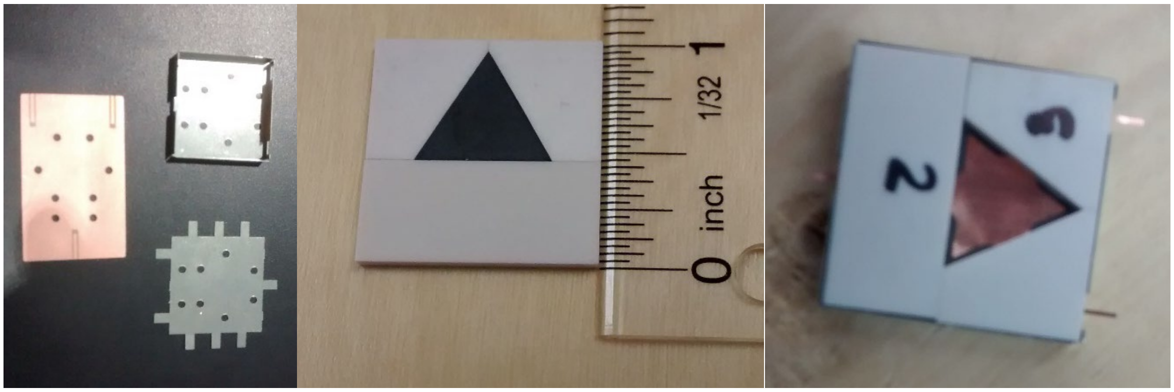

Figure 4.1: Testing board and enclosure pieces of the circulator (with vias) before assembly (left). Dielectric and ferrite blocks of one layer (middle). Circulator (no vias) in mid-assembly, with the bottom layer completed and the top layer dielectric inserted (right).

Once cooled, the center conductor was then slotted into place and pressed down to prevent movement by the upper layer of substrate and ferrite pieces. The top layer of the enclosure with bent fingers was then placed on top of the structure and clamped down. The edges of the top enclosure were then soldered to the edges of the bottom enclosure's side faces. The fingers were soldered to the side faces for extra structural rigidity.

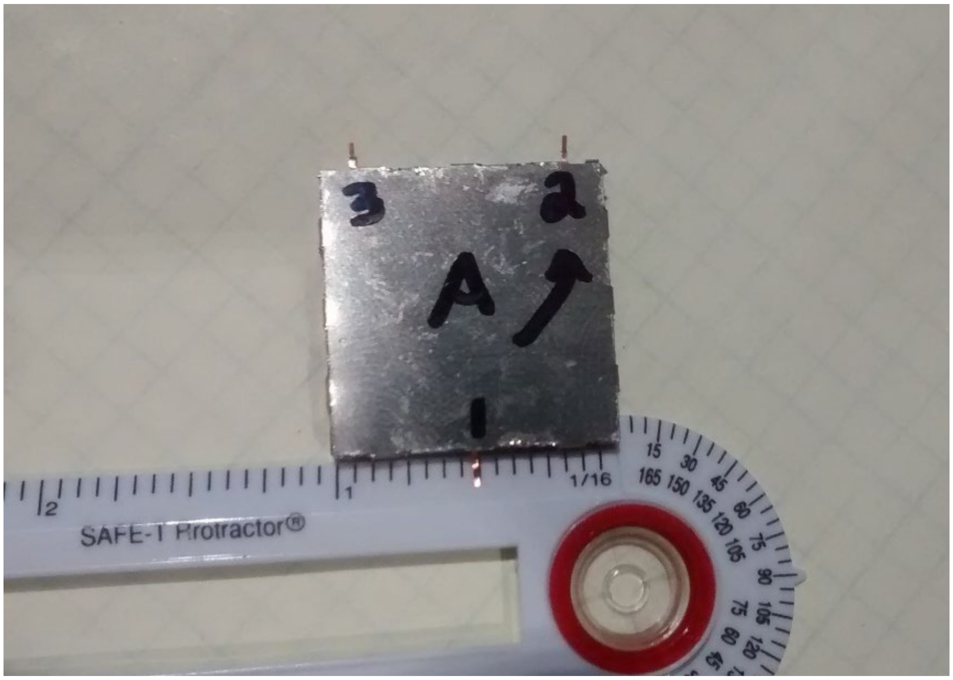

Figure 4.2: Circulator (without vias) in the final stages of assembly, become adhesion to the testing board.

Solder flux and solder paste were applied to the testing circuit board where it connects to the circulator enclosure. The circulator was then affixed to the testing board with the mode suppressing vias and then soldered down directly. The pseudo-wirebond air microstrip traces were realized by bending the traces with tweezers under a microscope. Pre-applied solder flux and solder paste on the testing board's grounded coplanar waveguide lines keep the wirebond in place once soldered down, requiring minimal solder. In case of unintended accidental contact between the transmission lines and the ground planes in the testing board's gap channels, tweezers were run through the gaps to remove the superfluous solder. The SMAs were then soldered into place, and the coplanar waveguide channels were once again cleared of solder. The end result of this process is depicted in Figure 4.3 (without vias) and Figure 4.4 (with vias).

Figure 4.3: Fully fabricated initial circulator prototype, without vias.

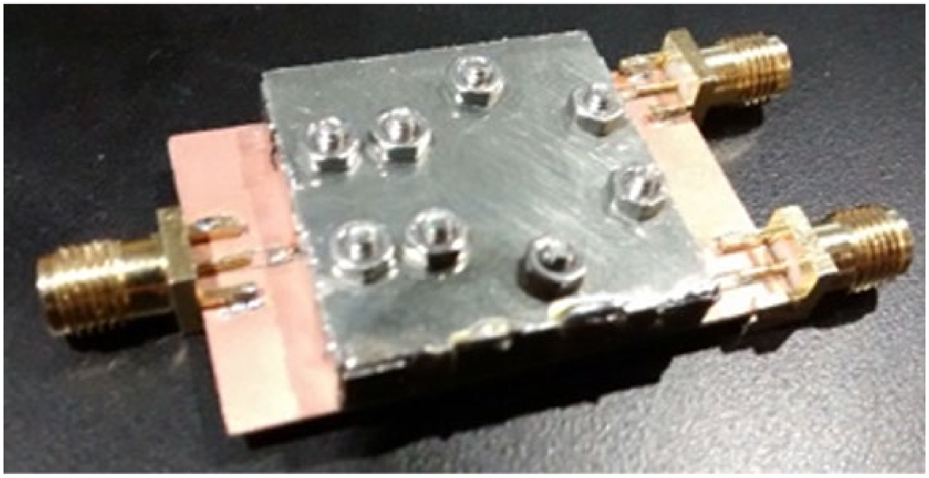

Figure 4.4: Fully fabricated circulator prototype, with steel screws used as mode suppressing vias.

After experimentation with direct drilling, the substrate material proved far too thick and brittle to drill through using the tools and equipment available to the author, and as such, it was outsourced to Island Ceramics. Corresponding holes were milled into the circulator's metal enclosure and testing board using an LPKF ProtoMat S103 milling machine, and 2-

mm screws were inserted into the structure. In total, these screws serve to hold the structure together, act as mode suppressing vias, and act as a strong electrical connection between all the ground planes in the circuit.

After initial measurements, it was found that the fabrication process did not provide a uniform and consistent connection with the dielectric blocks, equivalent to an air gap between all pieces. Ultimately, this issue was solved by incorporating indium foil from Custom Thermoelectric. The analysis that leads to the inclusion of indium foil as a compressible conductor, as well as the impact in performance this ultimately made, is detailed in Chapter 5.

4.3 General Measurement Setup

The circulator in all measurement cases was measured using an Agilent Technologies N5242A PNA-X vector network analyzer and calibrated for three ports at 50 Ω using an Agilent N4691-60006 electronic calibration module. For an initial discussion of the circulator's performance, the circulator was biased using electromagnets, allowing a sweep of magnetic bias strength through the use of DC power supplies.

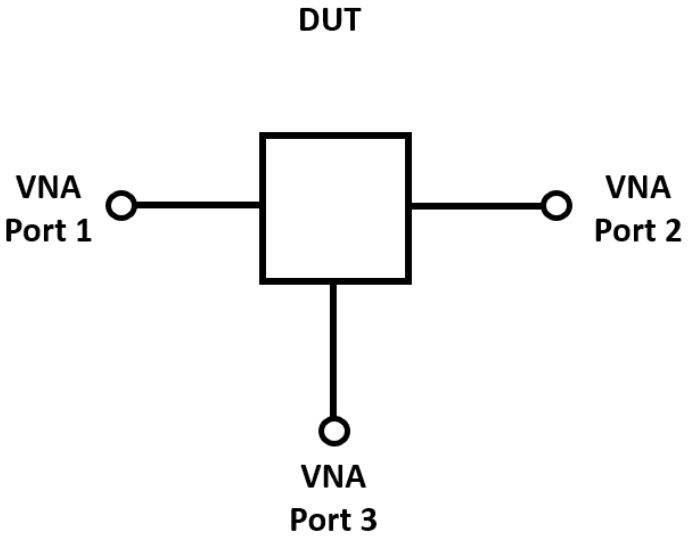

Figure 4.5: Circuit diagram of the generalized circulator set-up meant for quick testing at room temperature and low power conditions.

After measurement, the input impedance of the three-port circulator was extracted by converting the measured S parameters into Z parameters and then subsequently using the following relation that is simply derived from the Z parameter definition:

$$[V] = [Z][I] \quad \rightarrow \quad \begin{bmatrix} V_1 \\ V_2 \\ V_3 \end{bmatrix} = \begin{bmatrix} Z_{11} & Z_{12} & Z_{13} \\ Z_{21} & Z_{22} & Z_{23} \\ Z_{31} & Z_{32} & Z_{33} \end{bmatrix} \begin{bmatrix} I_1 \\ I_2 \\ I_3 \end{bmatrix} \tag{4.1}$$

where V_n and I_n refer to the voltage and current at the n-th port. The load impedance at ports 2 and 3 are known to be matched and calibrated to 50 Ω, leading to the relation between the voltages and currents at ports 2 and 3 to be:

$$V_2 = -Z_{L2}I_2 \qquad V_3 = -Z_{L3}I_3 \tag{4.2}$$

Plugging this relation into (4.1) and rearranging leads to the relation:

$$\begin{gathered} \begin{bmatrix} V_1 \\ -Z_{L2}I_2 \\ -Z_{L3}I_3 \end{bmatrix} = \begin{bmatrix} Z_{11} & Z_{12} & Z_{13} \\ Z_{21} & Z_{22} & Z_{23} \\ Z_{31} & Z_{32} & Z_{33} \end{bmatrix} \begin{bmatrix} I_1 \\ I_2 \\ I_3 \end{bmatrix} \\ \rightarrow \quad \begin{bmatrix} V_1 \\ 0 \\ 0 \end{bmatrix} = \begin{bmatrix} Z_{11} & Z_{12} & Z_{13} \\ Z_{21} & Z_{22} + Z_{L2} & Z_{23} \\ Z_{31} & Z_{32} & Z_{33} + Z_{L3} \end{bmatrix} \begin{bmatrix} I_1 \\ I_2 \\ I_3 \end{bmatrix} \end{gathered} \tag{4.3}$$

Cramer's rule for solving systems of linear equations can then be used to extract the ratio of voltage to current at port 1 when ports 2 and 3 are loaded, better known as the input impedance:

$$Z_{in} = \frac{V_1}{I_1} = \frac{\begin{vmatrix} Z_{11} & Z_{12} & Z_{13} \\ Z_{21} & Z_{22} + Z_{L2} & Z_{23} \\ Z_{31} & Z_{32} & Z_{33} + Z_{L3} \end{vmatrix}}{\begin{vmatrix} 1 & Z_{12} & Z_{13} \\ 0 & Z_{22} + Z_{L2} & Z_{23} \\ 0 & Z_{32} & Z_{33} + Z_{L3} \end{vmatrix}} \tag{4.4}$$

This equation calculates the input impedance as seen from port 1 with known loads at ports 2 and 3 but can be modified such that one can calculate the input impedance for the other ports.

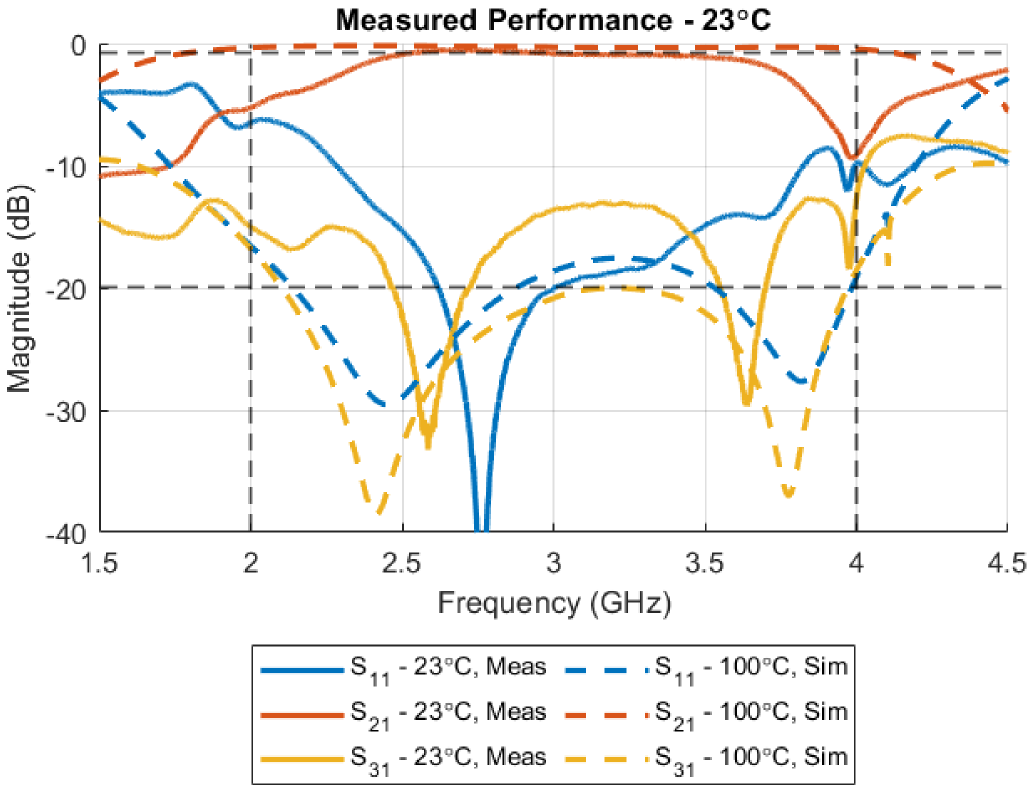

Figure 4.6: Room temperature measurement scattering parameters at low power conditions.

The circulator measured at room temperature was biased such that the externally applied magnetic field was 700 Oe. As at room temperature, the magnetic saturation of the ferrites is 1200 G, as the ferrites are not saturated at this biasing level. Thus, the performance of the circulator is far from that simulated under ideal conditions, as can be seen in Figure 4.6. Under this condition, the circulator operates at approximately the same center frequency but with greatly reduced bandwidth and isolation.

4.4 High Power Measurement

The prototype circulator was then measured under high power conditions, in steps from -10 dBm to 47 dBm. As the Agilent Technologies N5242A PNA-X vector network analyzers (VNAs) used could not handle power levels this high, a high power test setup was devised to bring the power in the device under testing (DUT) up to 47 dBm while only sourcing minimal power from the VNA. The circuit used to accomplish this, along with a picture of the actual setup, are depicted in Figure 4.7 and Figure 4.8, respectively.

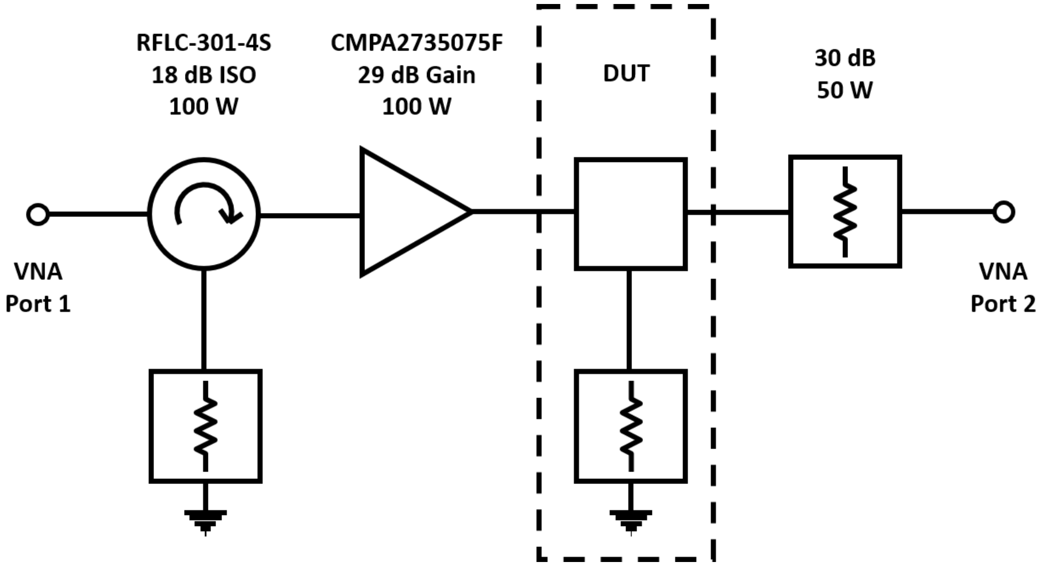

Figure 4.7: Circuit diagram of the high power test setup for the circulator prototype.

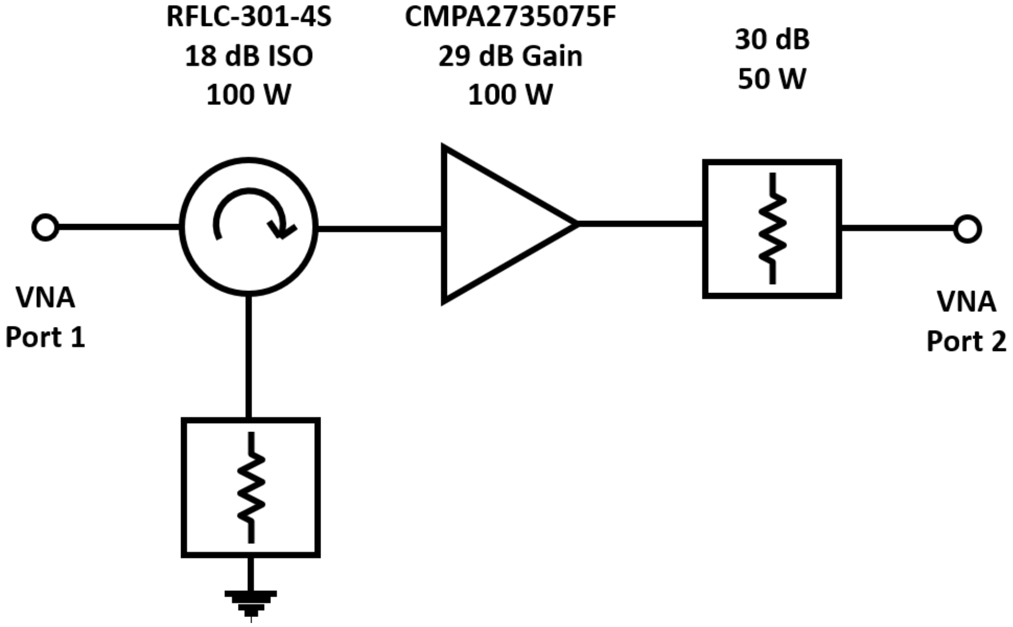

Figure 4.8: Reference circuit diagram of the high power test setup for the circulator prototype.

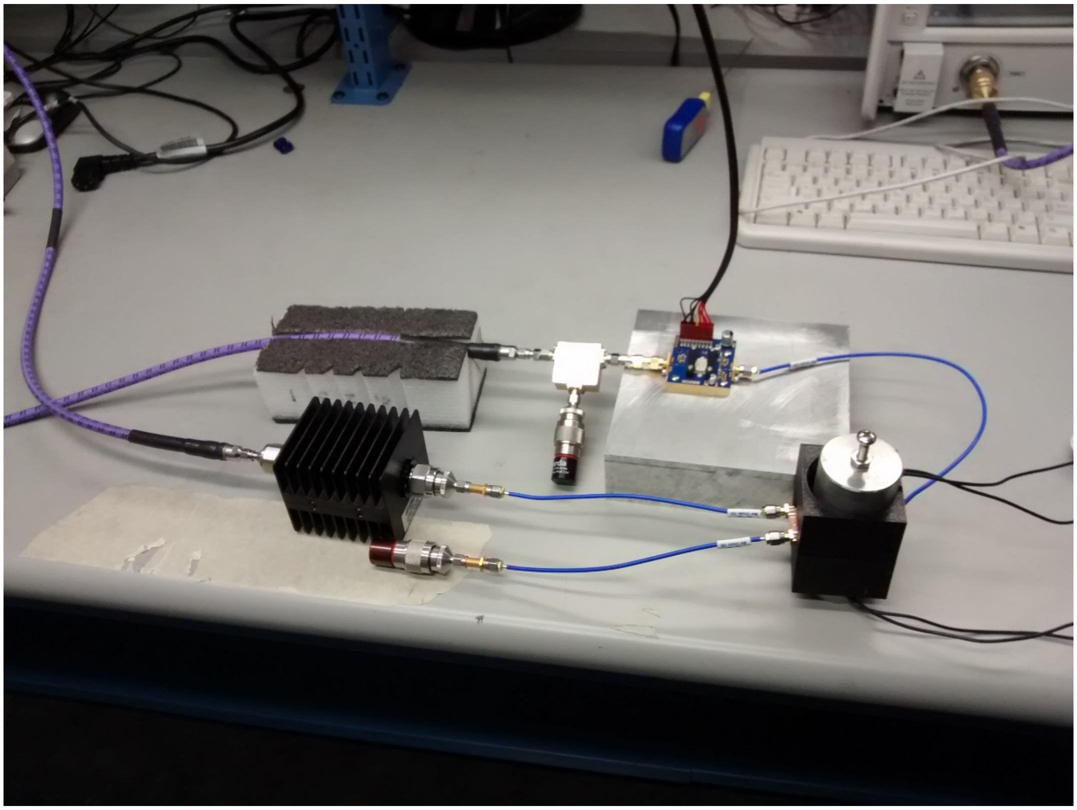

Figure 4.9: High power circulator test setup for scattering parameter measurement.

As the scattering parameters of the circulator could not be extracted directly, what was measured instead was the drop in insertion loss at the center frequency of 3 GHz. The value to be extracted here is the P_{1dB} point, the point at which the RF magnetic field H_{RF} is strong enough to generate spin-waves and transmitted power for a given signal level has fallen to 1 dB beneath transmitted power at -10 dBm. This value was extracted by comparing the drop in performance of the measured insertion loss for the reference circuit without the circuit being tested versus the circuit with the device under test.

As detailed in Chapter 3, the expected power handling of this circulator at room temperature is 24 dBm ($H_{RF} = 2.33\ Oe$), very near the measured values seen in Figure 4.10.

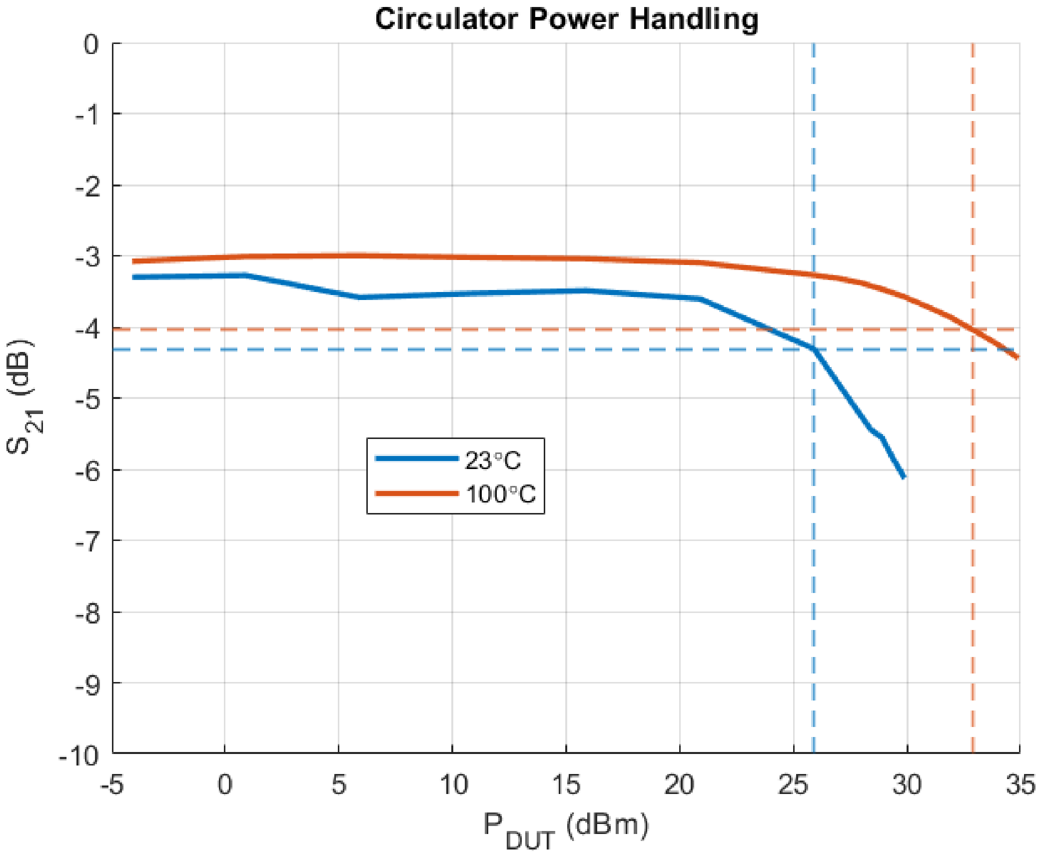

Figure 4.10: Measured insertion loss of the full test circuit as a function of the amplifier output power. P_{1dB} point is the level at which the spin-waves become excited, and the dramatic spike in insertion loss begins. Depicted are the results for room temperature (left) and 100 °C (right).

4.5 High Temperature Measurement

As the circulator is designed for operation at 100°C, the response at room temperature (~23°C) is predictably suboptimal, as the magnetic saturation level $4\pi M_S$ is much higher than the design value. Thus, the circulator needed to be measured at 100°C.

Due to calibration concerns for high temperature conditions, the VNA used in previous sections was electronically calibrated at room temperature (23°C), and a through-line microstrip transmission line was fabricated from Rogers RO4350B substrate, and measured from 1 GHz to 5 GHz, the intended measuring range of frequencies for the circulator. The through-line was then heated to 100 °C via a hot plate and a heat gun, as depicted in Figure 4.11.

The performance of the through-line for both temperature extremes was plotted in Figure 4.11. Both the return loss and the insertion loss are found to differ minimally between temperature extremes. From the performance, it was decided that the VNA would not need recalibrating at high temperatures and was thus calibrated at room temperature for three ports in order to measure the performance of the circulator at all ports.

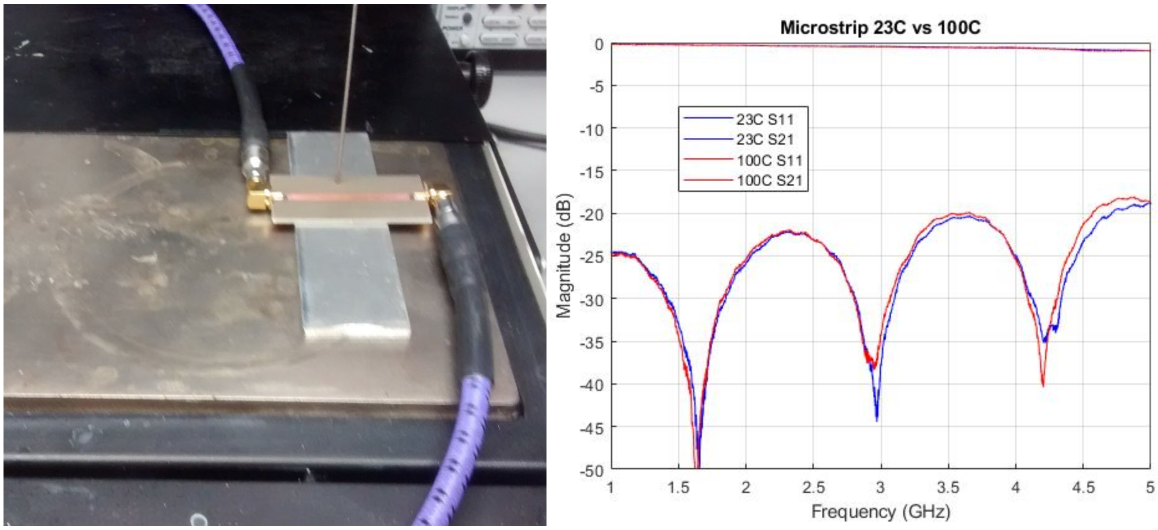

Figure 4.11: High temperature calibration test through line undergoing measurement (left). Measured through line performance at room temperature and high temperature (right).

The circulator was tested at 100 °C, which was accomplished simply by heating the circulator under measurement via a hot plate underneath, and a heat gun overhead. The temperature was measured using a Westward 2LTC6 thermometer. Scattering parameter measurements were taken after twenty minutes to allow the entire device to heat up thoroughly.

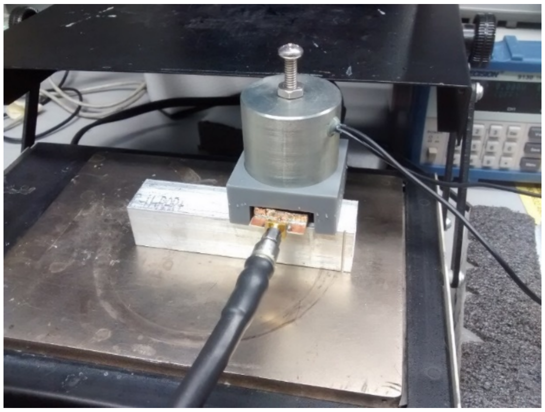

Figure 4.12: High temperature circulator test setup for scattering parameter measurement.

The scattering parameters of the circulator at room temperature and at 100 °C are shown in Figure 4.13, in addition to the idealized high temperature performance. The performance improves as temperature increases, albeit not enough to perfectly align with the ideal simulated performance. Several possible causes of this drop in performance are investigated in Section 4.6. As the temperature increases, the bandwidth and the isolation in the passband noticeably increase, albeit with reduced return loss for the majority of the frequencies in the passband.

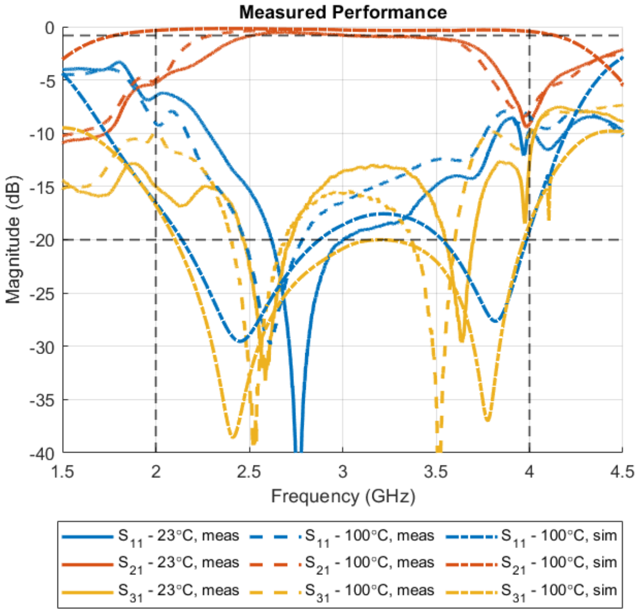

Figure 4.13: Measured circulator scattering parameters for room temperature (23°C) and 100°C. The idealized simulated performance is additionally plotted.

The circulator at high temperature was additionally tested at high power levels, with a maximum of 35 dBm in the circulator under test. The P_{1dB} point at which spin-waves begin absorbing power was displayed previously in Figure 4.10, and is seen to be significantly higher than that measured at room temperature at 32.9 dBm, as expected from the decrease in magnetic saturation, allowing higher H_{RF} levels before spin-wave power absorption begin to take effect.

4.6 Circulator Performance Investigation

The performance of the circulator at high temperature conditions is readily seen to not perfectly match the idealized performance, as depicted in Figure 4.13. Electromagnetically, a multitude of causes could be responsible, with a non-uniform magnetic biasing, imperfect thermal conduction, and a frequency dispersive dielectric constant likely being at fault.

The first potential cause of imperfect performance analyzed was that of non-uniform magnetic biasing. During high temperature measurements, the fabricated circulator was biased using a single electromagnet, oriented above the device as in Figure 4.12. While the electromagnet has a large enough radius to provide an approximately uniform biasing field in $\hat{x}$ and $\hat{y}$, the variation in the biasing field along $\hat{z}$ is highly variable along the ferrite pieces. This non-uniformity was simulated in Ansys HFSS as in Chapter 3 by subdividing each ferrite block into three independently biased ferrite layers, for a total of six layers, as in Figure 4.14. The internal biasing field (H_{int}) of each ferrite layer was defined as a linear gradient between the internal biasing of the top and bottom layers, H_1 and H_2 respectively. The biasing levels were defined to have their average equal to the ideal internal biasing of 0 Oe. As the circulator was biased from above, the biasing of the top layer is stronger than the bottom layer, leading to the relation:

$$\begin{gathered} H_1 = -H_2 \\ H_1 \geq H_2 \end{gathered} \tag{4.5}$$

Lumped in this simulation is a variation on the magnetic saturation value of the ferrite blocks, which, as discussed in Chapter 2 is broadly inversely related to temperature. At room temperature (~25 °C), the magnetic saturation of the ferrites is 1200 G, while at 100 °C, it is

900 G. Due to the open-air environment of the high temperature measurement and the high surface area of thermally conductive materials in the fabricated circulator, it is possible that a large degree of heat conducted away from the center of the device, and thus the ferrite blocks, after heating, leading to a higher than expected magnetic saturation in the center of the device. Thus, the magnetic saturation value for the ferrite layers in the simulation was swept in 100 G increments from 900 G to 1200 G.

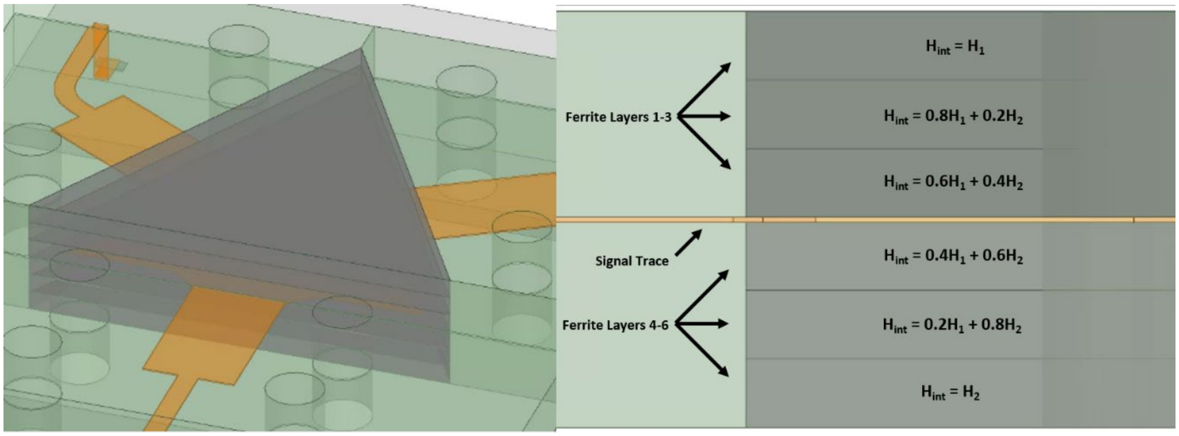

Figure 4.14: HFSS simulation model of the single magnet non-uniform biasing condition. The model is depicted isometrically (left) and from the side (right). Each ferrite is segmented into three discrete pieces with equivalent material definitions and slightly differing magnetic biases.

The simulated performance of the circulator worsens as the ferrite magnetic saturation increases, as expected from a deviation from nominal. As the temperature of the ferrites increase, the bandwidth, isolation, and return loss all increase substantially. Additionally, as the biasing differential increases, the performance of the circulator at lower frequencies in the passband decreases due to the impact in the ferrite junction resonator characteristics. It is thus hypothesized that the ferrite blocks were not sufficiently heated, in addition to not being uniformly biased along $\hat{z}$.

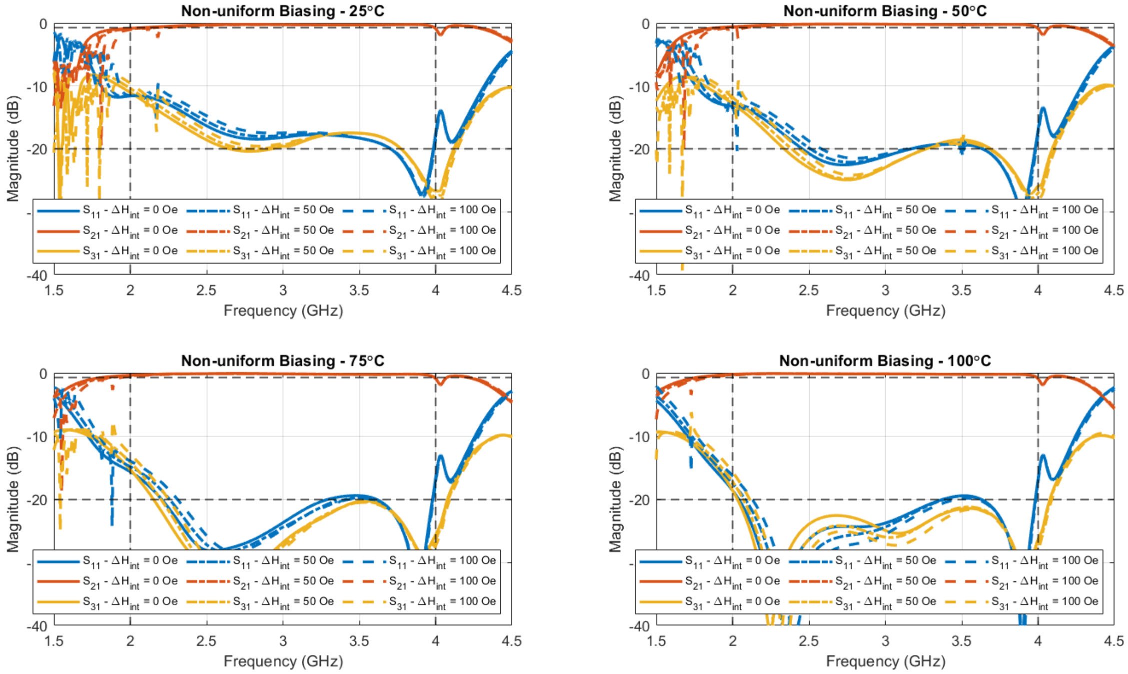

Figure 4.15: Simulation results for the single magnet non-uniform biasing condition. For each temperature, the difference in the internal bias between the highest and lowest ferrite $\Delta H_{int} = H_1 - H_2$ was varied from 0 Oe to 100 Oe. The saturation magnetization of the ferrite layers was varied in the simulation inversely with temperature, from 25 °C (1200 G) to 100 °C (900 G).

The third potential cause of imperfect measurement investigated was the possibility of the dielectric substrate in the circulator enclosure having a higher than expected frequency and temperature dependency. While the relative permittivity of MCT-20 in S-band is not published, data exists for 354 MHz ($\varepsilon_r = 18.9$) and 9.4 GHz. ($\varepsilon_r = 20.0$) [41]. No data on the temperature dependence of the relative permittivity of MCT-20 was found, although comparable materials such as PD-20 [42] have a relative permittivity temperature coefficient of $135^{-6}\ C^{-1}$, indicating that MCT-20 would have only a negligibly higher dielectric constant at 100 °C. Nevertheless, the dielectric constant of the dielectric in the simulation was swept from 15 to 20 in increments of 2.5.

The performance of the simulated circulator with a change in the dielectric's relative permittivity is found to have significantly reduced bandwidth, isolation, and return loss as the quarter-wave transformers become electrically shorter, as in Figure 4.16.

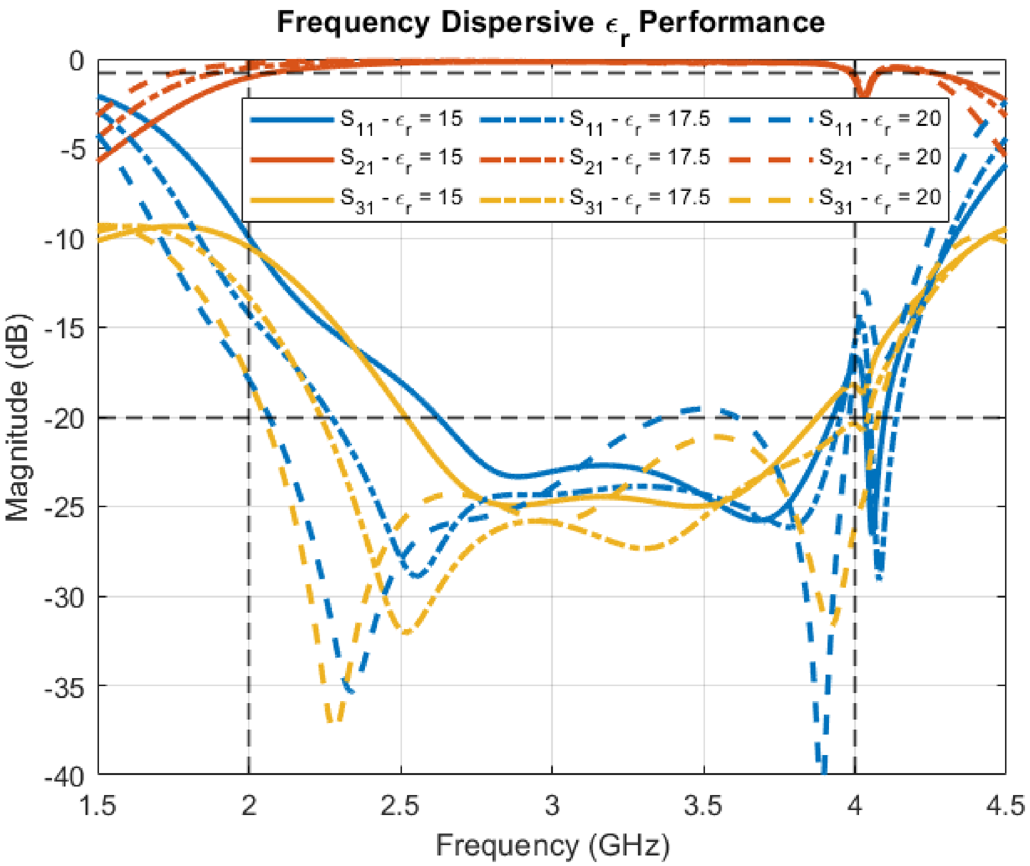

Figure 4.16: Simulation results for the frequency dispersive dielectric constant of the dielectric substrate condition. The MCT-20 material used in the fabrication of the circulator has a dielectric constant of approximately 20.0 at 9.4 GHz and 18.9 at 354 MHz [41]. The dielectric constant of the material was varied in simulation from 15 to 20 in increments of 2.5.

4.7 Conclusion

The below resonance octave bandwidth surface mountable circulator designed and simulated in Chapter 3 was fabricated and tested for a variety of power and temperature conditions. The fabrication and measurement process was shown and discussed in detail to allow replication of the shown scattering parameter results. The P_{1dB} point at which spin waves begin to take effect was measured for both temperature extremes as a function of power inside the DUT.

Two major types of prototypes were fabricated and tested. The original (whose performance is not shown in this chapter) without mode suppressing vias was found to have extremely poor performance, with low return loss and resonances and spurs across the entire passband. Several fabrication errors were isolated and corrected, as will be discussed in Chapter 5. After these errors were corrected, the prototype as shown in this chapter was measured and the results were shown.

While the performance of the fabricated circulator increased as the ambient temperature increased, there is some disagreement between the measured results and the simulated results. Several possible causes were investigated via simulation, with the most probable culprit being the relative permittivity of the enclosure's substrate differing from specifications, as a function of both frequency and temperature. In addition, it was found that the prototype heating method was imperfect, and the core of the circulator enclosure (the ferrite junction itself) never truly reached the ambient temperature, thus lowering performance.

Chapter 5

Time Domain Impedance Analysis

A time domain impedance analysis method is defined and demonstrated on an example 5th order Chebyshev bandpass filter. This analysis method is able to be used to see the input impedance of a device as a function of time in order to find the locations at which a circuit is faulty. The analysis method is applied to the circulator to solve several fabrication issues that were found in the development of this thesis.

5.1 Time Domain Impedance Analysis Theory

With regards to filters, especially high order filters, an unfortunate reality in their realization is a virtual guarantee of a long and arduous tuning process to achieve the idealized simulated performance. This process is made more complex and unintuitive by the coupling and interaction between individual resonators making up the physical filter. This is even further complicated by the fact that two resonators, if mistuned in the same manner, can alter the filter's performance in exactly the same way when viewing the performance of the filter as scattering parameters in dB versus frequency, as is very often the case. One method to make this tuning process immensely easier is by transforming the filter's measured return loss into the time domain, as devised by [43]. By necessity, the data transformed can't be over all frequency as a bandpass filter that is designed for a given center frequency f_0 will also have a passband at many, but not necessarily all, integer multiples of the center frequency $n \cdot f_0$ (Combline filters being an example of a filter that does not have a passband at $2 \cdot f_0$ [44]). Instead, the frequency data being transformed must be windowed, centered at the center frequency f_0. Additionally, the filter being analyzed must be a bandpass filter, meaning the return loss data must be 0 dB at the window edges. This provides an unfortunate upper limit on the tuning resolution, which is further reduced as the window shrinks.

Previous authors recommend that the frequency window be several times larger than the filter bandwidth in order to provide enough resolution to adequately tune [45].

5.2 Time Domain Impedance Analysis Example

Traditionally, this analysis method is used in tuning high-order filters. However, the mathematics behind the method remains valid for lower-order filters, including circulators. As circulators can be modeled as a first-order directional filter, they may be analyzed using many of the same methods that are used on passive filters, including the time domain impedance analysis method in question.

Before applying this method to the circulator in question, it is important useful to see this analysis method in practice. As an example, an arbitrary 5th order Chebyshev ripple bandpass filter with coupled line topology was devised for a fractional bandwidth of 400 MHz (7.14%) with a center frequency of 5.6 GHz, with an insertion loss ripple of 0.1 dB [15]. Before the geometry of the filter can be calculated, the low pass filter equivalent of the filter normalized for a cutoff frequency ω_c of 1 rad/s and system impedance Z_0 of 1 Ω needs to first be derived and then scaled to the desired center frequency and system impedance.

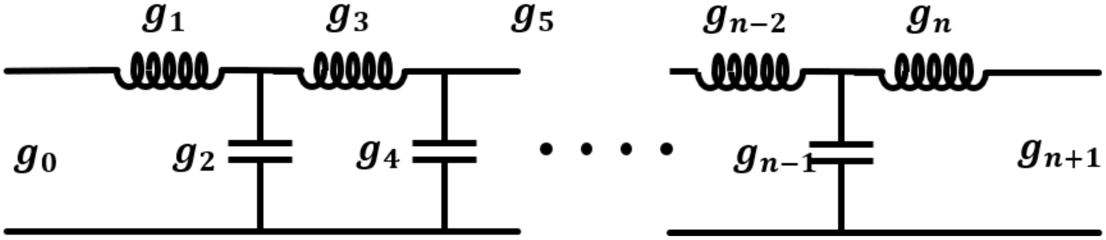

Figure 5.1: LC ladder circuit for an arbitrary order low pass filter.

The key variables that must be known to design a lossless, low pass filter with a Chebyshev style ripple in the passband are the filter order n, the passband ripple specified for either insertion loss (L_A) or return loss (L_R), and the filter bandwidth, expressed fractionally (FBW). This low pass filter is composed of an alternating sequence of series inductors and shunt capacitors, with the total number of elements equal to the filter order, as in Figure 5.1. For a Chebyshev style ripple in the passband, akin to that used in broadband ferrimagnetic circulators, the inductance and capacitance of the elements in the filter are described solely by parameters called "g-coefficients." For design purposes, it is the engineer's choice as to whether the inductor or capacitor element is the first element in the ladder. In the aforementioned figure, one can see that the quantity of g-coefficients is two greater than the filter order. The first and last g-coefficients, g_0 and g_6, represent the port impedances of the filter, which, as mentioned, are currently 1 Ω. For a Chebyshev ripple in the passband, the g-coefficients can be calculated by first calculating the intermediate variables ε and η, which depend on either the return loss ripple (RL) or insertion loss ripple (IL) specified in dB:

$$\varepsilon = \sqrt{10^{IL/10} - 1} \quad OR \quad \varepsilon = \frac{1}{\sqrt{10^{RL/10}}}$$
$$\eta = sinh\left[\frac{1}{n} sinh^{-1}\left(\frac{1}{\varepsilon}\right)\right] \tag{5.1}$$

The g-coefficients are then iteratively calculated using:

$$g_0 = 1$$
$$g_r g_{r+1} = G_r = \frac{4sin\left(\frac{(2r-1)\pi}{2n}\right) sin\left(\frac{(2r+1)\pi}{2n}\right)}{\eta^2 + sin^2\left(\frac{r\pi}{n}\right)} \tag{5.2}$$
$$g_{r+1} = \frac{G_r}{g_r}$$

The final g-coefficient that represents the port impedance of the output port depends on if the filter is of an even or odd order:

$$g_{n+1} = 1 \quad for\ n\ odd$$
$$g_{n+1} = \left(\varepsilon + \sqrt{1 + \varepsilon^2}\right)^2 \tag{5.3}$$

Ultimately, the g-coefficients for this filter are calculated to be:

$$g_0 = g_6 = 1, \qquad g_1 = g_5 = 1.1468$$
$$g_2 = g_4 = 1.3712, \qquad g_3 = 1.9750 \tag{5.4}$$

Once the g-coefficients of the low pass prototype are known, the filter is converted to the desired filter type, in this case, bandpass. Then, the filter is scaled with frequency such that the predesignated corner or center frequency, whichever is applicable.

When converting from a low pass filter prototype to a bandpass filter prototype, each inductor is paired with a capacitor in a series connection to generate a resonance, and each capacitor is paired with an inductor in parallel to generate an antiresonance. Each element in this new bandpass filter is calculated using:

$$\begin{aligned} L_r &= \frac{g_r Z_0}{2\pi f_0 \Delta} && \text{for series inductors} \\ L_r &= \frac{Z_0 \Delta}{2\pi f_0 g_r} && \text{for shunt inductors} \\ C_r &= \frac{\Delta}{2\pi f_0 Z_0 g_r} && \text{for series capacitors} \\ L_r &= \frac{g_r}{2\pi f_0 Z_0 \Delta} && \text{for shunt capacitors} \end{aligned} \tag{5.5}$$

where Δ is the fractional bandwidth, Z_0 is the system impedance, and f_0 is the center frequency of the filter.

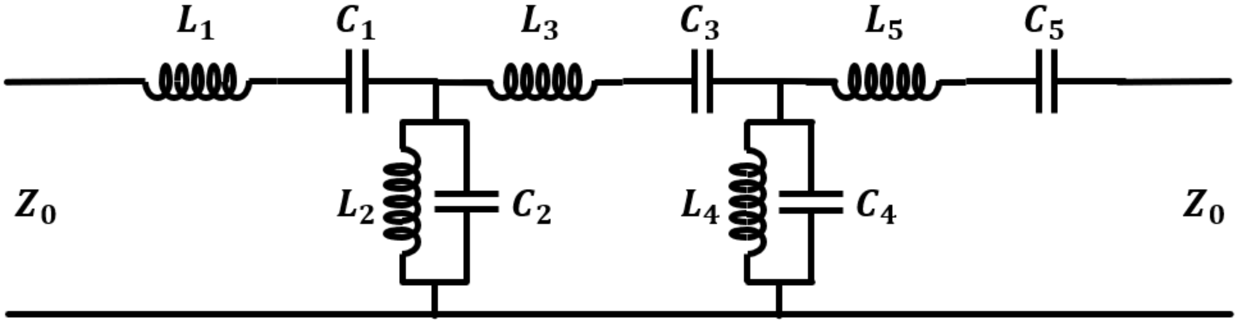

Figure 5.2: Lossless LC circuit for a 5th order bandpass filter.

One of many possible physical implementations of a distributed element filter of this type is a coupled line filter. When two transmission lines are parallel to one another, power can be heavily coupled between the lines, in effect generating a single new three-wire transmission line. The impedance and propagation constant on this line can be described and calculated at any point along the line by the capacitance between the three wires in the mode, the microstrip or stripline lines, and the ground plane. The characteristic impedance of the line is described by a combination of the even and odd mode impedance of the line, each defined by the direction of current flow on each line, as depicted in Figure 5.3 and Figure 5.4. Even mode being defined as the characteristic impedance when the current flow on each line is equivalent and in the same direction, effectively forming an H-wall between the lines. The odd mode is defined as the characteristic impedance when the current flow on each line is equivalent and in the opposite direction, effectively forming an E-wall between the lines.

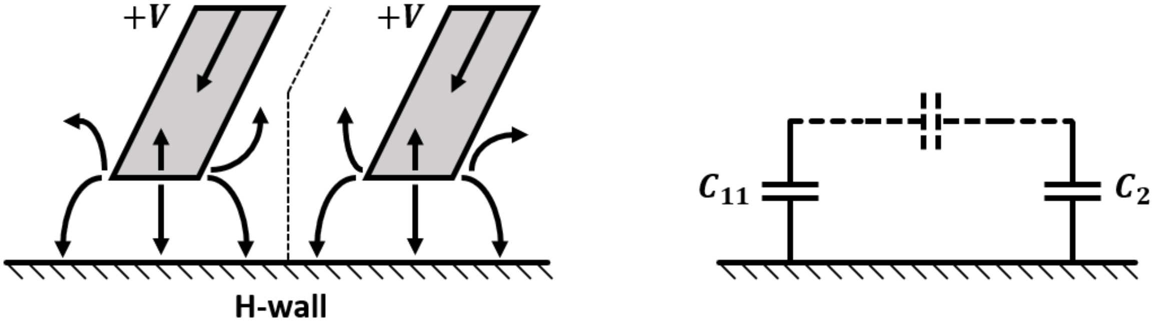

Figure 5.3: Electric field vectors and circuit diagram for an even mode excitation of a coupled line transmission line.

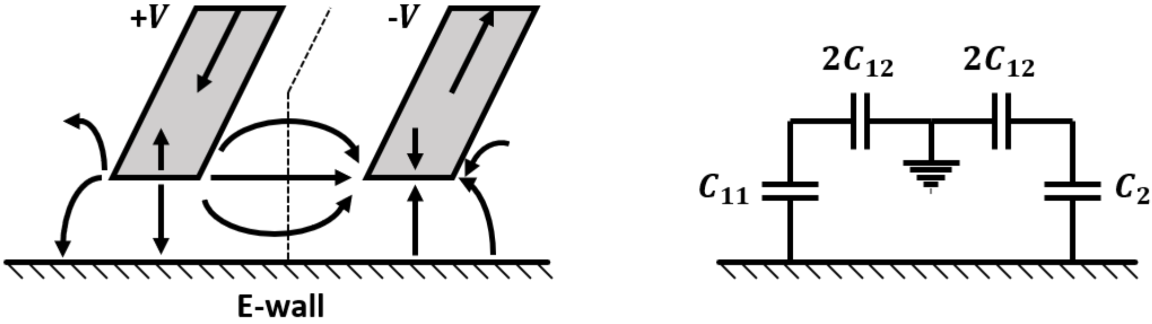

Figure 5.4: Electric field vectors and circuit diagram for an off mode excitation of a coupled line transmission line.

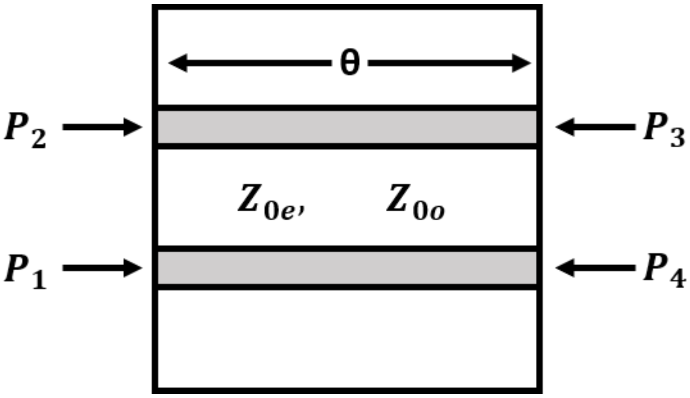

Figure 5.5: Definition of the ports for a coupled line transmission line segment.

Treating a section of the coupled line as a four-port network with the ports defined as depicted in Figure 5.5, the elements of the impedance matrix Z are derived:

$$\begin{aligned} Z_{11} &= Z_{22} = Z_{33} = Z_{44} = \frac{-j}{2}(Z_{0e} + Z_{0o}) \cot\theta \\ Z_{12} &= Z_{21} = Z_{34} = Z_{43} = \frac{-j}{2}(Z_{0e} - Z_{0o}) \cot\theta \\ Z_{13} &= Z_{31} = Z_{24} = Z_{42} = \frac{-j}{2}(Z_{0e} - Z_{0o}) \csc\theta \\ Z_{14} &= Z_{41} = Z_{23} = Z_{32} = \frac{-j}{2}(Z_{0e} + Z_{0o}) \csc\theta \end{aligned} \tag{5.6}$$

A coupled line transmission line of electrical length $\theta = \beta l$ with the port definitions and terminations as seen in Figure 5.5 is equivalent to a -90° impedance inverter with a transmission line of electrical length $\theta = \beta l$. Each transmission line segment can, in turn, be represented as an LC element shunt resonator, as in Figure 5.2, thus making a cascading connection of coupled lines as in Figure 5.6. that can be fully represented by Figure 5.2.

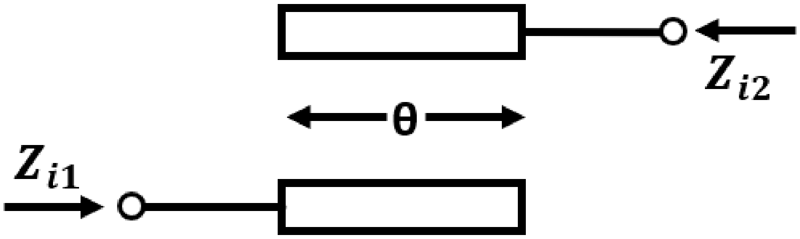

Figure 5.6: Simplified circuit schematic for a section of a coupled line filter.

The impedance of each coupled line segment can be extracted from the even and odd mode impedances of the lines, in addition to the electrical length of the lines:

$$Z_{i1} = \frac{\sqrt{(Z_{0e} - Z_{0o})^2 - (Z_{0e} + Z_{0o})^2 cos^2\theta}}{2sin\theta} \tag{5.7}$$

The characteristic impedance of each impedance inverter relative to the system impedance JZ_0 for each quarter-wavelength coupled line segment is defined using:

$$\begin{gathered} J_1 Z_0 = \sqrt{\frac{\pi\Delta}{2g_1}} \\ J_r Z_0 = \frac{\pi\Delta}{2\sqrt{g_{r-1}g_r}} \qquad for\, r = 2, 3, \dots, n \\ J_{n+1} Z_0 = \sqrt{\frac{\pi\Delta}{2g_n g_{n+1}}} \end{gathered} \tag{5.8}$$

Once this value is known for a given coupled line section, the even and odd mode impedances required to produce this value are given by:

$$\begin{aligned} Z_{0e} &= Z_0[1 + JZ_0 + (JZ_0)^2] \\ Z_{0o} &= Z_0[1 - JZ_0 + (JZ_0)^2] \end{aligned} \tag{5.9}$$

One will note that $n + 1$ coupled line segments are required due to the inclusion of the initial feeding line at system impedance. For a Rogers RO4350B substrate with a thickness of 20 mils, the necessary dimensions, and impedances to realize a filter of this type are as detailed in Table 5.1.

Table 5.1: Coupled line filter dimensions and impedances.

r	g_r	Z_{0e} (Ω)	Z_{0o} (Ω)	W (mm)	S (mm)
0	1.0000	N/A	N/A	N/A	N/A
1	1.1468	70.53	39.25	0.876	0.145
2	1.3712	54.87	45.93	1.088	0.755
3	1.9750	53.64	46.83	1.097	0.967
4	1.3712	53.64	46.83	1.097	0.967
5	1.1468	54.87	45.93	1.088	0.755
6	1.0000	70.53	39.25	0.876	0.145

This filter was modeled and simulated using Ansys HFSS, with the model as depicted in Figure 5.7 with the performance as depicted in Figure 5.8. With the physical realization of the ladder element filter in Figure 5.2 now known, both filters were deliberately mistuned by reducing the capacitance in resonators 2 and 4 by decreasing the length of resonators 2 and 4 by 1 mm near the middle of the filter, as pictured in Figure 5.7, independently. The middle resonator, resonator 3, was not shortened to compensate. The ports in the HFSS model were de-embedded to the first coupled line segment to maintain symmetry. Scattering parameter results for both models in the frequency domain and the time domain are depicted in Figure 5.8. The frequency window used to convert to the time domain was 4 GHz to 7.2 GHz. The input impedance for both models was calculated by converting the extracted return loss into an impedance matrix (Z) as described in Section 4.3, and then using:

$$Z_{in} = \frac{V_1}{Z_1} = \frac{\begin{vmatrix} Z_{11} & Z_{12} \\ Z_{21} & Z_{22} + Z_L \end{vmatrix}}{\begin{vmatrix} 1 & Z_{12} \\ 0 & Z_{22} + Z_L \end{vmatrix}} = Z_{11} - \frac{Z_{12}Z_{21}}{Z_{22} + Z_L} \tag{5.10}$$

As can be seen from the time domain return loss, a peak occurs for every resonator that is reached chronologically. When the capacitance in a resonator is decreased by shortening the length, the return loss remains identical to the matched performance until the corresponding return loss peak is significantly lessened, and the measured return loss of the filter increases beyond this point, as the majority of power being reflected is at this point.

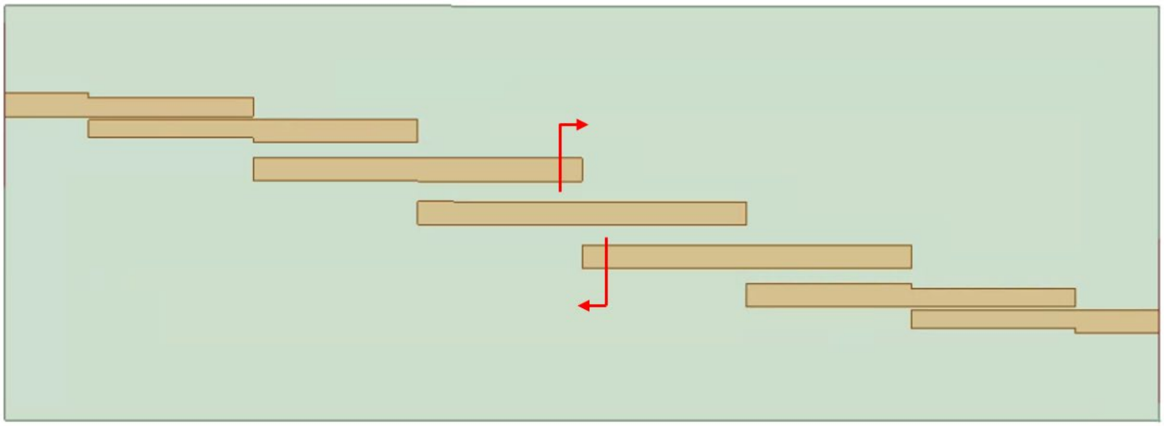

Figure 5.7: HFSS model of 5th order coupled line filter. Locations for the shortening of resonators 2 and 4 are shown in red.

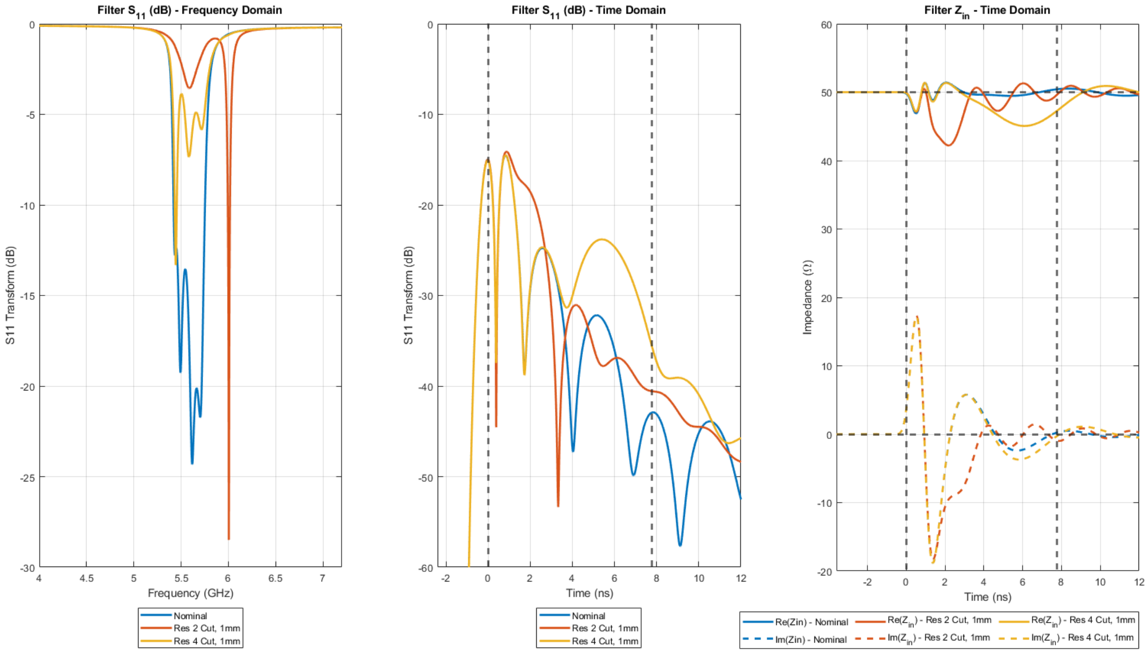

Figure 5.8: Simulated coupled line filter return loss in both the frequency domain and time domain. Input impedance in the time domain is additionally included. The cases included are the nominal case and resonators 2 and 4 cut by 1 mm independently.

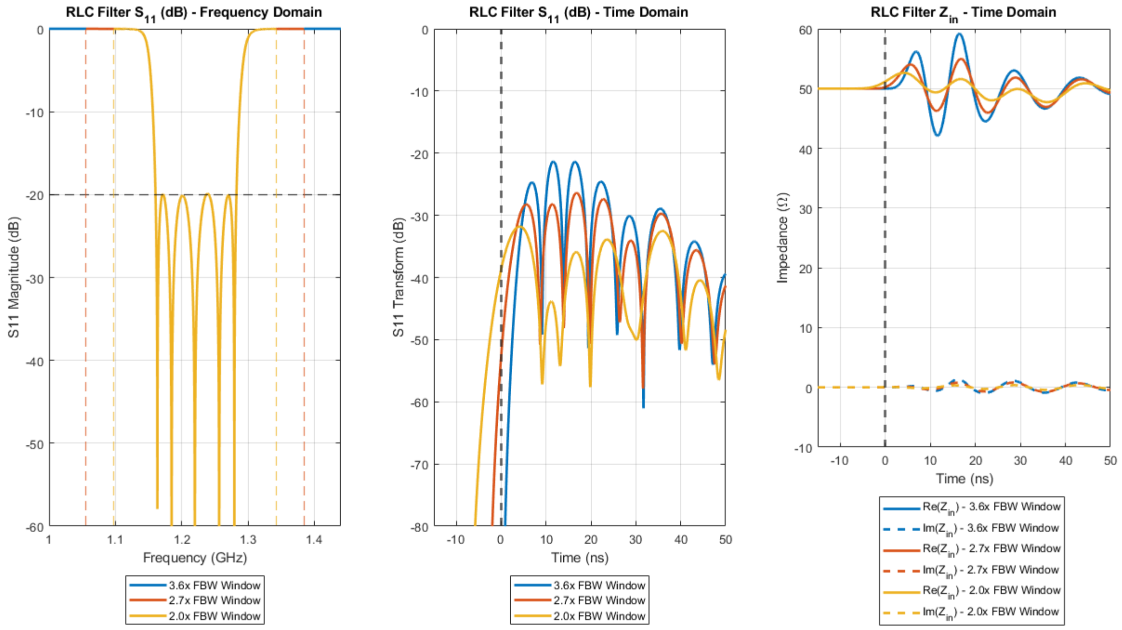

Figure 5.9: Secondary example of an idealized 5th order Chebyshev ripple LC bandpass filter with 10% fractional bandwidth centered around 1.22 GHz. The frequency window was iteratively diminished relative to the passband to demonstrate the impact the frequency window has on the analysis method. Largely, peaks have reduced magnitude, and nulls are in the same location.

A prime example of the difficulty in frequency domain tuning is demonstrated by changing the resonant frequency of any given resonator by altering the length. For this example, resonators 2 and 4 were shortened independently by 1 mm, increasing their resonant frequency. From the filter's performance, its tuner can see that one resonator is severely mistuned; however, it is not immediately apparent which is at fault. Transforming the return loss versus frequency into the time domain reveals a series of peaks and zeros across time. Each peak corresponds to the coupling strength between any two resonators in sequence, while each reflection zero corresponds to a given resonator. The closer aligned the return loss is to the nominal case, the better tuned the filter. Looking at the time domain return loss reveals what was masked by the frequency domain return loss: When the 2nd resonator causally is mistuned, the response aligns with the nominal until the coupling peak between the first and second resonator where they begin to diverge significantly, leading to a complete misalignment by the reflection zero of the second resonator. A similar situation is seen for the second resonator. If the circuit's group delay is known, one can even locate exactly where a filter is mistuned by halving (Measured time is doubled from real due to reflection) the measured time of misalignment.

5.3 Circulator Fabrication Error Simulation

As a circulator can be modeled as a single resonator filter, time domain impedance analysis was applied to the measured results of the initial fabricated prototype. Unfortunately, the non-passband return loss of a circulator is not as well behaved as a filter of comparable bandwidth and passband return loss. This results in scattering parameters varying wildly and virtually unpredictably at frequencies outside of the passband, forcing a comparatively small frequency window with which to analyze, 1 GHz to 5 GHz, where the circulator passband is 2 GHz to 4 GHz. While the resolution of the time domain impedance analysis is hindered somewhat, it is still more than enough to discern problematic areas with regards to a ferrimagnetic circulator.

As previously mentioned, the fabricated circulator was found to have significant errors in the measured scattering parameters. After some troubleshooting in simulations and refabrication, it was found the two most likely sources of poor performance were in the air gaps between the enclosure's ground and the substrate, along with a poor electrical connection between the enclosure ground and the testing circuit board ground. It can be inferred that an increase in the air gaps results in an overall lower dielectric constant in the enclosure, altering the impedances of the lines allowing an impedance mismatch. Poor soldering between the differing ground reduces the cross-sectional area of the current return path, reducing the inductance of the path.

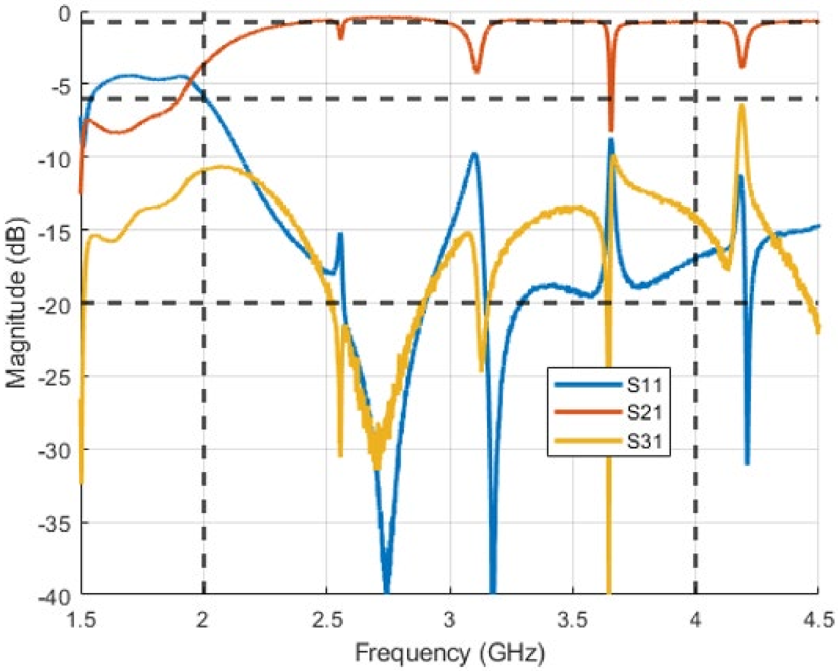

Figure 5.10: Measured scattering parameters of the prototype circulator with fabrication errors.

In previous simulations of this circulator, air gaps were included between the dielectric and ferrite blocks and were found to have minimal effect on circulator performance for their expected range due to fabrication. After fabrication, it was found that these air gaps did not comprise the entirety of air gaps in the system, as the gaps between the grounding enclosure and the blocks were neglected. Thus, equidistant gaps between all pieces of the enclosure were included. The increase in space between the signal trace and the dielectric blocks was between only the upper pieces, as gravity forces contact between the lower pieces.

Figure 5.11 depicts the performance of the simulation model depicted in Figure 3.31 when the solder is alternately kept and removed from the structure for a variety of airgap distances. It can be seen that for each air gap case, the scattering parameter performance is largely the same. The most significant difference is the addition of resonances in the upper frequencies of the passband. These resonant frequencies move up in frequency as the air gaps increase, as the electrical size of the enclosure reduces with the effective permittivity.

Figure 5.12 depicts the same performance as in Figure 5.11 but reformatted to highlight the impact of the air gap thickness of performance, with and without a well soldered electrical connection between the enclosure ground and the testing circuit board ground. In both cases, the performance of the circulator is significantly lessened.

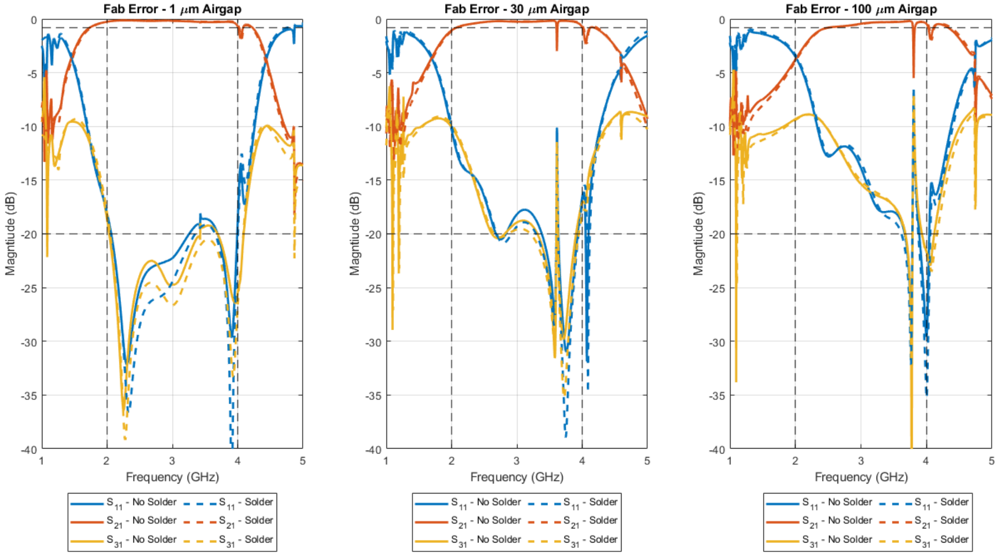

Figure 5.11: Simulated performance of fabrication errors. Depicted are the differences in performance dependent on the presence of an electrical connection between the circulator ground and testing circuit board ground for an increased air gap thickness of 1 µm (left), 30 µm (middle), and 100 µm (right).

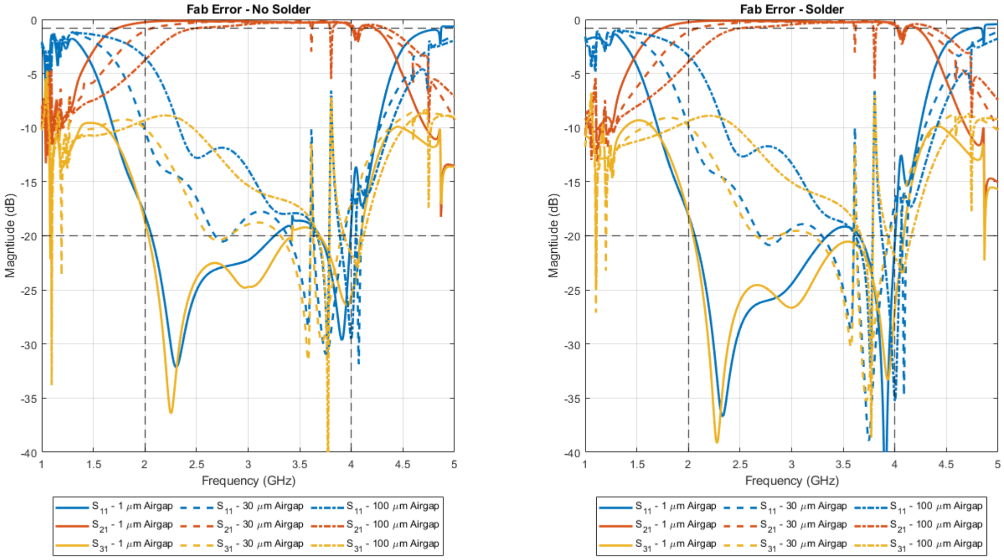

Figure 5.12: Simulated performance of fabrication errors. Depicted are the differences in performance depending on the level of increased air gap thickness for a poor soldered case (left) and a well-soldered case (right).

5.4 Time Domain Analysis on Circulator Impedance

Time domain impedance analysis was applied to the simulated and measured performance of the circulator, both before and after correcting the aforementioned fabrication errors. The poor solder connection was corrected simply by improved soldering techniques, using a larger quantity of solder as well as solder flux. The air gap thickness correction was ultimately much more involved. As there is not a consistent physical contact between the dielectric blocks and the circulator enclosure, the impedance of the quarter-wave transformers and the ferrite junction is significantly altered. A compressible conductor between the two materials was desired to maintain physical contact. After some research, 2 mils thick Indium foil from Custom Thermoelectric was obtained and integrated into the fabrication process, as detailed in Chapter 4.

The fabrication error simulation scattering parameters were analyzed using time domain impedance analysis. Figure 5.13 depicts the best and worst-case scenarios. As a circulator can be represented as a first-order directional bandpass filter, one would expect a reflection null at exactly half the group delay. The best-case scenario, with 1 micron air gaps and a well-soldered ground connection, is found to have a time domain return loss with a single reflection null at exactly this time. The worst-case scenario, with 100 micron air gaps and a poorly soldered connection, has no reflection null in the relevant time span and is found to be extremely capacitive compared to the best case scenario at times corresponding to the metal enclosure.

This analysis method was repeated for all cases. Figure 5.14 depicts the simulated performance for each air gap thickness for a well-soldered ground connection, while Figure 5.15 depicts the simulated performance for each air gap thickness for a poorly soldered connection. As air thickness increases, the time domain return loss significantly decreases, and the enclosure becomes far more capacitive.

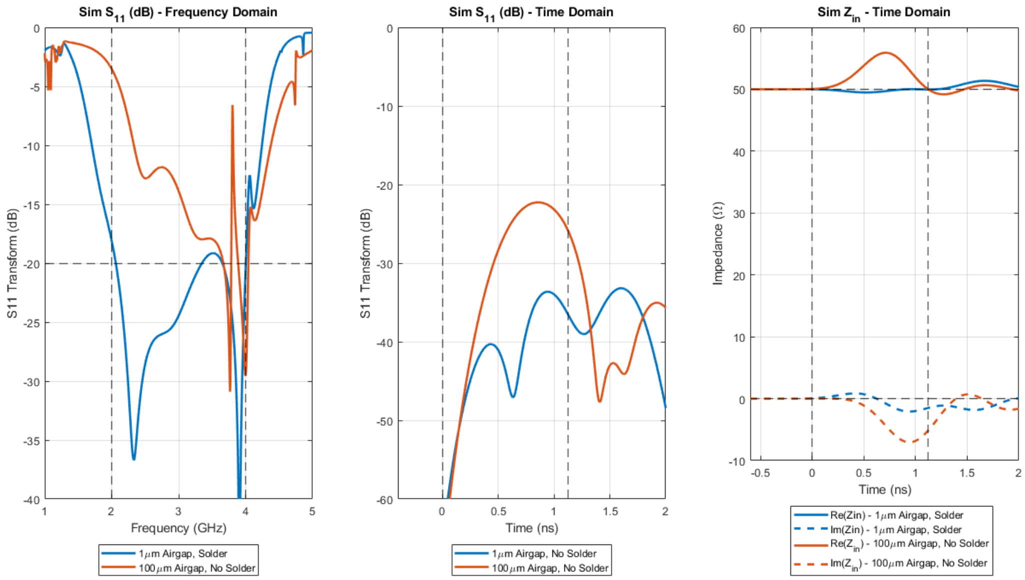

Figure 5.13: Simulated circulator performance comparison between the nominal case (1 µm air gap with well-soldered connection) and the worst case considered (100 µm air gap with poorly soldered connection). Vertical dashed lines are included to show the times at which the signal is introduced and the group delay of the best case circulator.

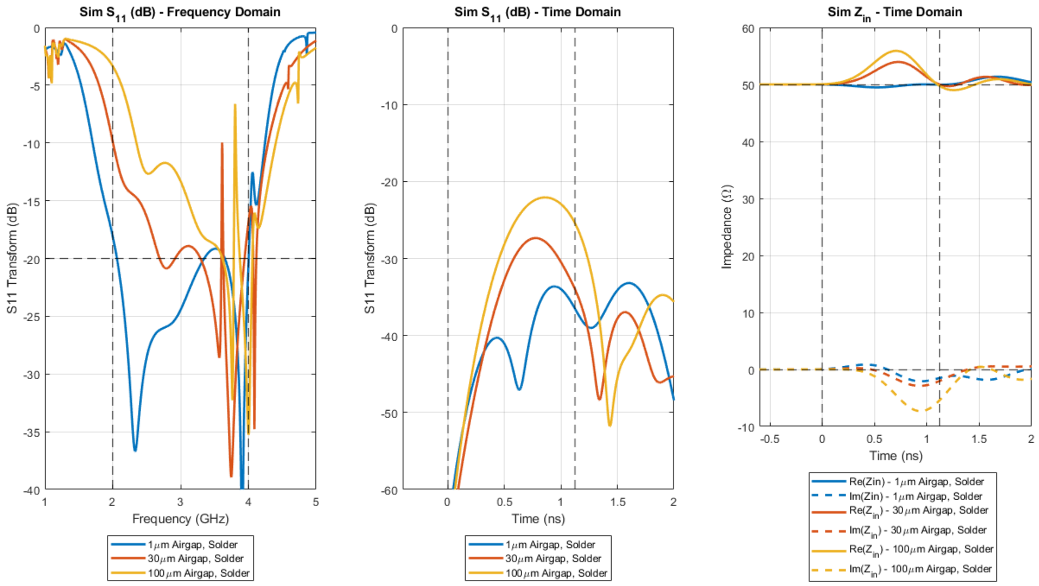

Figure 5.14: Simulated circulator performance comparison for a variety of airgap thicknesses (1 µm, 30 µm, and 100 µm) with a well-soldered ground connection. Depicted are the return loss in the frequency domain (left) and the time domain (middle), and the input impedance at port 1 in the time domain (right).

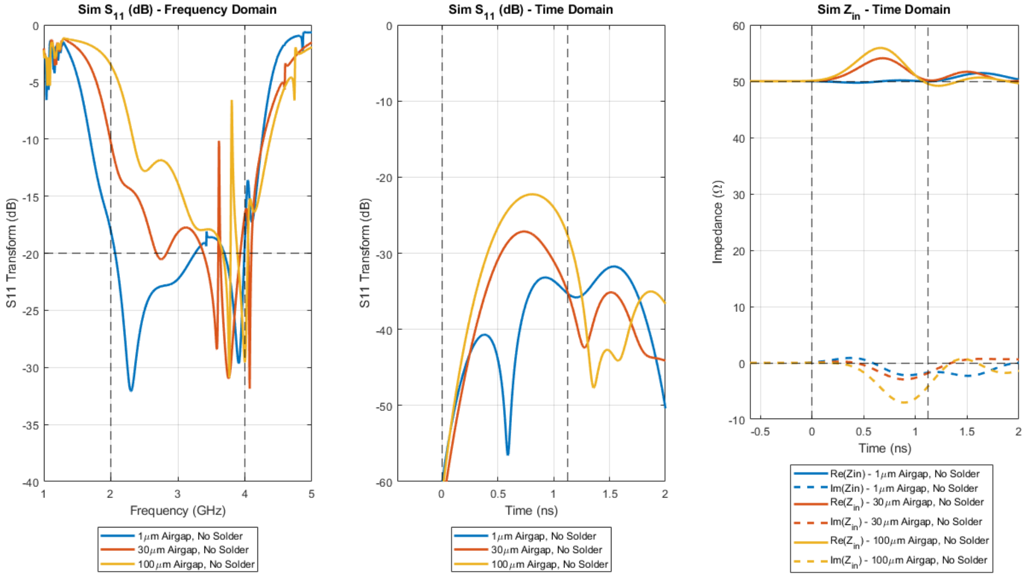

Figure 5.15: Simulated circulator performance comparison for a variety of airgap thicknesses (1 µm, 30 µm, and 100 µm) with a poorly soldered ground connection. Depicted are the return loss in the frequency domain (left) and the time domain (middle), and the input impedance at port 1 in the time domain (right).

Time domain impedance analysis was performed on the measured circulator scattering parameters, with fabrication errors removed. Figure 5.16 depicts the frequency domain and time domain return loss, along with the time domain input impedance of the measured and simulated performance of the circulator. As with the simulations with intentionally introduced fabrication error, the ferrite junction resonator is only weakly felt at the center frequency, with the structure overly capacitive and ill-matched in impedance. While the return loss of the circulator at room temperature is lower at most frequencies compared to 100 °C, the input impedance at high temperatures more closely matches that of the ideal simulation results.

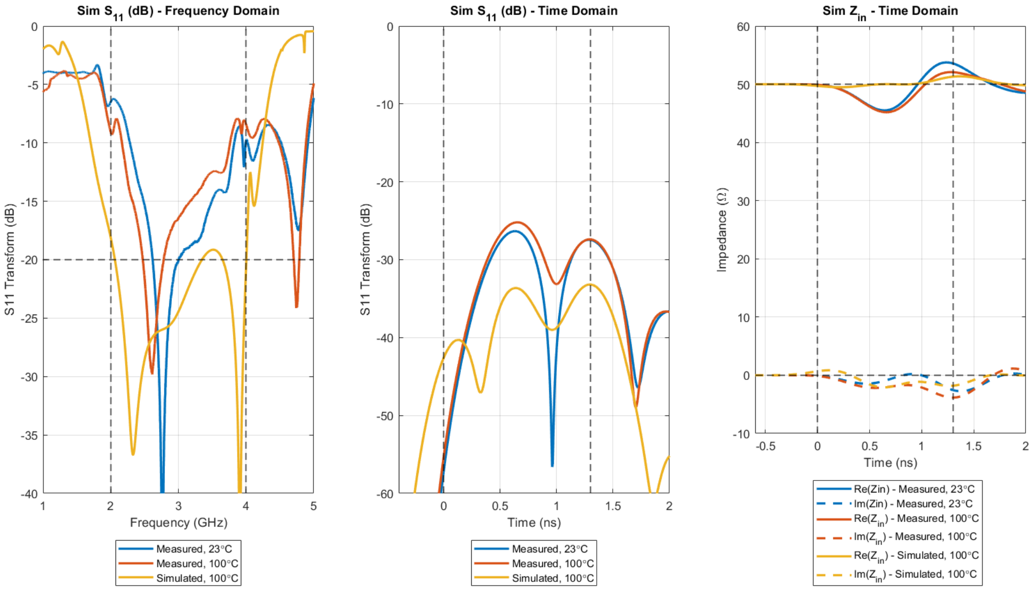

Figure 5.16: Frequency and time domain performance and time domain input impedance of the circulator. Depicted are the measured performance for room temperature (23 °C) and 100 °C, along with the ideal simulated performance at 100 °C.

5.5 Conclusion

The original fabricated circulator was found to have extremely poor performance, with low return loss with resonances and spurs across the passband. A time domain impedance analysis method is described and characterized using a coupled line bandpass filter as an example. The method was then expanded to the fabricated and simulated three port circulators for the first time in order to find and correct the fabrication errors responsible. After analysis, the major faults were found to be unintentional air gaps in the circulator enclosure, and a poor electrical connection between the device and system ground planes. The correction of these errors resulted in the significantly improved performance of the circulator shown in Chapter 4.

Chapter 6

Conclusions & Future Work

6.1 Conclusions

Ferrimagnetic materials, when used appropriately, are capable of unique feats for RF and microwave devices. Passive power circulation for monostatic simultaneous transmit and receive radar systems, passive power limitation through attenuation for sensitive radar systems, and passive power isolation for monostatic transceiver systems. While degrees of success can be achieved without ferrimagnetic materials, they are required in order to achieve a low cost and small size implementation, with real-time passive results.

Ferrimagnetic circulators emerged as a practical method to passively introduce non-reciprocity in RF and microwave systems quickly found themselves the primary solution to said problem. In the decades hence, a great deal of research has gone into making circulators more practical in terms of integration into existing systems and in terms of performance. From their beginning, ferrimagnetic circulators have been bulky and exceedingly unwieldy in terms of integration, often resulting in a radar systems engineer needing to incorporate a coaxial or drop-in integration method if a circulator is used. Even when ignoring the methods of port integration, ferrimagnetic circulators tend to be bulky. Commercial off-the-shelf (COTS) circulators are frequently seen to have a large footprint, with a device thickness high enough to be nearly cubic in shape. After several decades, the properties of ferrite junction circulators were successfully characterized, allowing significant improvement in port isolation, bandwidth, and impedance matching. Currently, ferrimagnetic circulators operating in the below resonance operating region are capable of exceeding octave bandwidths, with over 20 dB of return loss and isolation.

In this thesis, the basics of ferrimagnetics as it pertains to RF and microwave ferrimagnetic devices such as circulators were discussed and explained to the benefit of an experienced RF and microwave engineer new to anisotropic ferrimagnetic materials. A design for an octave bandwidth high temperature and high power operating at S-band (2-4 GHz) was simulated and demonstrated. A circulator fabrication method using a Tetris-like stacking of dielectric and ferrite blocks was analyzed. The aforementioned design was fabricated and measured at all combinations of room temperature, high temperature (100 °C), low power (-10 dBm), and high power (47 dBm). Potential fabrication difficulties using the fabrication methods used to minimize the circulator's size were discussed and analyzed, with practical solutions given using a time domain impedance analysis method.

6.2 Scientific Impact

While RF and microwave devices have utilized the 3D Tetris-like building block method fabrication method, to this author's knowledge, this is the first time it has been applied to ferrimagnetic circulators. In conjunction with a surface mount integration, the construction and design of this circulator are shown to be novel.

Additionally, time domain impedance analysis is demonstrated in a ferrimagnetic context for the first time, allowing a degree of certainty in analyzing and correcting any potential fabrication error using the aforementioned construction method.

6.3 Future Work

Despite the strides made in this circulator with regards to the below resonance ferrimagnetic circulator design and fabrication, there are still areas that can be improved upon by engineers in the future.

The pseudo-wirebond implementation of the surface mount integration circulator is far from ideal and will cease to work at frequencies higher than S-band. In the future, a higher performance solution might be the inclusion of half-castellated vias at the edges, preventing performance degradation by slight misplacement of the pseudo-wirebond trace.

The fabrication process and the surface mount integration method have been shown to work well in a below resonance circulator, but no work has been done on an above resonance circulator equivalent. As the power handling of this circulator is fairly low, power levels sufficient only to find the P_{1dB} point at which spin-waves become excited were introduced. As above, resonance circulators do not need to worry about spin-waves, much higher levels of power could be introduced to test performance.

The measured performance of the circulator has been shown to have bandwidth only half that of simulation, with only 15 dB of isolation. Several possible origins of measurement error and fabrication error were investigated and mostly corrected. Future authors could continue investigations on the remaining errors preventing the fabricated circulator from matching the ideal simulated performance.

The impedance matching network used in the circulator discussed in this thesis is standard fare for broadband circulators. Quarter-wave transformers are far from the only way to achieve a broadband match in a ferrimagnetic circulator, but they are the simplest. Future authors could potentially achieve an integrated circulator with similar performance that was electrically small enough to not excite cavity resonant modes in the passband without the use of mode suppressing vias.

References

[1] J. Wang et al., "Self Biased Y-Junction Circulator at Ku Band," *IEEE Microwave and Wireless Components Letters*, vol. 21, no. 6, pp. 292–294, Jun. 2011, DOI: 10.1109/LMWC.2011.2142297.

[2] K. K. Darrow, "Contemporary advances in physics — XIII. Ferromagnetism," *The Bell System Technical Journal*, vol. 6, no. 2, pp. 295–366, Apr. 1927, DOI: 10.1002/j.1538-7305.1927.tb01216.x.

[3] D. Polder, "VIII. On the theory of ferromagnetic resonance," *The London, Edinburgh, and Dublin Philosophical Magazine and Journal of Science*, vol. 40, no. 300, pp. 99–115, Jan. 1949, DOI: 10.1080/14786444908561215.

[4] J. Lim, G. Kim, and S. Hwang, "Suppression of Microwave Resonances in Wirebond Transitions Between Conductor-Backed Coplanar Waveguides," *IEEE Microwave and Wireless Components Letters*, vol. 18, no. 1, pp. 31–33, Jan. 2008, DOI: 10.1109/LMWC.2007.911985.

[5] W. H. Haydl, "Resonance phenomena and power loss in conductor-backed coplanar structures," *IEEE Microwave and Guided Wave Letters*, vol. 10, no. 12, pp. 514–516, Dec. 2000, DOI: 10.1109/75.895086.

[6] C. L. Hogan, "The ferromagnetic Faraday effect at microwave frequencies and its applications: The microwave gyrator," *The Bell System Technical Journal*, vol. 31, no. 1, pp. 1–31, Jan. 1952, DOI: 10.1002/j.1538-7305.1952.tb01374.x.

[7] H. Bosma, "On Stripline Y-Circulation at UHF," *IEEE Transactions on Microwave Theory and Techniques*, vol. 12, no. 1, pp. 61–72, Jan. 1964, DOI: 10.1109/TMTT.1964.1125753.

[8] H. N. Chait and T. R. Curry, "Y Circulator," *Journal of Applied Physics*, vol. 30, no. 4, pp. S152–S153, Apr. 1959, DOI: 10.1063/1.2185863.

[9] E. N. Skomal, "Theory of Operation of a 3-Port Y-Junction Ferrite Circulator," *IEEE Transactions on Microwave Theory and Techniques*, vol. 11, no. 2, pp. 117–122, Mar. 1963, DOI: 10.1109/TMTT.1963.1125612.

[10] J. B. Davies and P. Cohen, “Theoretical Design of Symmetrical Junction Stripline Circulators,” *IEEE Transactions on Microwave Theory and Techniques*, vol. 11, no. 6, pp. 506–512, Nov. 1963, DOI: 10.1109/TMTT.1963.1125717.

[11] J. Helszajn, “Quarter-Wave Coupled Junction Circulators Using Weakly Magnetized Disk Resonators,” *IEEE Transactions on Microwave Theory and Techniques*, vol. 30, no. 5, pp. 800–806, May 1982, DOI: 10.1109/TMTT.1982.1131140.

[12] D. Herstein, “A Novel Technique for Evaluation and Integration of Connectorless (Drop-In) Microwave Components,” *IEEE MTT-S International Microwave Symposium Digest*, May 1987, vol. 2, pp. 613–616. DOI: 10.1109/MWSYM.1987.1132485.

[13] X. Wang, K.-L. Wu, and W.-Y. Yin, “A Novel Surface-Mounted Monoblock Dielectric Filter,” *IEEE Transactions on Components, Packaging and Manufacturing Technology*, vol. 4, no. 11, pp. 1822–1827, Nov. 2014, doi: 10.1109/TCPMT.2014.2347342.

[14] D. K. Cheng, *Field and Wave Electromagnetics*, Pearson, 2013.

[15] D. M. Pozar, *Microwave Engineering*, Wiley, 2011.

[16] ASTM A883 / A883M-01, *Standard Test Method for Ferrimagnetic Resonance Linewidth and Gyromagnetic Ratio of Nonmetallic Magnetic Materials* (Withdrawn 2006), ASTM International, West Conshohocken, PA, 2001.

[17] N. Mo, J. J. Green, B. A. Beitscher, and C. E. Patton, “High precision metrology based microwave effective linewidth measurement technique,” *Review of Scientific Instruments*, vol. 78, no. 11, p. 113903, Nov. 2007, DOI: 10.1063/1.2813344.

[18] C. Kittel, “On the Theory of Ferromagnetic Resonance Absorption,” *Phys. Rev.*, vol. 73, no. 2, pp. 155–161, Jan. 1948, DOI: 10.1103/PhysRev.73.155.

[19] J. A. Osborn, “Demagnetizing Factors of the General Ellipsoid,” *Phys. Rev.*, vol. 67, no. 11–12, pp. 351–357, Jun. 1945, DOI: 10.1103/PhysRev.67.351.

[20] R. M. Bozorth and D. M. Chapin, “Demagnetizing Factors of Rods,” *Journal of Applied Physics*, vol. 13, no. 5, p. 320, Apr. 2004, DOI: 10.1063/1.1714873.

[21] A. Aharoni, “Demagnetizing factors for rectangular ferromagnetic prisms,” *Journal of Applied Physics*, vol. 83, no. 6, p. 3432, Jun. 1998, DOI: 10.1063/1.367113.

[22] ASTM A894 / A894M-00(2011)e1, *Standard Test Method for Saturation Magnetization or Induction of Nonmetallic Magnetic Materials* (Withdrawn 2017), ASTM International, West Conshohocken, PA, 2011.

[23] D.K. Linkhart, *Microwave Circulator Design*, Artech House, 2014.

[24] Pacific Ceramics, *Garnet Ferrites*, PCeramics.com, https://www.pceramics.com/garnetferrites.html (accessed 7 June 2021)

[25] H. Bosma, "A general model for junction circulators; choice of magnetization and bias field," *IEEE Transactions on Magnetics*, vol. 4, no. 3, pp. 587–596, Sep. 1968, DOI: 10.1109/TMAG.1968.1066335.

[26] G. L. Matthaei, L. Young, and E. M. T. Jones, *Microwave Filters, Impedance-matching Networks, and Coupling Structures*, Artech House, 1980.

[27] M. Dydyk, "Take two steps toward better circulator design," *Microwaves*, vol. 18, pp. 53–56, Mar. 1979.

[28] J. Helszajn, "Synthesis of Quarter-Wave Coupled Circulators with Chebyshev Characteristics (Short Papers)," *IEEE Transactions on Microwave Theory and Techniques*, vol. 20, no. 11, pp. 764–769, Nov. 1972, DOI: 10.1109/TMTT.1972.1127870.

[29] C. E. Fay and R. L. Comstock, "Operation of the Ferrite Junction Circulator," *IEEE Transactions on Microwave Theory and Techniques*, vol. 13, no. 1, pp. 15–27, Jan. 1965, DOI: 10.1109/TMTT.1965.1125923.

[30] J. Helszajn, *The Stripline Circulator: Theory and Practice*, John Wiley & Sons, Inc., 2008.

[31] H. A. Wheeler, "A Simple Formula for the Capacitance of a disk on Dielectric on a Plane," *IEEE Transactions on Microwave Theory and Techniques*, vol. 30, no. 11, pp. 2050–2054, Nov. 1982, DOI: 10.1109/TMTT.1982.1131376.

[32] J. Helszajn, "Operation of Tracking Circulators," *IEEE Transactions on Microwave Theory and Techniques*, vol. 29, no. 7, pp. 700–707, Jul. 1981, DOI: 10.1109/TMTT.1981.1130431.

[33] A. W. Scott, *Cooling of Electronic Equipment*, Wiley, 1974.

[34] B. Lax and K. J. Button, *Microwave Ferrites and Ferrimagnetics*, McGraw-Hill, 1962

[35] B. D. Hannaford and M. J. Howes, "A General Theory for Spin-Wave Suppression in Ferrites," *G-MTT International Microwave Symposium Digest*, May 1967, pp. 95–99. DOI: 10.1109/GMTT.1967.1122608.

[36] Engineering ToolBox, (2008). *Ceramic Materials Properties*. Available at: https://www.engineeringtoolbox.com/ceramics-properties-d_1227.html.

[37] J. Bahl and R. Garg, “Simple and accurate formulas for a microstrip with finite strip thickness,” *Proceedings of the IEEE*, vol. 65, no. 11, pp. 1611–1612, Nov. 1977, DOI: 10.1109/PROC.1977.10783.

[38] R. K. Tenzer, "Estimating Leakage Factors for Magnetic Circuits by a Simple Method", *Applied Magnetics; Valparaiso, IN: The Indiana Steel Products Co*., April-June 1957.

[39] K&J Magnetics, Inc., *Demagnetization (BH) Curves for Neodymium Magnets*, kjmagnetics.com, https://www.kjmagnetics.com/bhcurves.asp, (accessed 7 June 2021)

[40] Magnet Kingdom, *Item #CM-0279 Ceramic Disk*, MagnetKingdom.com, https:www.magnetkingdom.com/product-detail.asp?partID=76 (accessed 7 June 2021)

[41] B. Freemire et al., “Low Powered RF Measurements of Dielectric Materials For Use In High Pressure Gas Filled RF Cavities” p. 3.

[42] Pacific Ceramics, *Dielectrics*, PCeramics.com, https://www.pceramics.com/dielectrics.html (accessed 7 June 2021)

[43] J. Dunsmore, “Tuning band pass filters in the time domain*,” IEEE MTT-S International Microwave Symposium Digest* (Cat. No.99CH36282), Jun. 1999, vol. 3, pp. 1351–1354 vol.3. DOI: 10.1109/MWSYM.1999.779638.

[44] J.-S. Hong and M. J. Lancaster, *Microstrip Filters for RF/Microwave Applications*, John Wiley & Sons, In., 2001.

[45] Kirby Microwave, Agilent *AN 1287-8 Simplified Filter Tuning Using Time Domain*, KirbyMicrowave.co.uk, https://www.kirkbymicrowave.co.uk/Support/Links/application-notes/HP-Agilent-Keysight/Keysight-5968-5328E.pdf (accessed 7 June 2021)